Aus dem Max-Planck Institut für Kolloid and Grenzflächenforschung

---

Herstellung poröser Metalloxide für katalytische Anwendungen unter Verwendung von Templatierungsverfahren

Fabrication of porous metal oxides for catalytic applications using templating techniques

Dissertation
zur Erlangung des akademischen Grades
"doctor rerum naturalium"
(Dr. rer. nat.)
in der Wissenschaftsdisziplin "Kolloidchemie"

eingereicht an der
Mathematisch-Naturwissenschaftlichen Fakultät
der Universität Potsdam

von
Atul Suresh Deshpande
Aus Daund, Indien

Potsdam, den 19. April 2004

Contents

ÈÈÏ;jgqri fhAÈÈ

1Introduction

"There is plenty of room at the bottom" were the famous words from physicist, Nobel laureate and a great visionary, Richard P. Feynman [1]. In this legendary talk delivered in 1959, he opened the gateways of a vast unexplored territory of "nanoscience". He discussed the possibility of maneuvering atoms, building computer circuits that are in the scale of nanometers, properties of materials and the problems that might arise in dealing with the machines at very small length scales. Now, after four decades, we see that the word "nano" is no more restricted to the scientific community but is also playing a role in the social and political arena. Indeed we come across many things in our daily life, which are based on nanostructured materials such as electronic devices, automotive catalysts, batteries, cosmetics and medicines.

Nanostructured materials may differ considerably in terms of properties as compared to the bulk materials. Confinement of matter in zero (quantum dots), one (nanowires), two nanosheets) or three (periodic structures) dimensions on the nanometer scale can show tremendous changes in material properties like conductivity, magnetic behavior, optical properties. Conventionally, these features were tuned by the ways such as doping, choosing between synthetic approaches e.g. solid state, hydrothermal or sol-gel process, and optimizing the synthesis parameter. It was not until the last decade that serious efforts were made to tailor the properties of materials by structural manipulation. The more recent synthetic approaches are based on the organization of matter in which the

kinetic rather than the thermodynamic aspects dictate the terms, and higher order organizational states dominate over equilibrium states. For example, Mackay in his work "flexicrystallography" described structure and symmetry properties of about 50 minimal-energy surfaces [2]. He indicated that the traditional crystallographic geometry does not apply to curved structures but may be generalized to finite and infinite arrangements, where strict equivalence is replaced by quasi-equivalence. This enables one to go beyond the conventional crystallography and with its 230 space groups. In fact, nature in the form of biominerals has already exploited this idea. Many biominerals are organized over multiple length scales to yield hierarchical materials with complex forms.

Fig.1.1 shows a SEM photograph of a Radiolarian. Radiolarians are amoeba-like single celled organisms, which are protozoans. They have silicious exoskeletons, called tests. These tests are usually spherically symmetrical with lots of spines radiating outward. Radiolaria use an ordered assembly of vesicles as a structure-directing scaffold and produce a very complex structure through controlled deposition of silica. These intricate morphological features impart robustness to the exoskeleton and also give buoyancy to the organism. Deeper understanding of the processes involved in biomineralization has led materials scientists to develop a fascinating synthetic approach in materials synthesis, namely, bio-inspired materials [3]. In this approach, biological concepts, mechanisms, functions and design features are taken as starting point to get to the new synthetic materials and devices. The basic principal is not to copy the process, but to use

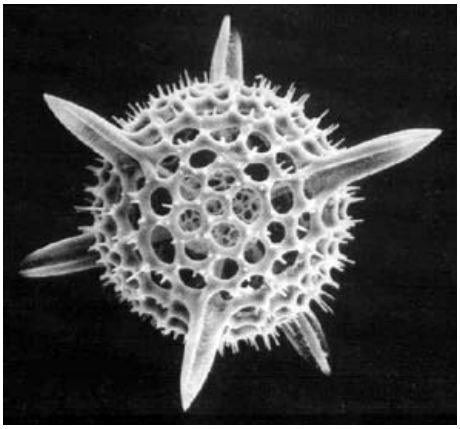

Figure 1.1 Exoskeleton of a radiolarian

the knowledge as a guideline. In this context, synthesis of structured inorganic materials hinges on the idea of using molecular objects or supramolecular assemblies as structure directing agents to control the morphology of materials at nanometer scale. In recent years this approach has gained popularity as morphological features and properties of the final material can be tuned to the requirements by choosing the appropriate structure directing agent and synthesis conditions.

The motif of the present work to use some of these principles and philosophies to generate nano-structured functional inorganic materials with enhanced performance.

The present work deals with the synthesis of porous metal oxides using porous polymeric beads and block-copolymers as structure directing agents. The first section describes the synthesis of macroporous TiO_2-M_2O_3 (M=Al, Ga, In) spheres. The procedure is based on the use of the corresponding metal alkoxides in a sol-gel process and macroporous polystyrene reverse phase chromatography beads. In this part, we discuss the effect of the structure-directing agent and added oxides on the crystallization behavior and surface properties of TiO_2 and the photocatalytic activity of the final oxide spheres. The second section describes the synthesis of a complete range of $Ce_xZr_{1-x}O_2$ nanoparticle sols and their characterization using various techniques. The third part includes the use of $Ce_xZr_{1-x}O_2$ nanoparticle sols to synthesis mesoporous $Ce_xZr_{1-x}O_2$ spheres as well as CuO loaded samples of the general composition $(Ce_xZr_{1-x}O_2)_a$ $(CuO)_b$. Mesoporous polystyrene beads for size exclusion chromatography were used as templates. The catalytic activity of these spheres for the steam reforming of methanol is also discussed.

The fourth section describes the synthesis of mesoporous $Ce_xZr_{1-x}O_2$ powders via an evaporation induced self-assembly process using $Ce_xZr_{1-x}O_2$ nanoparticle sols and block co-polymers as template.

2 Background

Porosity in materials imparts many advantageous features [4]. For example, bones of birds are highly porous but all the same strong and elastic, which is suitable for flying. Activated charcoal, which has high porosity, acts as good adsorbent and is used in the sugar industry as a decolorizing agent. Zeolites, which have specific pore structure, are used for the ion exchange processes. In general, porous materials have found uses in various areas of our life and hence it is important to develop and study advanced porous materials.

In the chemical synthesis processes, porosity can be generated by inter-particle voids formed during co-precipitation, by controlled hydrolysis of alkoxides to get xerogels or by combustion method, where the gases evolved during the process result in porous materials. In general, these methods are unrefined and no control over the porosity is possible during the synthesis.

A more sophisticated approach is to use an object as a structure-directing agent and to build the desired material around it. The object used for structure direction is termed as *Template* and the process in general is called *Templating*. The template can be a single molecule, a molecular assembly or even a larger, object.

Depending on the role of template in generating the final structure, the templating processes are classified into two main groups: Direct templating and indirect templating.

Direct templating is subdivided into *Transcriptive* and *Synergistic*. In transcriptive templating, one uses template with a definite form. If the building material fills the whole space around the template so that the final material after the template removal looks like

inverse replica of the original template, the process is called *Casting.* If only a layer of building material is formed on the template surface so that the final material looks like inverse hollow replica of the original template, then the process is called *Coating*. In synergistic templating, the structured material is formed by mutual interaction of the template and the building material leading to self-assembly and ordering.

Indirect templating, also termed as *Morphosynthesis*, results when instead of an object template a confined chemical environment is used, provided for example by a bi-continuous phase formed by microphase separation in oil-water type of systems. The transformation of the building material into the final material can occur by three different processes: *Static morphosynthesis*, resulting from replication of a preformed microphase separated state into final material; *Reconstructive morphosynthesis*, resulting from replication of a preformed microphase separated state and then transformation into other structure; and *Transitory morphosynthesis*, resulting from replication of transiently formed microphase separated state by a continuous process into final material.

Apart from this, *Integrative synthesis* is also known, which results from the combination of one or more processes described above. This classification has been described in detail by Mann *et. al.* [5].

2.1 Porous materials

2.1.1 Characteristics

Though porous materials such as clays, activated charcoal and zeolites were known for a long time, it was not until the last century that systematic studies of porous systems were made.

Porous materials are differentiated on the basis of pore structure and pore sizes. According to IUPAC [6] nomenclature, pores of size smaller than 2 nm are called *micropores*, pores between 2-50 nm are called *mesopores* and pores bigger than 50 nm are called *macropores*. Depending on the connectivity between the pores, they are termed *open* if they are connected and *closed* if they are not connected.

The porous material are also characterized by the *porosity,* which is the fraction of volume occupied by the pores compared to total volume and *specific surface area*, which is the surface area per unit mass of the sample.

2.1.2 History

One of the most widely studied classes of porous materials are zeolites. The zeolites are natural minerals known for almost 250 years. Zeolites (from the greek *zein*, to boil, and *lithos*, stone) are hydrated alkaline or alkaline earth aluminosilicates with the general formula $M^{n+}_{x/n}[(AlO_2)_x(SiO_2)_y]^{x-} \cdot wH_2O$. They have a cage like open pore structure formed from interconnected SiO_4 and AlO_4 tetrahedra. The pore sizes are characteristic of a particular type of zeolite and are in the range of 0.4-1.5 nm. In 1862, Sainte Claire Deville reported the first synthetic zeolite [7]. Till this date, around 100 synthetic zeolites are known. The general synthetic procedure involves the use of short chain alkyl amines as templates and the templating process is considered to be synergistic. The alkyl chains of these amines are hydrophobic in nature and their dissolution in water occurs via formation of water pockets. The key point in the synthesis is the weak interaction between SiO_4 and AlO_4 with the template, which gives stable structures even after the template removal. Due to the uniform porosity, zeolites are used for selective ion

removal, fluid catalytic cracking of heavy petroleum distillates, in detergents and for many other applications.

However, zeolites, are not useful to carry out reactions with molecules of larger size, because the pore size is restricted to below 2 nm. Hence, efforts to get the materials having uniform pores with size greater than 2 nm was on. The first success was achieved by Kresge *et. al.* [8]. They reported the synthesis of a new family of porous silicon dioxide materials called M41S. The templates used in this case were long chain alkyl ammonium halides. The synthesis mechanism follows synergistic templating, but instead of single molecules interacting with SiO_4 tetrahedra, the alkyl ammonium ions assemble in the form of micelles, which interact further with the inorganics to give ordered porous structure.

Depending upon the ratio of template to silica content three main materials were described in the M41S family. MCM-41 has cylindrical pores, ordered in a hexagonal fashion, MCM-48 has a cubic, bi-continuous pore structure, and MCM-50 is lamellar. The discovery of these materials opened a whole new area of mesoporous oxides. The original work of Kresge *et.al.* [8] is now amongst the most cited articles with 3461 citation till date.

In spite of tremendous efforts, the synthesis of only a few mesoporous, M41S-like transition metal oxides has been reported. The first attempts were reported by Huo *et al.* [9] They reported a generalized route for the formation of surfactant-inorganic composites. However, the structures were not stable on surfactant removal. Antonelli and Ying reported the first non-silica mesoporous material [10]. They synthesized mesoporous TiO_2 by using the charged surfactant tetradecyl phosphate and controlling the hydrolysis of Ti-isopropoxide by addition of acetylacetone. These reports were followed by the synthesis

of mesoporous Nb_2O_5 and Ta_2O_5, using neutral alkyl amine surfactants [11, 12]. Mesoporous zirconia has been obtained with anionic surfactants [13, 14]. Three kinds of surfactants, $CH_3(CH_2)_{10}OSO_3Na$, $CH_3(CH_2)_{14}OSO_2Na$, and $(C_{12}H_{25}O)PO(OH)_2$, were used. A hexagonal mesostructured vanadium oxide can be synthesized by acid-catalyzed hydrolysis of ethanolic cetyltrimethylammonium vanadate (CTAV) [15].

While the matter of formation mechanism of MCM-41 and related materials remained controversial, Attard *et.al*. [16] came up with a new approach of transcriptive (casting) templating, in which preformed liquid crystalline phases of block-co-polymer were used for the templating and the formation of mesoporous silica. They demonstrated that silica materials with various pore-structures could be obtained by choosing the initial liquid crystalline phase. In 1998, Yang *et.al*., reported a generalized method for the synthesis of inorganic materials using block-co-polymers and anhydrous metal chlorides [17]. Numerous accounts of silica and non-silica materials were reported afterwards and excellent reviews are available to follow this development [18-21]

In general, the M41S type synthesis is based on the synergistic approach and depends upon complex interactions between the surfactant and the inorganic matter. It is not easy to get the desired product with controlled porosity. The transcriptive approach followed by Attard *et. al.* [16] is more useful in this regard. The use of the block-polymers, though useful in getting mesoporous materials, is unsuitable to get larger pores that are desirable for many applications. Macroporous materials (i.e., pore size > 50 nm) are particularly interesting, due to their improved transport properties. Organized macroporous arrays present optimal fluxes, and diffusion is not a limiting issue for these materials. This is a central point for any processes concerning accessibility, such as catalysis, sorption, delivery, or sensors.

In this regard, the first case of ordered macroporous silica was reported by Velev *et. al*. [22]. They used monosized spherical latex particles, which on close packing give an ordered assembly of particles called *colloidal crystal* as the assembly resembles close packing of atoms in the normal crystals. The voids between the spheres were filled with a silica precursor, which was transformed into amorphous silica and the template was subsequently removed. The process was simplified by Holland *et. al.* who used metal alkoxides as precursors [23]. This approach has been very popular and various materials from oxides to metals have been synthesized in this manner. Concurrent with the work of Velev *et. al*., Imhof and Pine reported [24] the use of crystal like assemblies of densely packed, monodisperse non-aqueous emulsion droplets as template to synthesize ordered macroporous TiO_2, ZrO_2 and SiO_2. Caruso *et. al*. demonstrated the use of polymer gels and cellulose based membranes as templates, which have a macroporous bi-continuous structure [25, 26]. A major contribution to the templating approach was given by the same author in developing different ways of the utilization of precursors such as *nanocoating* and *nanocasting* [27, 28]. In the nanocoating process, a thin layer of precursor is formed on the template surface. The advantage of this approach is that by controlling the thickness of the precursor layer, one can control to some extent the crystal growth and the connectivity between the particles. Furthermore, the combined use of macroporous polymer gels and block-co-polymers to get silica materials with hierarchical pore structure was also demonstrated [29]. The advantage of these kinds of systems is that they show better flow property due to the macroporous network while occurrence of the mesopores results in greater surface area.

One more widely used template has been the porous alumina membrane. These membranes possess cylindrical pores. By using these membranes Lakshmi *et. al.* first

reported the synthesis of TiO_2, ZrO_2 and WO_3 nanotubes and nanofibres, depending upon the immersion time of the membrane in precursor solution [30].

Apart from this, organogels [31, 32], bacterial fibres [33], electrospun fibers [34], starch gel [35], eggshell membrane [36], bioskeletons [37], viruses [38] and lot of other systems as templates are reported in the literature.

From the literature survey one can see that the self-assembly processes are more specific and depend strongly on the specific template-precursor interactions and reaction conditions such as pH, temperature, chemical environment. Hence these processes cannot be applied as general synthetic process.

On the other hand, the transcriptive process in which preformed templates or templates with well-defined forms are used, is more effective and easy to generalize. Solid templates such as polymer gels or membranes are stable and can be used in a wide range of experimental conditions.

In general, an ideal template can be considered as the one that is readily available or easy to process. It should be stable throughout the templating process and can easily be removed to obtain the final product. The templating process should be simple, effective and reproducible. The synthetic approach should be easy to generalize such that a large variety of materials can be obtained.

2.2 Precusors

Precursor is a general term that can be roughly defined as a material, which can be used directly or transformed during the synthesis process to obtain the desired product. In the processing of ceramic materials, contrary to the solid-state synthesis, which give non-

structured material, the soft chemical processes designed for obtaining nanostructured materials, rarely involve the use of bulk oxide. An exception is the synthesis of V_2O_5 nanotubes reported by Niederberger *et. al.* [39], which involves the use of V_2O_5 bulk oxide as the precursor. A more popular approach is the use of sol-gel processes based on alkoxides. In these processes, the metal alkoxides react readily with water and undergo hydrolysis to form small cluster of partially or fully hydrolyzed metal oxide precursor in solution. These clusters then undergo condensation reaction to form a network or a gel. A schematic reaction for metal alkoxides with tetravalent metals is shown in Fig. 2.1

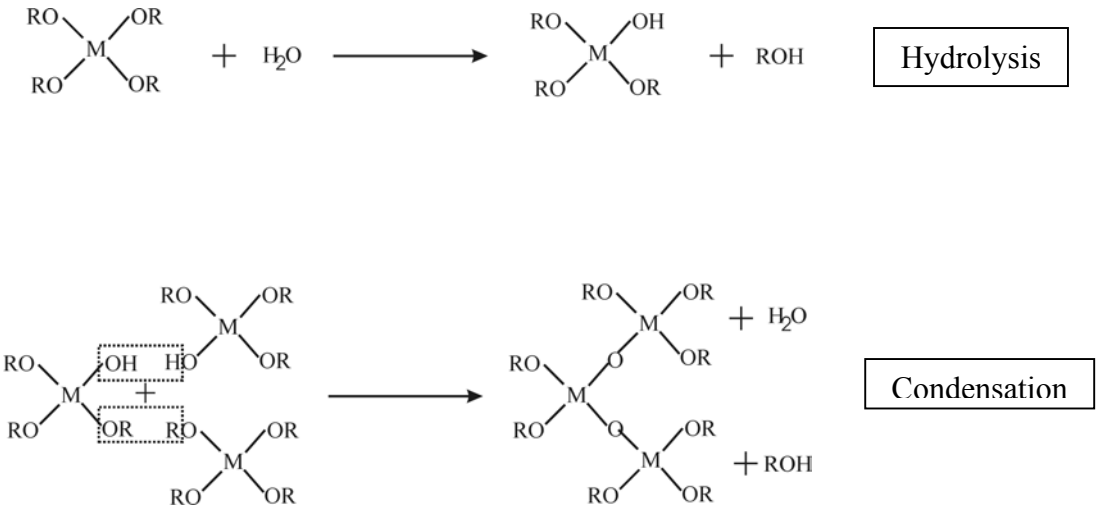

Figure 2.1 Reactions involved in the sol-gel process.

Change in the reaction conditions, such as temperature, pH, ratio of water to alkoxide, can be used to control the hydrolysis and condensation of metal alkoxides, which is essential for formation of better gels. Addition of reagents such as acetylacetone can also be used in controlling the hydrolysis and condensation process. Apart from alkoxides, anhydrous metal chlorides react vigorously with alcohols resulting in splitting of the

alcohol similar to the hydrolysis process giving extended networks or gels. Yang *et. al.* have used this process to produce a large variety of mesoporous metal oxides [17].

Besides alkoxides as precursor, pre-formed nanoparticles also offer an attractive option [40]. Nanoparticles possess highly active surface, which can bind to the other particles forming a network. Increasing the concentration or changing the pH, for example, can effect the gelation of nanoparticle sols. Many reports demonstrate the successful use of nanoparticles to obtain nanoporous materials.[33, 37, 41-44]. The advantage of using nanoparticles is that the nanoparticles are much denser than the clusters formed during the hydrolysis reaction of alkoxides. Consequently, template removal by heat treatment results in less shrinkage of the structure in case of nanoparticulate system as compared to the gels obtained from alkoxide sol-gel process. If the nanoparticles are crystalline, high calcination temperatures are not required. Alternatively, the template can be removed by chemical processes. In the transformation of amorphous gels from alkoxide process, the process of crystallization may result in the collapse of the structure. This can be avoided by the use of crystalline nanoparticles.

In the present work, we demonstrate the use of sol-gel processes based on metal alkoxide chemistry as precursors, as well as the use of preformed nanoparticles as nanobuilding blocks for the fabrication of porous materials.

2.3 Materials

Throughout the literature, silica and silica-based materials have dominated the arena of porous materials. The simple reason lies in the fact that silica usually adopts an amorphous, glass form. It can form homogeneous glasses over a large length scales. The hydrolysis and condensation of silicon alkoxides can be better controlled as compared to

other metal alkoxides. Similar to water, SiO_4 tetrahedra show affinity towards surfactants and amphiphiles, which support the self-assembly process and the formation of ordered structures by the liquid crystal templating approach. Even though the mesoporous and macroprous silica materials have been appreciated from a aesthetic point of view, they have not found as much use as in terms of applications due to there amorphous nature. Many other transition metal oxides such as TiO_2, ZrO_2, CeO_2, Fe_2O_3, WO_3, or pervoskites are among the more interesting candidates in regards to their application in various fields. In the present work, TiO_2-based materials and CeO_2-ZrO_2 solid solution systems are investigated.

2.3.1 Titanium dioxide (TiO_2)

Titanium dioxide or titania is one of the most widely found oxides in the mineral form. TiO_2 exists in three different polymorphs: brookite, anatase and rutile. Anatase and rutile are the more common forms. Both of them have a tetragonal crystal structure but different lattice parameters. Brookite on the other hand is a less common polymorph having an orthorhombic crystal structure. In all the three modifications titanium has a co-ordination number of six and exhibits octahedral symmetry. Though all the polymorphs of TiO_2 can be obtained in stable form at ambient conditions, rutile remains the thermodynamically most stable form. Anatase and brookite are transformed into rutile upon heat treatment at high temperatures ranging from 400ºC to 1000ºC. Both anatase and rutile have a high refractive index of 2.5-3.0 and 3.87 respectively and hence can scatter light better than other materials such as alumina or silica. For this reason, TiO_2 and in particular rutile has been extensively used in the production of pigments. The world market for TiO_2-based pigments is as huge as four million tons per year [45]. The

high refractive indices of these substances also make them attractive candidates for applications in opto-electronics. By far the most actively pursued applied research on titania is its use for photo-assisted degradation of organic molecules. Anatase and rutile are semiconducting in nature with a band gap of 3.23 eV and 3.033 eV respectively. The electron–hole pair that is created upon irradiation with light radiation may separate and the resulting charge carriers might migrate to the surface where they react with the adsorbed water and oxygen to produce radical species. Out of the two, anatase is more active as compared to rutile [46]. Hence, it is desirable to have the anatase phase in the catalyst systems. Reports show that addition of small quantities of metal oxides such as ZrO_2, SiO_2, or In_2O_3 [47-49] retards the anatase to rutile transformation.Semiconducting metal oxides may change their conductivity upon gas adsorption. This change in the electrical signal is used for gas sensing. TiO_2 is not used as extensively as SnO_2 and ZnO, but it has received some attention as an oxygen gas sensor, e.g., to control the air/fuel mixture in car engines [50, 51].

In general TiO_2 is a material with interesting properties and wide range of possible applications.

2.3.2 Cerium dioxide

Cerium dioxide (CeO_2) or generally called ceria is a rare-earth oxide. CeO_2 has a cubic fluorite type structure. Cerium shows two stable oxidation states Ce^{4+} and Ce^{3+}. Unlike the other rare-earth oxides, it does not have a stable sesquioxide, Ce_2O_3. Nevertheless, because of its ability to shift between Ce^{4+} and Ce^{3+} reversibly, CeO_2 acts as a good oxidizing agent. Furthermore, due to this inherent property, CeO_2 can generate oxygen vacancies while still retaining the cubic fluorite structure. As there are no other

polymorphs for CeO_2 it can act as a thermally stable support. Apart from this, studies show that CeO_2 increases thermal stability of the supports, but also favours noble metal dispersion, promotes steam reforming and water gas shift reactions. Due to its ability to switch between Ce^{4+}/ Ce^{3+} states it can store and release oxygen at oxygen rich and lean environment respectively at high temperatures [52]. It can promote CO removal by employing lattice oxygen. All these properties make CeO_2 as ideal candidate for an auto exhaust catalyst, catalyst for the reforming reactions and for the fuel cell applications. Other applications of CeO_2 include abrasive for polishing glass due to its high hardness index of about 6, and oxidizing agent in sunscreens due to the strong UV absorption property.

2.3.3 CeO_2-ZrO_2 binary system.

In order to enhance the inherent properties of CeO_2, addition of other rare-earth oxides and transition metal oxides has been tried [52]. Of all the combinations explored, the CeO_2-ZrO_2 system was best in terms of performance.

Before discussing about the CeO_2-ZrO_2 system in detail, let us see some basic properties of ZrO_2. ZrO_2 exists in three stable crystal modifications, monoclinic, tetragonal and cubic. At ambient condition monoclinic is the stable phase. It can be transformed reversibly at higher temperature to the tetragonal and cubic phase as shown below [53].

ZrO_2 can be stabilized in the tetragonal and cubic phase at room temperature by doping with di-, tri- and tetravalent cations such as Ca^{2+}, Y^{3+}or Ce^{4+}. It has been found that the CeO_2-ZrO_2 binary system exhibits solid solution formation over a wide range. CeO_2 has a

cubic fluorite structure in which the Ce atom has a co-ordination number of eight. The structural changes occurring with increase in zirconium content are depicted in Fig. 2-2 (a). When a small amount of zirconium is introduced in the lattice, it results in the shrinkage of the unit cell due to the smaller size of Zr^{4+} (ionic radius = 0.84 Å) as compared to the larger Ce^{4+} (ionic radius = 0.97Å). The strain also creates oxygen vacancies. With increase in zirconium content the distortion forces increase resulting in the formation of the tetragonal phase. Pure ZrO_2 shows a monoclinic phase with a co-ordination number of seven for the Zr atoms. This is consistent with the small ionic radius of Zr and the strong covalent character of the Zr-O bond.

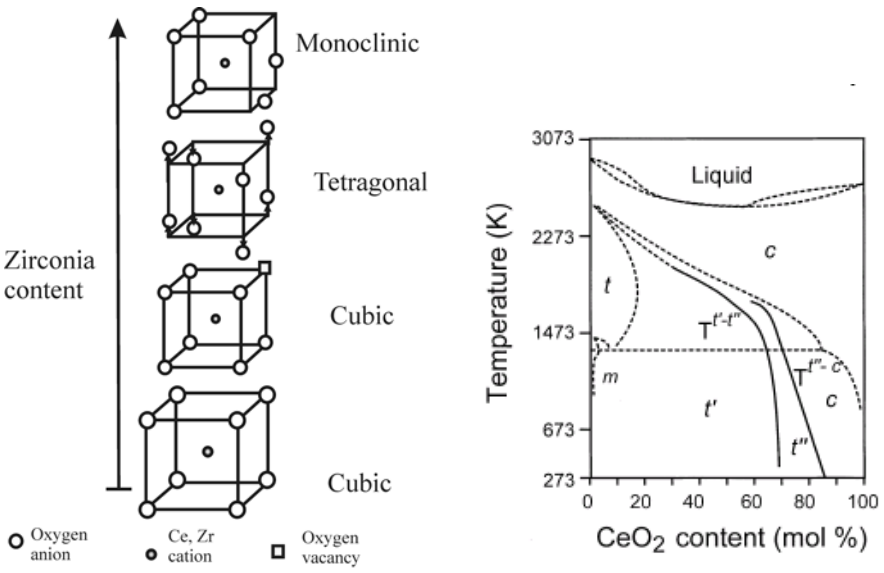

Figure 2.2 (a) Structure evolution in the CeO_2-ZrO_2 system with increase in zirconium content (b); phase diagram of CeO_2-ZrO_2 binary system adopted from Reference [53]

The exact appearance of the phase diagram is still a matter of debate. The main reason is that besides thermodynamically stable phases a number of metastable phases have been

reported. From the phase diagram it can be seen that for a CeO_2 content less than 10 mol% a monoclinic phase exists, while for CeO_2 content higher than 80 mol% a cubic phase is found. The phase composition of intermediate compositions is still unclear. Three different tetragonal phases *t, t'* and *t"* are mainly identified. Of these, *t* is the stable tetragonal phase, which can be identified by XRD. The *t'* and *t"* are metastable tetragonal phases, which are identified by Raman as it is more sensitive in getting information on the local structure. *t"* is also called the pseudo cubic phase as there is no real tetragonality in the structure. The oxygen atoms are slightly displaced from their position in the cubic conformation.

CeO_2-ZrO_2 systems have attracted a lot attention due the formation of defect structures. Mainly the tetragonal and the modified cubic structures both of which have oxygen vacancies act as good oxide ion conductor and hence are useful for fuel cell applications and for automotive exhaust catalysts. CeO_2-ZrO_2 compositions are more stable towards sintering and loss of surface area than CeO_2 alone, which makes it ideal for high temperature applications.

In general CeO_2 and CeO_2 based systems have been extensively studied and excellent reviews and books are available which discuss all the different aspects from structural properties to catalytic applications [52, 54-57].

2.4 Applications

2.4.1 Semiconductor photocatalysis

The phenomenon of semiconductor photocatalysis has been known for a long time. The semiconductor zinc oxide attracted a great deal of attention at the turn of this century as a

photo-sensitizer for the decomposition of organic compounds and as a sensitizer for a number of inorganic photoreactions [58]. In 1972 Fujishima and Honda demonstrated photocatalytic splitting of water using a TiO_2 electrode. Since then extensive efforts to understanding and enhancement of photocatalytic efficiency of TiO_2 have been carried out. The schematic view of processes occurring during photoreaction is depicted in Fig. 2-3. The origin of semicoductor photocatalysis lies in the fact that the energy diagram of semiconductors consists of a valence band and a conduction band, which is separated by certain fixed amount of energy between 0,1 and 4 eV, called as the band gap.

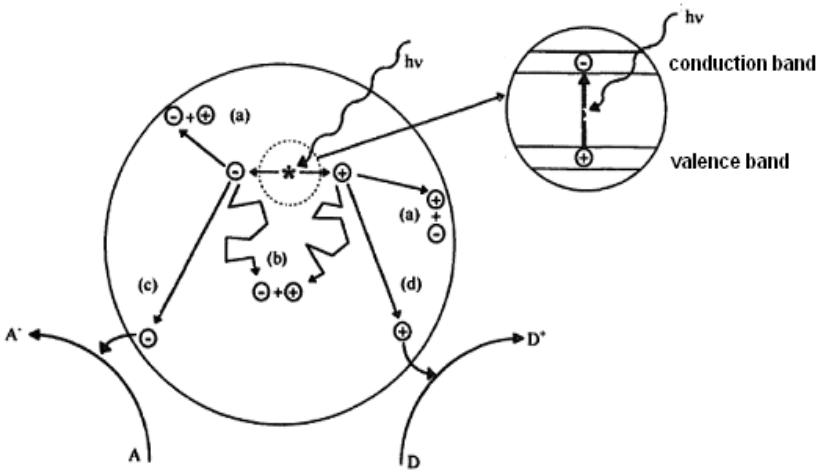

Figure 2.3 Major processes occurring in photocatalysis: * generation of electron hole pair, (a) electron hole pair recombination on the surface and (b) inside the bulk, (c) reduction of an electron acceptor A by an electron, (d) oxidation of a electron donor D by the hole

When light of appropriate energy is introduced on the semiconductor, it may result in excitation of an electron from the valence band into the conduction band leaving a positive hole in the valence band. This pair of electron and hole may be utilized in

carrying out redox reactions. During photocatalysis, light does not act as a catalyst but is rather consumed during the reaction. So many researchers like to call this phenomenon as photoreaction rather than photo catalysis.

During the photo excitation the electron excited into the valence band can fall back immediately, recombining with the hole in the valence band. On the other hand the electron and the hole may separate and travel within the matrix. As shown in Fig. 2.3 they can either recombine in the bulk (b) or on the surface (a). Those reaching the surface may also interact with the species in the vicinity of the surface and result in the reduction and oxidation reactions by the electron and the hole respectively [46, 59].

There are lots of factors that affect the photocatalytic properties of a semiconductor material. First thing is the size of the band gap. If the band gap is very large, the excitation radiation used should also have high energy. Secondly the position of the band gap is important. For a photocatalytic reaction occurring in an aqueous medium two sets of reactions are illustrated:

$$e^- + O_2 \longrightarrow O_2^{\bullet -}$$

$$2O_2^{\bullet -} + H_2O \longrightarrow H_2O_2 + O_2 \qquad \text{Reaction-1}$$

and

$$h^+ + H_2O \longrightarrow OH^\bullet + H^+$$

$$h^+ + OH^- \longrightarrow OH^\bullet \qquad \text{Reaction -2}$$

Here e^- is the photo-generated electron and h^+ the photo-generated hole. Which reaction will take place on the semiconductor surface is decided by the potential of the conduction band and the valence band. If the potential of the valence band is more negative than the

reduction potential of oxygen the Reaction-1 occurs and if the potential of the valence band is more positive than the oxidation potential of water/ hydroxide ion then the Reaction-2 is probable. In the case of nanoparticles below a critical particle size, the size of the band gap is dependent on the size of the particle. This is called the quantum size effect. The materials like CdS and Fe_2O_3 undergo decomposition as a result of the photochemical reaction. This is called photo corrosion. The pH of the medium determines the position of the band gap of the semiconductor material. These are some of the parameters that influence the photoactivity of a semiconductor material.

Photo catalysis offers solutions to pressing environmental issues such as pollution and shortage of energy resources. Examples of most commonly explored reactions include complete photocatalytic decomposition of halogenated aromatic and non-aromatic organic compounds, which are found as pollutant in industrial and domestic wastewaters [60]. Degradation of poisonous inorganic compounds such as cyanides sulfides is also reported [61, 62]. Furthermore, deactivation of viruses and bacteria has been attempted [63-65]. Cleavage of water to produce oxygen and hydrogen comes as one of the solutions for fuel problems as hydrogen acts as a clean fuel for fuel cell applications [66].

Semiconductor photocatalysis thus offers various applications based on a simple and effective process. With materials like TiO_2, which is efficient, non-toxic and cost effective, it is possible to make the technology available for the common people.

2.4.2 Steam reforming of methanol

As the reserves of conventional fuels are plummeting, the need to find alternative fuels is rising. One of the most popular alternative fuel is hydrogen. Reaction of hydrogen with oxygen gives water and a large amount of energy is released. Production of hydrogen can be done using photocatalyis. But the system is not suitable for production at very large scales. Secondly, regarding the hazards in the handling and storage of hydrogen it is desirable to have sources of hydrogen, which can yield hydrogen in situ for its use in applications like fuel cells. The remedy comes in the form of reforming reactions in which a hydrocarbon compound is decomposed to yield hydrogen and carbon dioxide. One of the most widely appreciated reaction is the steam reforming of methanol. The main reactions involved during the reforming process are as follows:

$$CH_3OH + H_2O \rightleftharpoons CO_2 + 3H_2 \qquad \text{Reforming}$$

$$CH_3OH \rightleftharpoons CO + 2H_2 \qquad \text{Decomposition}$$

$$CO + H_2O \rightleftharpoons CO_2 + H_2 \qquad \text{water-gas shift reaction}$$

There has been a general debate about the sequence of reaction occurring during the reforming process. The reforming reaction was thought to be a combination of methanol decomposition reaction and water-gas shift reaction [67]. Later it was proposed that the reforming occurs in a single step [68]. Peppley *et.al* have given a detailed account of all the proposed mechanisms and concluded that the over all mechanism of reforming involves a combination of all three reactions [69].

Apart from the main three reactions, there are also some side reactions involved such as:

$$2CH_3OH \rightleftharpoons CH_3CHO + 2H_2$$

$$CH_3CHO + H_2O \rightleftharpoons HCOOH + CH_3OH$$

$$HCOOH \rightleftharpoons CO_2 + H_2$$

A large variety of catalysts for the steam reforming of methanol have been reported in the literature [69, 70]. The majority of these have been copper based catalysts. Mainly Cu-Zn containing systems were seen to be highly effective [68]. Among the other Cu-based catalysts, ZrO_2 containing catalysts have shown interesting properties [70]. The main drawback in these systems is that the transformation of ZrO_2 from the tetragonal/cubic to the monoclinic phase results in a loss of surface area and consequently, considerable reduction in activity. As discussed in the previous section, ZrO_2 can be stabilized in the tetragonal or cubic phase by doping or addition other metal oxides to prevent the loss of activity due to phase transformation.

The reforming reactions are carried out at temperatures between 150ºC-400ºC. The ideal catalyst for reforming reactions is one that works at low temperatures. At higher temperature, the production of carbon monoxide increases can poison the proton-exchange-membrane (PEM) fuel cell, which uses the H_2 from reforming reaction as anode feed gas. Secondly, from an environmental point of view, it is also important to have low CO emission, as it is extremely poisonous.

3 Methods

3.1 Nitrogen sorption studies

Specific surface area of porous materials can be measured by using the phenomenon of physical adsorption of gases onto the surface at low temperatures. For porous materials, this method not only gives information about specific surface area of the material but also on the pore sizes and pore volume, given the pore sizes are in the range accessible by this method [6].

The gas used for the measurement (adsorbate) should have certain characteristic features. It should be chemically inert towards the solid sample (adsorbent), it should have saturation vapour pressure large enough to carry out the measurements accurately at working temperatures and the shape of adsorbate molecule should be close to spherical symmetry. In this regards, nitrogen is most widely used as adsorbate gas. Other gases used for the measurement are krypton, argon, benzene and carbon dioxide.

The nitrogen sorption measurements are carried out at constant temperature of 77.35 K, which is the boiling point of liquid nitrogen. For the measurement, the sample is evacuated completely and then, small amounts of gaseous adsorbate are fed gradually and adsorbed on to the sample. The volume of gas adsorbed V_A is taken as volume of the same amount of gas at standard temperature and pressures condition (STP). The partial pressure of gas P above the sample surface is measured relative to the atmospheric pressure P_0 at a constant temperature. The plot of the volume adsorbed V_A versus relative pressure P/P_0 gives the so-called adsorption isotherm. In general, depending on the nature of the adsorption isotherm, they are classified into six different types of isotherms called as Brunauer classification, which has been also accepted by IUPAC [71]. They are as shown

in Fig. 3.1. In case of non-porous materials or materials with large pores, an isotherm of type-II is observed. In this case, as the gas is allowed to come in contact with the sample surface at lower relative pressure, P/P_0, the gas is adsorbed onto the surface forming a

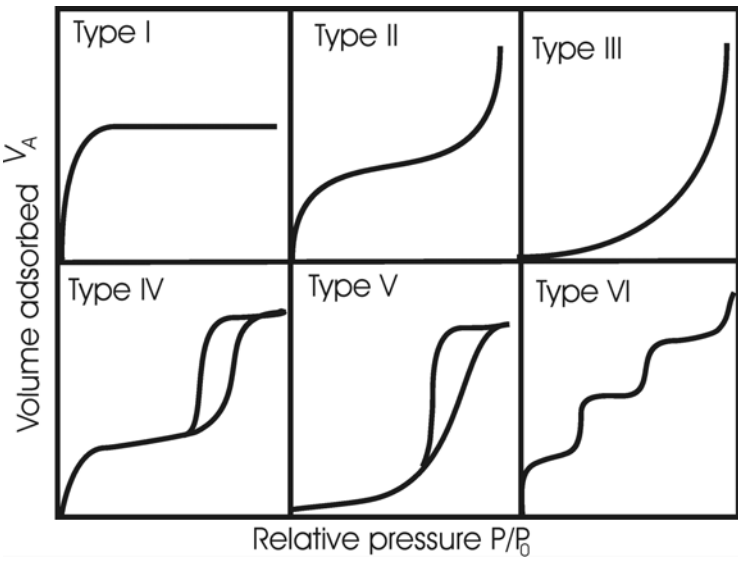

Figure 3.1 Types of isotherms according to the Brunauer classification.

monolayer, while pressure increases very slightly. This is reflected in sharp rise of the curve. After the monolayer is formed, the added gas is weakly bound to this layer forming additional layers, which is followed by subsequent increase of pressure and results in flattening of the curve. As the relative pressure, P/P_0, approaches atmospheric pressure, the gas condenses to a liquid and the curve shows a rise again.

In case of mesopores, the condensation occurs at lower relative pressures. In these pores the monolayer of nitrogen molecules form a curved interface which acts as nucleation site for condensation of gaseous nitrogen. According to Kelvin equation (Equation 3-1), the vapour pressure on the curved liquid surface is always less than the liquid with plane surface.

$$\ln\left(\frac{P^*}{P_0}\right) = -\frac{2\gamma V_0 \cos\theta}{RTr_m} \qquad \text{Equation 3-1}$$

P^* = Critical condensation pressure

γ = Surface tension of the adsorbate

V_0 = Molar volume of the adsorbate

θ = Contact angle of the condensed adsorbate with the sample surface

r_m = Mean radius of curvature

Figure 3.2 Schematic representation of a section through a cylindrical pore with nitrogen molecular monolayer on the pore wall.

The critical pressure P^* at which the adsorbate condense is smaller than the normal pressure P_0. Secondly, it is proportional to the mean radius of curvature and hence to the pore radius. So the smaller the pore radius, the lower will be the critical condensation pressure. For nitrogen, the contact angle is taken as $\theta = 0°$, which gives $\cos\theta = 1$. For a curved liquid interface, two radii of curvature are defined, which are perpendicular to each other. In a typical case of cylinder with both the ends open, they are defined as shown in Fig. 3.2. The mean radius of curvature in general is defined as $\frac{2}{r_m} = \frac{1}{r_1} + \frac{1}{r_2}$.

For cylinder with both the ends open, $r_1 = \infty$, so $r_m = 2r_2$. If we take into account the

thickness of the monolayer, the corrected mean radius of curvature is $r_m = 2\ (r_2 - t_{P/Po})$, so the pore radius can be given by the Equation 3-2:

$$r_2 = -\frac{\gamma V_0}{R T \ln\left(\frac{P*}{P_0}\right)} + t_{P/Po} \qquad \text{Equation 3-2}$$

This equation associates the pore radius r_2 of the given cylindrical pore with the relative pressure P/P_0 at which the condensation occurs.

For mesopores in the range of 2-10 nm, with the use of nitrogen as adsorbate, the relative condensation pressure lies in the range of 0.4-0.9. This type of system shows a Type-IV isotherm, where the curve is flattened after the first initial inflection and then at relative pressures, where condensation occurs, it rises up again.

The process of adsorption and desorption occurs in a different way, which leads to hysteresis. The nature of this hysteresis is also different in the case of pores, where the size of pore opening is different than the inner pore size. For pores smaller than 2 nm (micropores), a large part of the pore volume is filled during the monolayer formation. The capillary condensation in these pore size areas occurs at very low relative pressures. Therefore, the microporous samples show an isotherm of Type-I. Capillary condensation in these pores results in a sharp increase in the curve at very low relative pressure. After that, the relative pressure increases without an increase in the amount of adsorbed gas as there is no place for more adsorption to occur. As a result of this, the curve remains flat.

The other types of isotherms are rare and uninteresting from the analytical point of view. Type-III and Type-V isotherms originate from a weak gas-solid interaction. Non-porous or macroporous materials give a Type-III isotherm, while mesoporous or microporus

materials give isotherms of Type-V. The isotherm of Type-VI, called stepped isotherm, is also rare and is particularly of theoretical interest.

The region of the isotherm up to which there is no capillary condensation, i.e., the low relative pressure region of the Type-II and Type-IV isotherm, gives the account of specific surface area of the samples. Various theories have been put forth to calculate the specific surface area of the sample. I. Langmuir in 1918 proposed the first theory [72]. This theory gives the relation between volumes of gas adsorbed and the surface area of the sample based on the kinetic consideration of formation of a monolayer of the adsorbate over the sample surface.

S. Brunauer, P.H. Emmett and E. Teller improved this model by taking into account the adsorption of multiple layers of adsorbate molecules. This theory is widely acknowledged and is commonly known as BET-method, named after its inventors [73]. Equation 3-3 is called the BET equation:

$$\frac{\frac{P}{P_0}}{V_A\left(1-\frac{P}{P_0}\right)} = \frac{1}{V_m C} + \frac{C-1}{V_m C}\left(\frac{P}{P_0}\right) \qquad \text{Equation 3-3}$$

V_m = Volume of gas needed to form a monolayer on the entire sample surface

C = Constant which is related to enthalpies of adsorption H_A and condensation H_C given as $C \propto \exp\left(\frac{H_A + H_K}{RT}\right)$

The adsorption data gives the values for the terms on the left hand side of Equation 3-3, from which the parameters C and V_m on the right hand side of the equation can be easily calculated. From the volume of gas forming monolayer V_m, the mass of the sample and

the area per molecule of the adsorbate gas, one can calculate the surface area of the sample using Equation 3-4:

$$SA_{BET} = \frac{V_m N_A \sigma}{V_0 m} \qquad \text{Equation 3-4}$$

SA_{BET} = Specific surface area from BET method

N_A = Avagadro's number

σ = Area per molecule of the adsorbate gas

m = Mass of the sample

3.2 Electron microscopy

Resolving limit of a microscope is defined as the minimum detectable distance, Δx between two points, so that they are recognized as separate objects. In 1900 E. Abbe showed that the wavelength of electromagnetic radiation λ, the angle of the incident beam with the objective α and the refractive index of the medium n between the objective and the sample are related to the resolution limit as given by Equation 3-5:

$$\Delta x = \frac{\lambda}{n \sin \alpha} \qquad \text{Equation3-5}$$

The refractive indices of medium used generally lies below 2 and the maximum possible value for $\sin\alpha = 1$. So the maximum resolution that can be achieved by a microscope using visible light ($\lambda_{vis} > 400$ nm) is around 200 nm. Therefore, in order to achieve a better resolution, electromagnetic radiation sources with a smaller wavelength must be used.

Around 1930 E. Ruska developed the electron microscope based on De Broglie's principle of wave-particle duality. It states that associated with every particle there is a wave, wavelength of which is given by the Equation 3-6:

$$\lambda = \frac{h}{mv} \qquad \text{Equation 3-6}$$

h = Planck's constant

m = rest mass of the particle. In the case of electrons $m_e = 9.109 \times 10^{-31}$kg

v = velocity of the particle

The speed of electron v, accelerated by an electric field U is given in Equation 3-7:

$$\frac{1}{2} m_e v^2 = eU \qquad \therefore v = \sqrt{\frac{2eU}{m_e}} \qquad \text{Equation 3-7}$$

e = charge on electron = 1.602×10^{-19}C

For the acceleration voltage U = 100 kV, the De Broglie wavelength of the electrons using above equation is found to be 0.0037 nm. Accordingly, the theoretical resolution of electron microscopes is of three order of magnitude higher than that of light microscopes. Considering the fact that electrons can get scattered by any particle in their way, electron microscopes are operated at high vacuum.

3.2.1 Transmission electron microscopy (TEM)

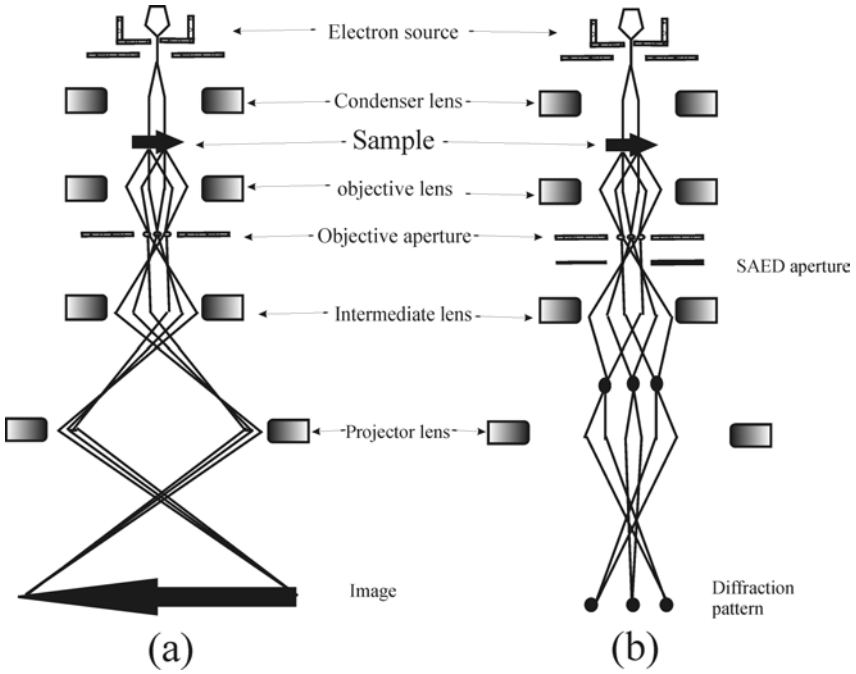

Figure 3.3 Schematic diagram of a transmission electron microscope: (a) TEM imaging set-up, (b) selected area diffraction pattern processing set-up.

The basic set-up of a transmission electron microscope is shown in Fig. 3.3. The TEM works in a similar way as a light microscope [74]. Instead of a light beam, a beam of electrons is used and magnetic lenses replace the optical lenses. As the electrons are charged, they can be deflected by the application of an electric or magnetic field. A beam of electrons can be made to diverge, or converge at a point using a magnetic field, which is analogous to the functioning of an optical lens.

An electron gun is used as source. It consists of a heated cathode, which emits thermal electrons. These thermal electrons are then accelerated using a high electrical potential of 60 to 200kV. The beam of electrons is adjusted by the use of condenser lenses to get a parallel beam, which is allowed to fall on the sample. The magnification can be adjusted

by adjusting the beam width, which in turn depends on the strength of the condenser lens. The electrons transmitted through the sample are then passed through a set of objective lens, objective aperture, intermediate lens and a projector lens to give a highly magnified image of the sample. As the electrons are scattered by the atoms in the sample, the darker part of the image correspond to the presence of matter, while lighter parts indicate the absence or thinning of material. The contrast depends upon the elements present in the sample. Heavy elements scatter more and hence give greater contrast.

In the case of crystalline samples, change in the set-up can give an electron diffraction pattern instead of the sample image. As shown in Fig. 3.3 (b), additional aperture limiting the area of beam and change in the strength of the intermediate lens in accordance with the objective lens gives a so-called selected area electron diffraction pattern (SAED) of the sample. The pattern appears as a dot pattern if the area under investigation is a single crystal. In case of a polycrystalline sample, a ring pattern is observed instead. The pattern is characteristic of the sample material and its orientation with respect to the beam. It gives information on crystal structural parameters such as the *d*-spacing between the crystal planes and symmetry.

For the TEM investigation, the samples are laid on a copper grid covered with thin carbon film. The sample thickness should be very small. Typically it should be less than 100 nm. In case of finely powdered samples, the powder is dispersed in a suitable solvent and a drop of it placed on the grid. Removal of the solvent by evaporation results in deposition of the sample on the grid. Alternatively, for larger objects ultramicrotomy technique is used. In this technique, the sample is first embedded in a polymer matrix and then thin slices of it are cut using a diamond knife. The sections are around 30-100 nm in thickness. These slices are then laid on the grid for analysis.

3.2.2 Scanning electron microscopy (SEM)

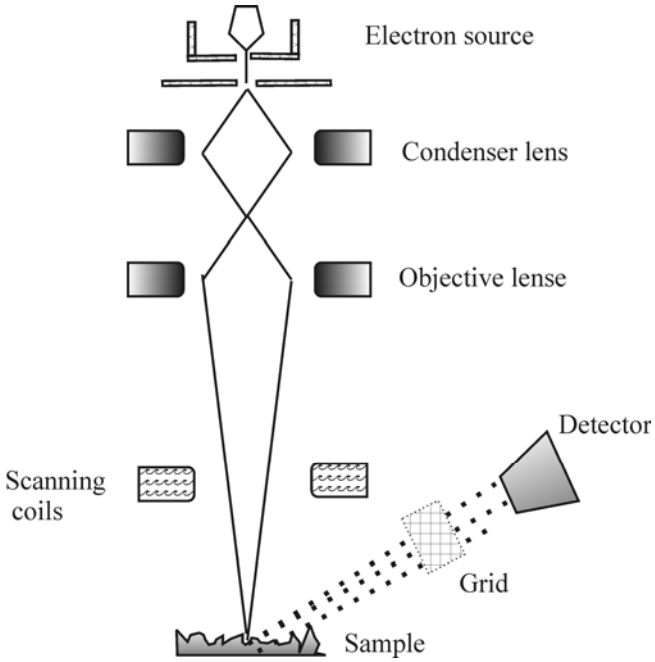

Figure 3.4 Schematic set-up of scanning electron microscope.

Scanning electron microscopy (SEM) gives information about the external morphology of a material [74]. The electron beam used for SEM possesses lower energy as compared to TEM. Typical acceleration potentials used are between 1-50kV. Using a set-up of a number of lenses, the electron beam is focused on to the sample in a single spot of cross section 2-10 nm. A set of scanning coils is used to control the position of the spot on the sample surface. By changing the potential applied to the scanning coils, the beam is made to scan the whole sample line by line in a quick succession. The bombarding of the sample with electrons leads to generation of X-rays and emission of secondary electrons. These effects can be used in probing the sample surface. Usually the secondary electrons are used in the image generation. The secondary electrons are selectively attracted towards a detector through a grid held at a low positive potential with respect to the

specimen. The electron detector counts the number of secondary electrons that arrive per unit time and translates this count rate into an electrical signal. The final image is built up from the information on the number of electrons collected from each point.

The number of secondary electrons reaching the detector depends upon surface topology. Based on geometrical considerations, secondary electrons generated at the edges and at convex surfaces have higher probability to escape from surface and reach the detector, while secondary electrons from shallow surfaces have the least probability to escape from surface and reach the detector. The area from where more secondary electrons are collected appears brighter, while the area giving a low secondary electron count appear dark. Through this contrast mechanism, we get a magnified image of the sample with topological details of the sample surface.

It is important to have a high amount of secondary electrons generated from the sample surface in order to get good contrast in the image. As the sample is bombarded with electrons, charge is built on the surface and if the sample is non-conducting it is not dissipated. As a result of this, the sample appears bright everywhere. To stop the charge from building up, the sample needs to be conducting. For these reasons the samples are coated with a very thin layer of metal such as gold or palladium prior to analysis.

3.3 Wide angle x-ray scattering (WAXS)

Crystalline materials consist of a periodic arrangement of repeating units of atoms in space. The simplest portion of the structure, which is repeated, and shows its full symmetry, is defined as the unit cell. The basic unit cell is a parallelepiped with the side lengths and angles as defined in Fig. 3.5. The angles and lengths used to define the size of the unit cell are known as the unit cell parameters. Depending on the symmetry of the unit cell, which is in turn defined by lattice parameters, seven crystal systems are identified. These are cubic, tetragonal, orthorhombic, trigonal, monoclinic, triclinic and hexagonal. These crystal classes are further sub-divided into thirty-two crystal classes depending on the position of atoms in the space. Repeating unit cells form a crystal lattice in which each atom represents a lattice point. Planes or set of planes parallel to each other can be drawn using the lattice points. These planes are labeled using Miller indices, *h, k* and *l*, which are integers given by the reciprocals of the fractional intercepts along each of the cell directions [75].

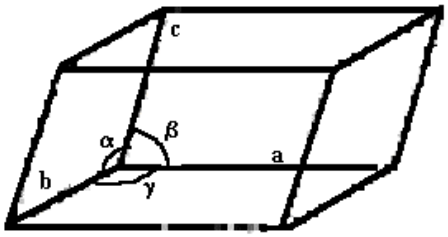

Figure 3.5. Schematic unit cell.

When X-ray interacts with an electron in the atom, the electrons act a secondary source and emit X-rays of the same frequency. This phenomenon is called as Thomson scattering. The extent of scattering depends on the number of electrons possessed by the atom. The emitted wave travels in all the directions as a spherical wave front. In case, if there are two or more sources in vicinity, the secondary wave interfere with each other to give increase or decrease in intensity due to constructive or destructive interference

respectively, depending on the phase difference at the point of interference. If the secondary sources are periodically arranged, the interference between the secondary waves gives high intensity due constructive interferences only at certain angles while, at other angles, destructive interference leads to the loss of intensity.

Bragg's approach was to consider the crystals as being built in layers, or planes, such that each acts as a semi-transparent mirror. The planes allow some of the X-ray beams to be reflected at the same angle as the angle of incidence (Fig. 3.6).

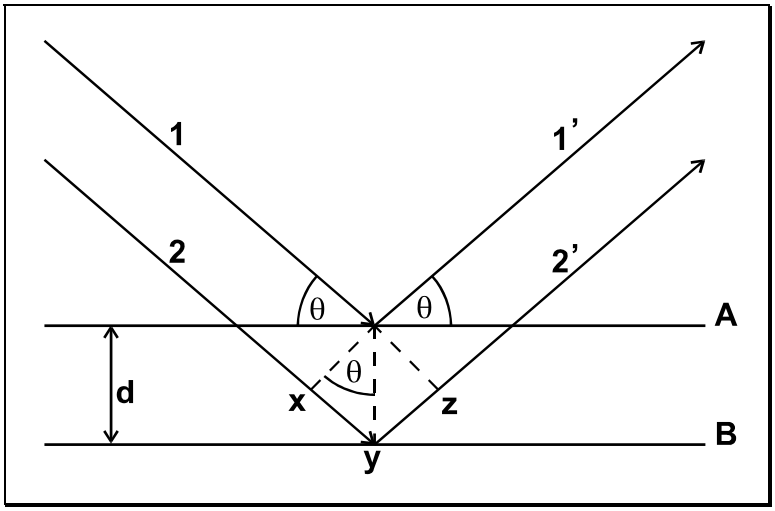

Figure 3.6 Schematic representation of derivation of Bragg's law.

The incident beams 1 and 2 are reflected by planes A and B to form beams 1' and 2', the condition under which these beams are in phase with each other is approached as follows. Beam 2 2', shown in Fig. 3.6, has to travel a further distance, xyz, as compared to beam 1 1'. For 1'and 2' to be in phase with each other, xyz must equal *n*, where *n* is an integer

and is equivalent to the number of wavelengths. The perpendicular spacing, d, and angle of incidence, θ, called the Bragg angle, are related by:

$$xy = yz = d \sin \theta$$

$$\Rightarrow \quad xyz = 2\, d \sin \theta$$

$$\text{Since} \quad xyz = n\lambda$$

$$\Rightarrow \quad n\lambda = 2\, d \sin \theta \qquad \text{Equation 3-8}$$

When Equation 3-8, Bragg's Law, is satisfied, the reflected beams are in phase and thus constructively interfere. If the angle is not correct then interference of a destructive nature will occur. It can be seen that many solutions are possible, i.e., n = 1,2,3, which result in peaks of higher order.

3.3.1 The powder X-ray diffraction method

The basic principle of the powder method is shown in Fig. 3.7. A powder sample is a random assembly of crystallites, a monochromatic beam of X-rays strike the powdered sample such that every orientation is possible. As a result, for every diffraction plane there are some crystals correctly oriented at the Bragg angle and hence some diffraction occurs.

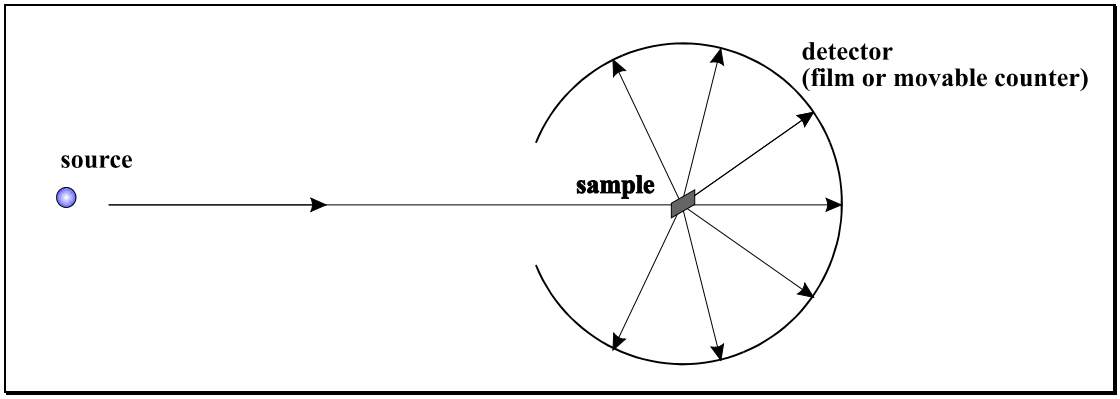

Figure 3.7 A schematic representation of the powder method.

The diffracted beam can be detected by one of two means, a photographic plate surrounding the sample, or a movable detector, connected to a computer. The original photographic method, called the Debye-Scherrer method, is little used in modern X-ray diffraction practices. A modern diffractometer can collect accurate positional and intensity data both quickly and easily. This enables the phase composition of crystalline samples to be determined in less than an hour, with the recorded pattern being matched against standard patterns.

3.3.2 Diffractometer

The collection of X-ray powder diffraction data is routinely carried out on a diffractometer, such as shown in Fig. 3.8:

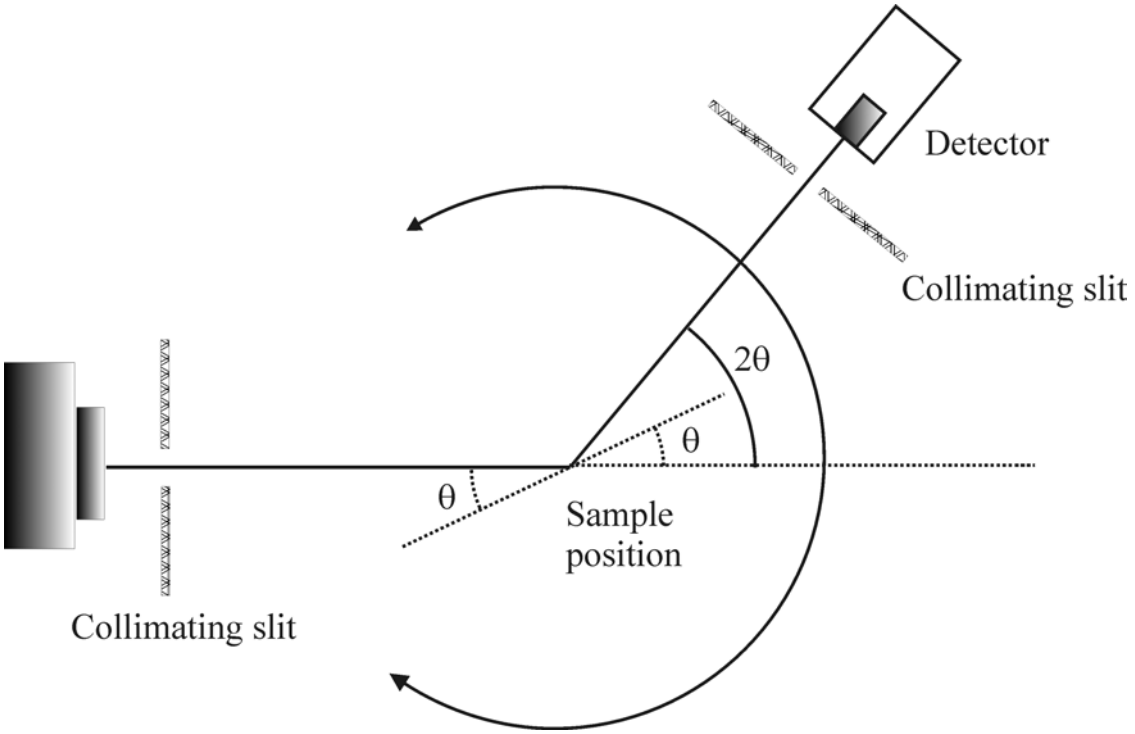

Figure 3.8 Schematic representation of a standard X-ray diffractometer.

The X-rays are generated in an X-ray tube, where electrons are bombarded against a metal target, usually copper. This bombardment results in the evolution of X-rays. The X-rays are then collimated into a pencil like beam. The beam then passes through the sample, which is rotating around a central axis, and is diffracted. This diffracted beam is then passed through a further set of collimation slits to remove X-ray scattering. The X-rays are then counted in a detector moving around the central axis, at an angle of rotation twice that of the sample.

3.3.3 Peak intensities

There are many factors, which can affect the peak intensity. A few are described below.

i) Structure Factor.

The peak intensity is influenced by the position of the atom in the unit cell and the atom type. If an atom has a high atomic number then it will scatter X-rays better than an element with a low atomic number, e.g., Cs scatters better than Li giving greater intensity.

ii) Multiplicity Factor.

For a cubic system, lattice planes such as (013), (031), (103), (130), all have the same d-spacing where a = b = c. In a powder XRD pattern the variable co-ordinate is the *d*-spacing. Therefore reflections, which give rise to the same d-spacing will be superimposed. As a result, a more intense peak will be observed.

iii) Preferred orientation.

This occurs if the powder is poorly ground or if the powder is not completely oriented randomly. This effect can cause some intensities to be increased while others are decreased.

iv) Temperature factor.

Thermal vibrations of atoms cause a decrease in the observed peak intensity with an increase in background scattering. This effect is usually only important for experiments performed at high temperature.

3.3.4 Diffraction pattern evaluation

Usually, X-ray diffraction pattern of a sample is evaluated by calculating the *d* values corresponding to each peak and matching with the known patterns from data bases such as Joint Committee on Powder Diffraction Studies (JCPDS) database.

3.3.5 Crystallite size measurement

It is possible to measure the crystallite size from X-ray powder diffraction patterns using the effect of line broadening on the diffraction pattern. The relationship between the mean dimension of the crystallites in a powder, *D*, and the pure X-ray diffraction broadening, β, was first determined by Scherrer, and is discussed in detail by Klug and Alexander [75]. Scherrer related the mean dimension, *D*, to the pure diffraction broadening, β, by Equation 3-9:

$$D = \frac{K\lambda}{\beta \cos\theta} \qquad \text{Equation 3-9}$$

K = Constant

θ = The diffraction angle

λ = The wavelength of the X-ray

3.4 Vibrational spectroscopy

Vibrational spectroscopy is a powerful tool to investigate the symmetry of molecules, the nature of bonding and interactions of atoms within the molecule. It is useful for qualitative as well as quantitative investigations [76, 77].

The simplest model of an atom bound in a molecule is given as large mass *m* by a weightless spring. The force *F* that is necessary to move the atom by a certain distance *x* from an equilibrium position is proportional to the force constant *f*, a measure of the strength of bond by Hooke's law given in Equation 3-10:

$$F = -f \cdot x \qquad \text{Equation 3-10}$$

By Newton's law $F = m \cdot \frac{d^2x}{dt^2}$

$$\Rightarrow \qquad m \cdot \frac{d^2x}{dt^2} = -f \cdot x \qquad \text{Equation 3-11}$$

One of the solutions of this second order differential equation is given as

$$x = x_0 \cdot \cos(2\pi\nu t + \varphi)$$

$$\Rightarrow \qquad \frac{d^2x}{dt^2} = -4\pi^2\nu^2 x_0 \cos(2\pi\nu t + \varphi) = -4\pi^2\nu^2 x_0 \qquad \text{Equation 3-12}$$

Where ν is vibrational frequency and φ is the phase angle.

Combining Equation 3-11 and 3-12

$$4\pi^2\nu^2 m = f \qquad \text{or} \qquad \nu = \frac{1}{2\pi}\sqrt{\frac{f}{m}} \qquad \text{Equation 3-13}$$

If we consider a diatomic molecule, the mass m is called reduced mass of diatomic molecule with the masses m_1 and m_2 :

$$\frac{1}{m} = \frac{1}{m_1} + \frac{1}{m_2}$$ Equation 3-14

Thus the frequency of vibration of a diatomic molecule is given as

$$\nu = \frac{1}{2\pi}\sqrt{f\left(\frac{1}{m_1} + \frac{1}{m_2}\right)}$$ Equation 3-15

A diatomic molecule is said to have one vibrational degree of freedom as it can have only one mode of vibration. Similarly, a molecule containing *n* number of atoms will have 3n-6 degree of vibrational degrees of freedom. Part of the energy possessed by a molecule comes from the vibrational modes and a molecule can be excited from one vibrational energy level to the other by using radiation of certain frequency. Thus every molecule shows a characteristic vibrational spectra depending on the mode of vibration and the frequency of radiation used for excitation. In general, the vibrational frequency is given in wave number units $\tilde{\nu}$ (waves per unit length), which is reciprocal of the wave length λ.

3.4.1 Infrared (IR) spectroscopy

Infrared (IR) radiation is electromagnetic radiation that encompasses all the wavelengths between the visible and microwave regions of the electromagnetic spectrum. The IR region can also be subdivided into three smaller regions known as near-IR, mid-IR and far-IR, of which the mid -IR region of radiation with the frequency range of 4000 cm^{-1} to 400 cm^{-1} corresponds to the changes in fundamental vibrational levels of most of the molecules. Hence the radiations in this region are used to probe the vibrational behavior of the sample molecules.

IR radiations of frequency equal to vibrational frequency are absorbed only if a change in the dipole moment of the molecule is involved. The vibrations accompanying dipole moment change are thus termed as *IR active*, while those without change in dipole moment are *IR inactive.* A typical IR spectrum for any material is obtained by irradiating it with a range of IR radiations and then measuring the transmittance or absorption corresponding to individual frequency. The intensity of transmitted radiation is given by the Beer-Lambert law (Equation 3-16):

$$I = I_0 + \exp(-\varepsilon cl) \qquad \text{Equation (3-16)}$$

I = Intensity of transmitted radiation

I_0 = Initial intensity

ε = Extinction coefficient corresponding to given radiation

c = Concentration of sample

l = Thickness of the sample

In general, IR spectra are obtained by *Fourier transform infrared spectroscopy* (FT-IR), which is based on the interferometer originally designed by Michelson and a mathematical procedure developed by Fourier that converts response from the 'time' to the 'frequency' domain [77].

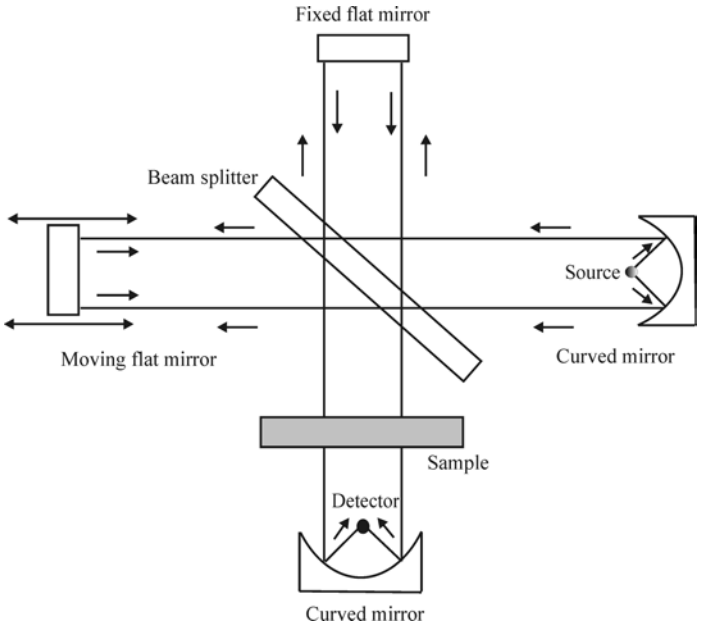

Figure 3.9 Sketch of the Michelson interferometer.

In the Michelson interferometer (Fig. 3.9), a parallel, polychromatic beam of radiation from a source is directed to a beam splitter, made from an infrared transparent material, such as KBr. The beam splitter reflects approximately half of the light to a mirror, known as the fixed mirror, which in turn reflects the light back to the beam splitter. The rest of the light passes through to a mirror, moving continuously, at a known velocity, back and forth along the direction of the incoming light and this is known as the moving mirror. Upon reflection from the moving mirror, radiation is then directed back to the beam splitter. At the beam splitter some of the light that has been reflected from the fixed mirror combines with light reflected from the moving mirror and is directed towards the sample. After passing through the sample, the radiation is focused onto the detector. The detectors are sufficiently fast to cope with time domain signal changes from the modulation in the interferometer

As the distance of the moving mirror from the beam splitter changes, different wavelengths of radiation are in-phase and out-of-phase at a frequency that is dependent both upon the rate at which the mirror moves and the frequency of radiation.

The complex pattern of overlaid sinusoidal waves of light (in the time domain) is known as an interferogram. The interferogram can be converted back to the original frequency distribution (spectrum) by means of a Fourier transform, which can be done very rapidly using a computer.

3.4.2 Raman spectroscopy

3.4.2.1 The Raman effect

The Indian physicist, C. V. Raman in 1928, discovered the effect. The Raman effect is most simply described as the inelastic scattering of light by matter. When light is scattered by a molecule there can be one of three outcomes:

1.Elastic (Rayleigh) scattering, where there is no net energy loss or gain to the incident light beam.

2.The light is scattered to lower energy and frequency (Stokes scattering).

3.The light is scattered to higher energy and frequency (anti-Stokes scattering).

When a beam of monochromatic radiation impinges on a sample, around 99.9% of the scattered light will be Rayleigh and only 0.1% will be Raman light. The proportions of the Stokes and anti-Stokes scattering are dependent on the vibrational energy population distribution before irradiation (and therefore temperature).

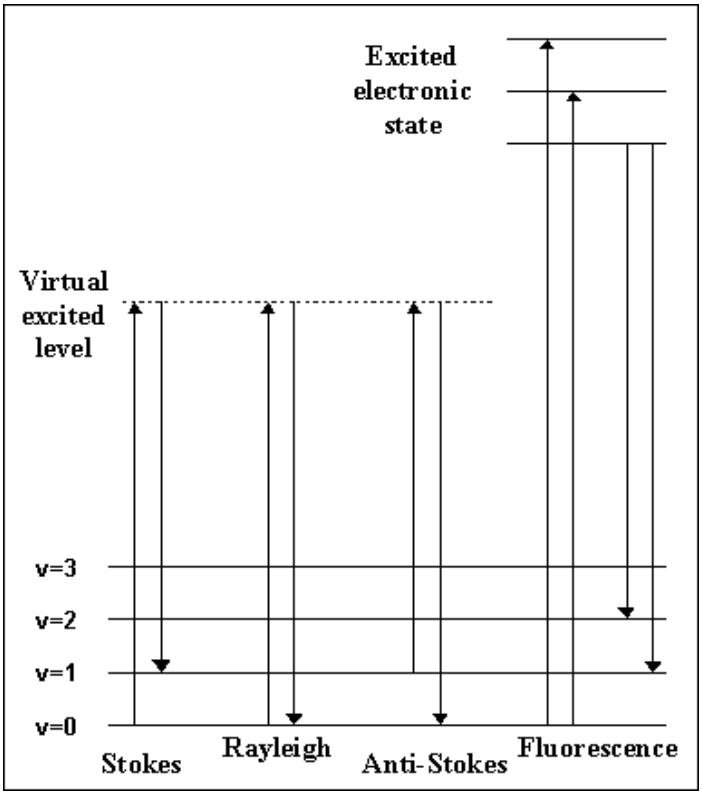

Figure 3.10 Schematic representation of various modes of scattering.

Raman spectroscopy is complementary to the IR spectroscopy [76]. The IR technique is based on the change in the dipole moment of the molecule while Raman effect is observed for only those modes of vibrations where change in the polarizability of the molecule occurs.

As the intensity of scattered radiation is very low, high intensity sources such as laser having wavelength in the visible region are used.

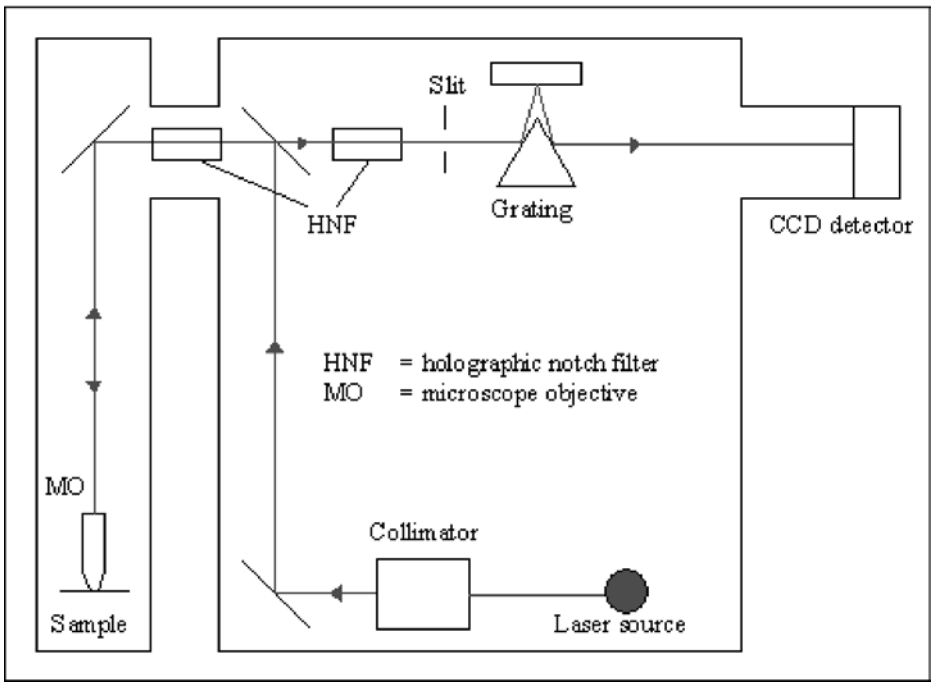

Figure 3.11 Schematic representation of a Raman spectroscope.

As shown in Fig. 3.11, the laser beam is passed through a collimator and then through a series of mirrors on to the sample through a microscope objective. The back-scattered radiations are collected through the same microscope objective and measured by a charge coupled device (CCD) detector. Holographic notch filters are used as beam splitter and to selectively filter out the Rayliegh light from the scattered radiation. The CCD detector is nothing but an array of small capacitors. These capacitors generate charges equal to the incident photons, which are then measured and obtained as a plot of frequency in wave number against scattering intensity. The excitation frequency is taken as zero and the values of Raman bands are assigned relative to it.

3.5 Analytical ultracentrifugation (AUC)

AUC, invented in 1920's by Thé Svedberg, is a very powerful and valuable method for the investigation of the physicochemical properties of macromolecules and colloids [78]. The various techniques used in AUC lead to the direct determination of molar masses, molecular weight distributions, shapes, particle sizes, interaction constants, sedimentation and diffusion coefficients.

When centrifugal force is applied on a solute particle suspended in a solvent, three different forces act on the particle, as illustrated in Fig. 3.12.

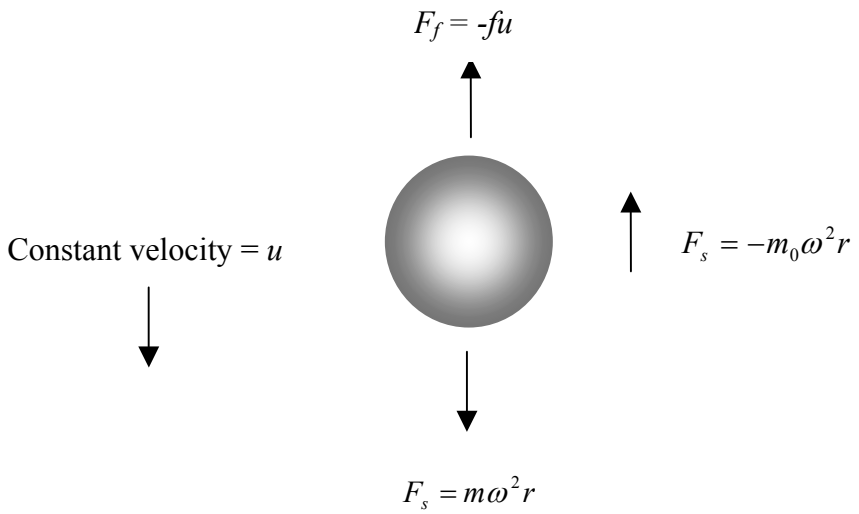

Figure 3.12 Forces acting on a solute particle under the influence of centrifugal force.

The centrifugal force F_s is given in Equation 3-17:

$$F_s = m\omega^2 r \qquad \text{Equation 3-17}$$

m = Mass of the particle

r = distance of particle from the axis of rotation

ω = Angular velocity

The buoyant force F_b is equal to the weight of displaced (Equation 3-18):

$$F_b = W = -m_0\omega^2 r = -\frac{m}{\rho}\rho_0\omega^2 r \qquad \text{Equation 3-18}$$

m_o = Mass of the solvent displaced by the particle = $m\nu\rho = M\nu\rho N_A$

ρ_0 = Density of the solvent

ρ = Density of the particle

As the particle begins to sediment, the radial distance increases, which leads to an increase in velocity of the particle. This results in a frictional force F_f

$$F_f = -fu \qquad \text{Equation 3-19}$$

f = frictional coefficient which depends on the size and shape of the particle.

When a particle reaches steady velocity, the forces on the particle add to zero. Therefore, the summary of the above three forces is represented by:

$$F_s + F_b + F_f = 0 \qquad \text{Equation 3-20}$$

$$\Rightarrow \qquad m\omega^2 r - \frac{m}{\rho}\rho_0\omega^2 r - fu = 0 \qquad \text{Equation 3-21}$$

Rearranging all the terms

$$u = \frac{m\omega^2 r\left(1 - \frac{\rho_0}{\rho}\right)}{f} \qquad \text{Equation 3-22}$$

Sedimentation coefficient, s, is defined as

$$s = \frac{u}{\omega^2 r} \qquad \text{Equation 3-23}$$

The frictional coefficient f is related to the solvent viscosity η and the radius of the particle R as

$$f = 6\pi\eta R \qquad \text{Equation 3-24}$$

From equation 3-21, 3-23 and 3-24

$$s = \frac{m\left(1 - \frac{\rho_0}{\rho}\right)}{6\pi\eta R} \qquad \text{Equation 3-25}$$

The mass of the particle m can be given as

$$m = \rho V = \rho \frac{4}{3}\pi R^3 \qquad \text{Equation 3-26}$$

V= volume of a spherical particle

Substituting the value of m from Equation 3-26 into equation 3-25

$$s = \frac{4R^2(\rho - \rho_0)}{18\eta} = \frac{D^2(\rho - \rho_0)}{18\eta}$$

$$\Rightarrow \qquad D = \sqrt{\frac{18\eta s}{(\rho - \rho_0)}} \qquad \text{Equation 3-27}$$

D = the particle diameter = $2R$

The sedimentation coefficient is obtained directly from the AUC measurements and from the known values of density of particle, density of solvent and viscosity of solvent one can easily calculate the particle diameter.

4 Aims and Objectives

The goal of the present work is to explore the different aspects of templating techniques to obtain porous metal oxides and to study the effect of template on the intrinsic and morphological properties of the product materials. In addition to the templating approach, the possibility of modification of a parent system by conventional methods such as addition of a second metal oxide to alter the crystallization behavior and the surface properties is also investigated.

4.1 Concept.

In the present work two different types of templating approaches are studied. The first one is the transcriptive approach. Porous polystyrene beads for chromatographic purposes are used as templates for the synthesis of porous metal oxides. Many reports on the synthesis of porous polymer bead are available [79-82] and their widespread use has made it possible to get a large variety of commercially available products. These beads are designed to have open pore structure for achieving better flow properties. The porosity and surface functionalization can be selected according to the application. These features render porous polymer beads highly suitable for templating procedures. Recent reports have shown the successful use of macroporous polymeric beads as templates to obtain porous metal and metal oxide spheres [83, 84].

The synthetic strategy applied for the preparation of porous metal oxide spheres is shown in Fig. 4.1. The template beads are infiltrated with a liquid precursor to fill the pores. Then the precursor is transformed into a solid matrix by process such as sol-gel and

finally the template is removed by methods like calcinations, consolidating the inorganic matter to obtain the porous metal oxide beads.

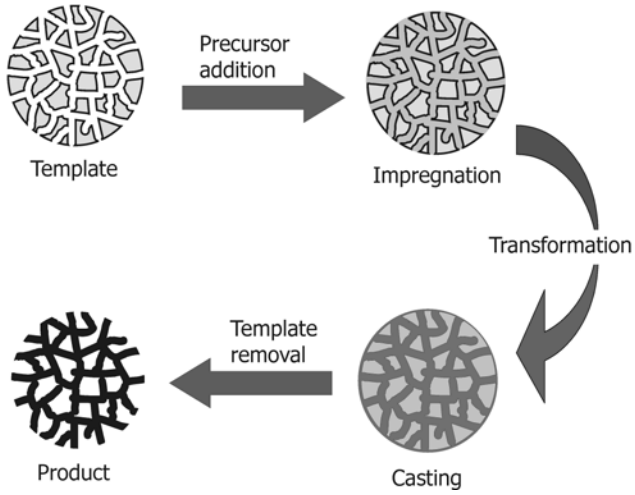

Figure 4.1. Schematic view of the porous polymeric beads templating process.

We use two types of precursors for the synthesis process. In the first project, metal alkoxides are used to synthesise the macroporous TiO_2-M_2O_3 spheres. The sol-gel process involving hydrolysis and condensation of the metal alkoxide was used to generate the metal oxide network. The second project involves the synthesis of the whole range of $Ce_xZr_{1-x}O_2$ and CuO-$Ce_xZr_{1-x}O_2$ nanoparticle sols and their use as nanoparticulate precursors for the fabrication of mesoporous materials.

The second templating approach follows a synergistic approach involving evaporation induced self-assembly of $Ce_xZr_{1-x}O_2$ nanoparticles and block co-polymer to generate large pore mesoporous structures as shown in Fig. 4.2. It is a common knowledge that amphiphilic block-co-polymers form micelles at low concentration in aqueous medium. The self-assembly process involves interaction of metal oxide nanoparticles and block-co-polymer micelles in aqueous/semi aqueous medium and assembly upon evaporation of

the solvent to generate periodic structures. On removal of the block-co-polymer by suitable method, stable ordered mesoporous material can be obtained.

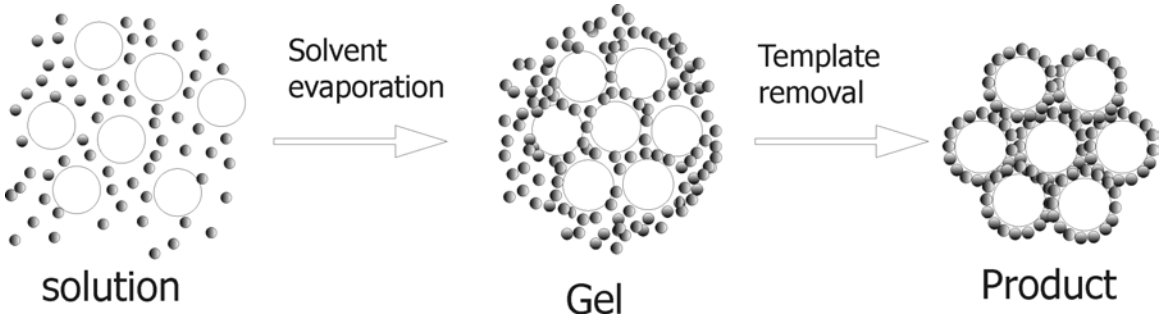

Figure 4.2. Schematic representation of evaporation induced self-assembly process of nanoparticle and block-copolymer micelles to generate porous material. Here ○: micelle and ●: metal oxide nanoparticle.

Very few reports are available in the literature depicting the use of nanoparticles and block-co-polymers to synthesise mesoporous materials [85, 86], as the synthetic approach is not easy to manifest. However, there are certain advantages of using this approach. The shrinkage in the final material is less as compared to the alkoxide process due to greater density of nanoparticles. If the nanoparticles used in the process are crystalline, higher calcination temperatures are not necessary for the crystallization process.

5 Results and Discussion

5.1 Synthesis of macroporous TiO_2-M_2O_3 spheres

Porous polystyrene beads, Source15 RPC (S15RPC) were used as a template in this study. As these beads are designed for chromatographic purposes, they possess open and well-connected internal pore structure, high effective surface area, spherical shape and diameter size in microns. To obtain the titanium dioxide and mixed oxide TiO_2-Al_2O_3, TiO_2-Ga_2O_3, TiO_2-In_2O_3 spheres sol-gel reactions, i.e., hydrolysis and condensation of the mixed alkoxide precursors, were conducted inside the matrix of the porous beads followed by removal of the template by calcination. The sample names were given according to the type and weight percent of the second metal oxide added to the TiO_2; for example, TiIn5 indicates 5 wt. % In_2O_3, 95 wt. % TiO_2. The ratio of template to precursor is very important as excess precursor results in the formation of additional inorganic matter and the aggregation of beads. However, the use of less than an optimum amount of precursor may result in poorly structured final product. A weight ratio of 1:1 dry bead to precursor solution was chosen as an optimum ratio. Containing 15 wt % gallium oxide (TiGa15)

Scanning electron microscopy (SEM) analysis (Fig. 5.1a and b) of the template show that the beads are fairly monodisperse, spherical in shape and highly porous. Fig. 5.1c and d depict the SEM images of the calcined samples containing 15 wt % gallium oxide (TiGa15). It showed that indeed a porous spherical morphology similar to that of the template beads, without excess inorganic material and negligible sphere aggregation, was

obtained, indicating that structural features from the initial beads (monodispersity, porous structure, and spherical shape) were maintained throughout the process.

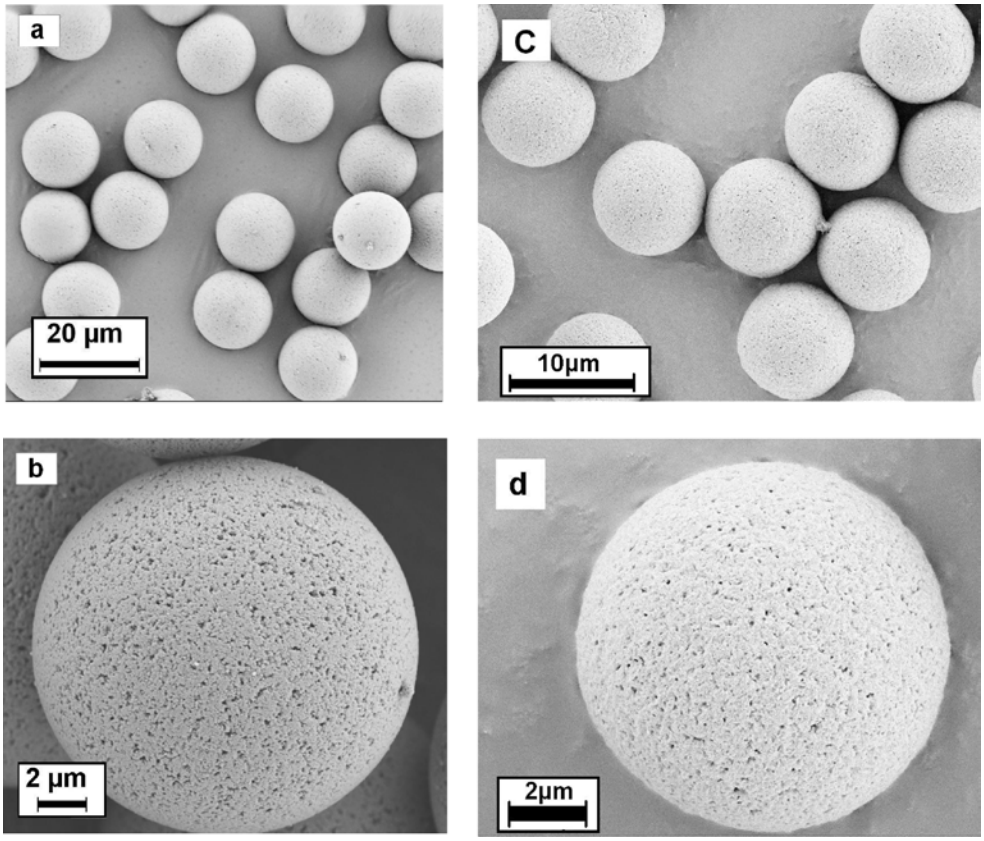

Figure 5.1 (a) and (b) SEM images of template beads- S15RPC, (c) the resulting inorganic spheres and (d) a higher magnification of a porous TiO_2-Ga_2O_3(TiGa15) sphere, showing porous surface structure.

However, there was considerable shrinkage after the calcination step. For the TiO_2 sample the average size of the spheres obtained was about 7 µm, i.e., diameter shrinkage of more than 50 % was observed. For the mixed oxides, the average sphere size increased with increasing weight of the second oxide (Table 5.1).

Sample	Inorganic Wt %	TiO_2 Wt%	BET Surface Area m^2g^{-1}	Average bead size µm	Average crystallite size* nm
Source15RPC	-	-	526	15	-
TO	0	100	61	7.1	16.2
TiIn5	5 (In_2O_3)	95	116	8.1	7.9
TiIn10	10(In_2O_3)	90	128	8.8	6.8
TiIn15	15(In_2O_3)	85	128	9.0	6.4
TiAl5	5 (Al_2O_3)	95	144	8.3	7.5
TiAl10	10(Al_2O_3)	90	168	8.7	7.3
TiAl15	15(Al_2O_3)	85	195	8.9	7.0
TiGa5	5(Ga_2O_3)	95	108	8.6	9.2
TiGa10	10(Ga_2O_3)	90	125	9.1	7.7
TiGa15	15(Ga_2O_3)	85	127	9.4	7.5

Table 5.1 Properties of the oxide spheres obtained upon calcination at 550ºC/10h. Inorganic content and TiO_2 content in weight percent from initial precursor composition, surface area obtained from Brunauer-Emmett-Teller analysis of nitrogen adsorption data, average crystallite size calculated from the 2 0 0 peak of anatase phase of corresponding sample using the Scherrer equation.

The details of the internal structure of the template beads and final inorganic spheres were observed by transmission electron microscopy (TEM). For TEM analysis the samples were embedded in polymer resin. Ultra-thin sections of the embedded sample allowed cross-sectional views of the beads. It was seen that the template beads (Fig. 5.2a)

have a random, interconnected internal pore structure with macropores in the range of 50-500 nm. Infiltration of the beads with precursor followed by hydrolysis and condensation reactions leads to an intermediate hybrid structure, an example of which is shown in Fig. 5.2b. Upon calcination, the organic material is burnt off and the amorphous inorganic network crystallizes, thus forming porous metal oxide spheres, Fig. 5.2c.

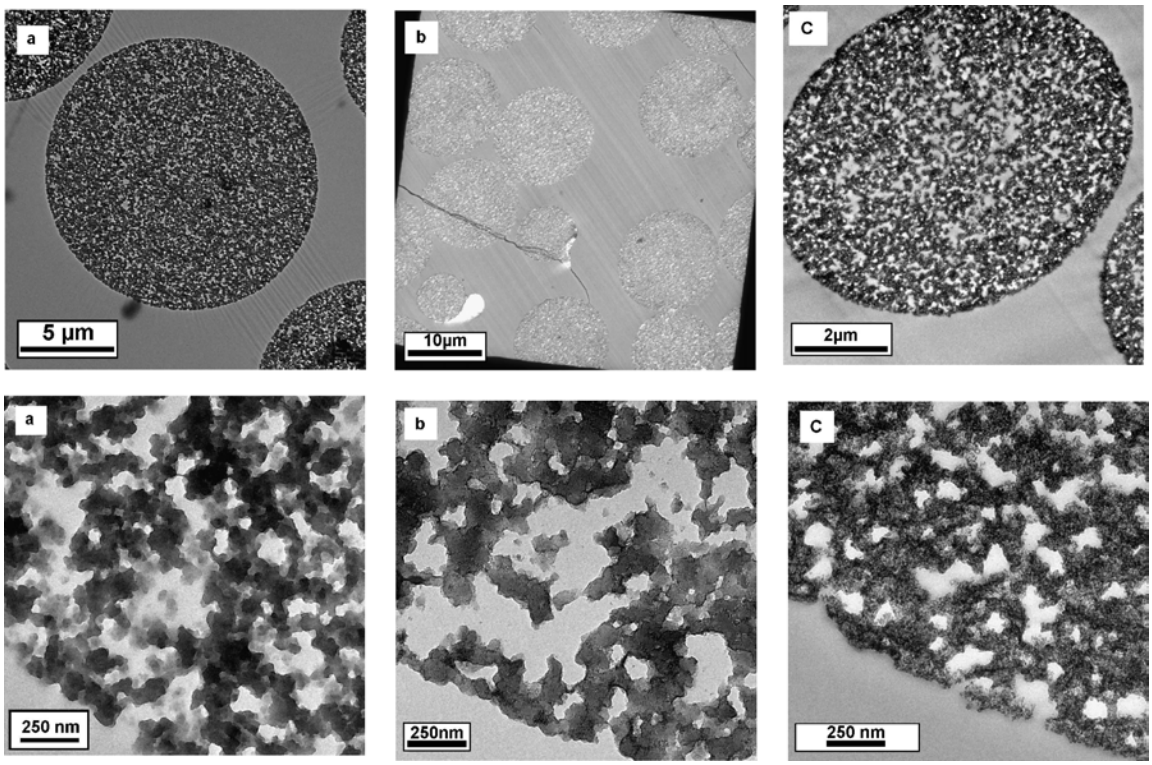

Figure 5.2 TEM images of ultramicrotomed samples at low and high magnification. (a) S15RPC template beads, (b) hybrid structure formed after hydrolysis and condensation of Ti/In isopropoxide mixed precursor inside the bead matrix, (c) TiO_2/In_2O_3 (TiIn10) spheres.

The effect of the addition of the second metal oxide on the titania particle size could be observed during the TEM studies: A decrease in particle size was seen in the mixed oxide samples compared with the TiO_2 sample. The average titania particle size decreased with

an increase in weight percent of the added oxide, which is in accordance with reports in the literature [47, 48, 87]. This effect was also reflected in the specific surface area of the final spheres. Table 1 gives the calculated BET specific surface areas of the template beads and porous inorganic spheres from nitrogen adsorption data. The surface area increased from 61 m^2g^{-1} for the TiO_2 spheres with increasing content of the second oxide: For the aluminum oxide samples this increase in surface area was maximum (195 m^2g^{-1} for 15 wt. % Al_2O_3, i.e., more than a three fold increase). For the addition of indium or gallium oxide to 15 wt. % the surface area was found to double.

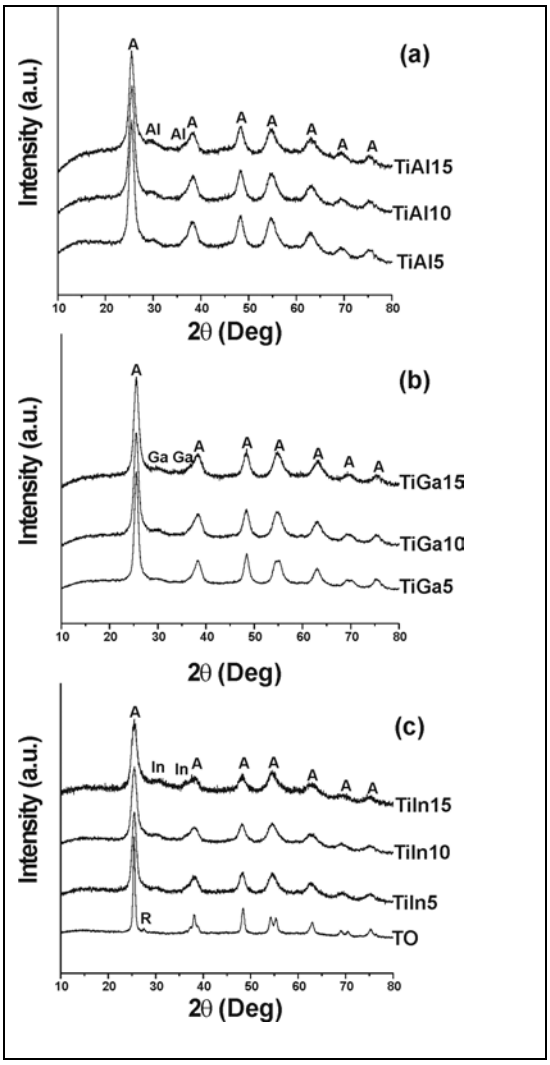

Figure 5.3 XRD patterns of the calcined (550ºC/10h) samples: (a) TiO_2 and TiO_2/In_2O_3 spheres, (b) TiO_2/Al_2O_3 spheres, (c) TiO_2/Ga_2O_3 spheres. Where A = anatase, R= rutile, In = In_2O_3, Al = Al_2O_3, Ga = Ga_2O_3.

X-ray powder diffraction (XRD) studies of the samples heated to 550 °C (Fig. 5.3) showed that the TiO_2 sample consisted mainly of the anatase phase with low intensity reflections corresponding to the rutile phase observed. The addition of the second oxide during synthesis resulted in peaks corresponding to only the anatase phase being observed for the titania in addition to broad reflections corresponding to poorly crystallized phases of the added oxides. As the peaks were very broad and of low intensity it was hard to predict the phases of the added oxides. No peaks of mixed phases, such as Al_2TiO_5, were detected. These results agree with those reported in the literature for TiO_2-Al_2O_3 and TiO_2-Ga_2O_3 systems wherein the anatase to rutile phase transformation occurs at temperatures higher than 900 ºC while Al_2O_3 and Ga_2O_3 remained amorphous at lower calcination temperatures [47, 87]. Furthermore, with an increase in the amount of the second metal oxide, an increase in the anatase peak width was observed, confirming the decrease in crystal size observed by TEM analysis. Crystallite sizes calculated using the Scherrer equation are given in Table 1. From the X-ray data the addition of Al_2O_3, Ga_2O_3 and In_2O_3 to titania retarded the phase transformation as well as the crystal growth of the titanium dioxide.

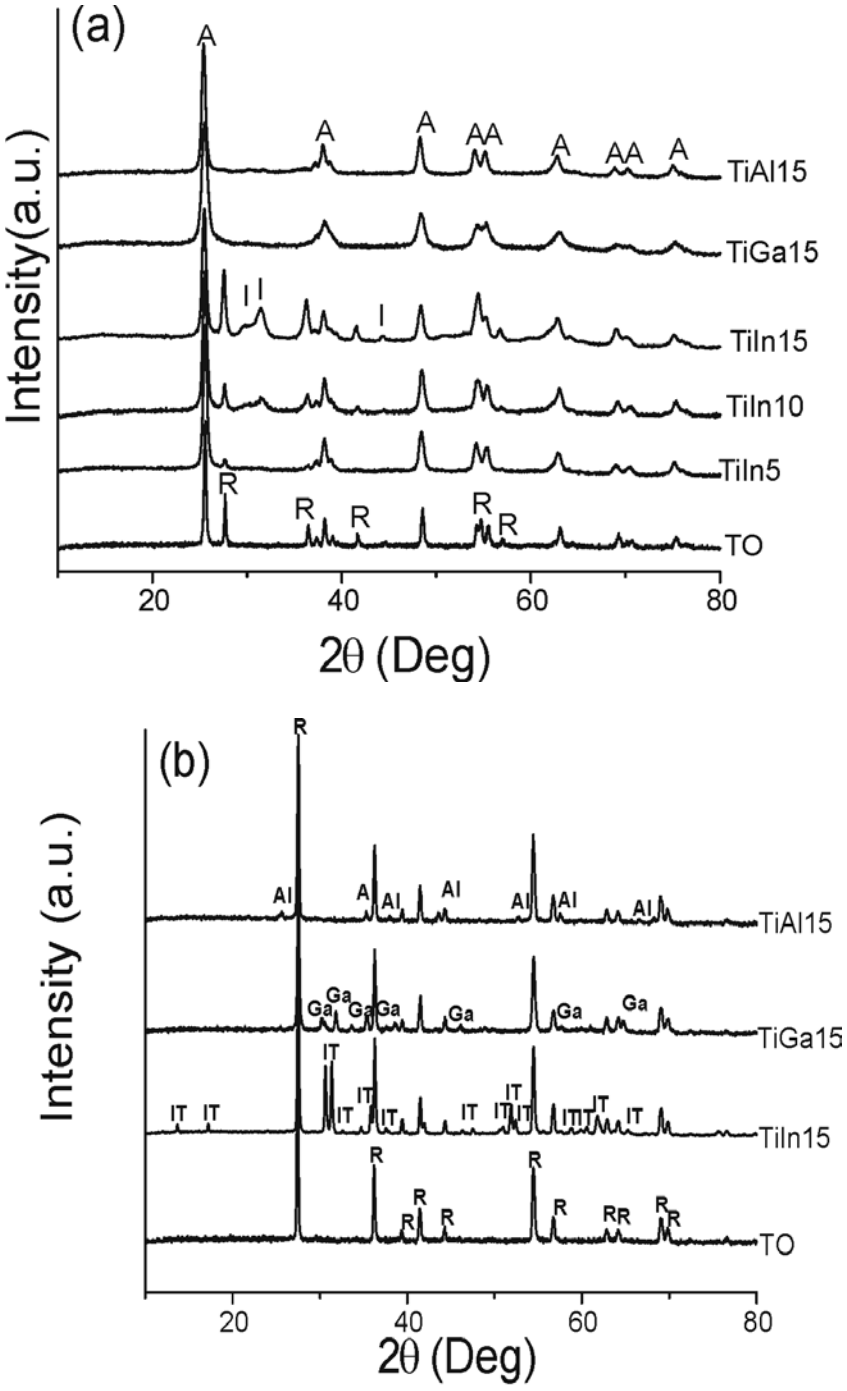

Figure 5.4 XRD patterns of samples calcined at (a) 750ºC/10h and (b) 950ºC/10h. Where A = anatase, R= rutile, In = cubic In_2O_3, Al = α–Al_2O_3, Ga = β–Ga_2O_3 and IT = In_2TiO_5.

The titania and titania-metal oxide samples were recalcined at higher temperatures (750 and 950 °C) to monitor phase transformation and crystallization of the second metal oxide, Fig. 5.4. After heating at 750 °C, the titania remained in the anatase phase in the presence of aluminum and gallium. However, in the presence of indium the rutile phase was observed. Low indium content showed less rutile content, but as the amount of indium increased the rutile content also increased. At lower indium content it may remain more dispersed, partially retarding the anatase to rutile transformation. But as the indium content increases, the indium oxide is more able to phase separate resulting in both an increase in In_2O_3 peaks and more rutile phase titania. An overall thinning of the anatase peaks is observed as the crystal size increases. Heating at 950 °C resulted in rutile phase peaks being observed for all the samples, plus metal oxide peaks for α-Al_2O_3 and β– Ga_2O_3 in case of TiO_2-Al_2O_3 and TiO_2-Ga_2O_3, respectively. For the TiO_2-In_2O_3 system, along with the rutile peaks, reflections matching with the reported pattern of In_2TiO_5 were observed [88]. Any further testing or analysis of the samples was conducted on materials heated to 550 °C only.

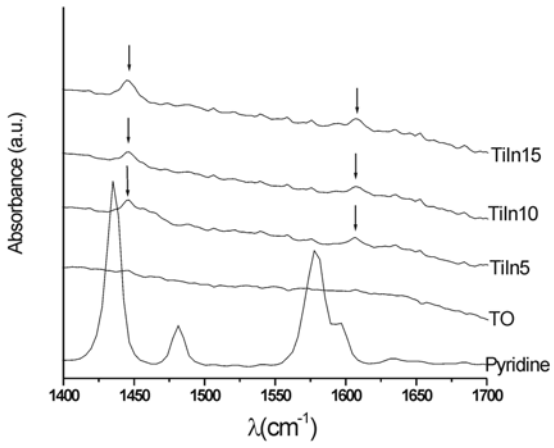

Figure 5.5 IR spectra of pyridine for calcined (550ºC/10h) TiO_2 and TiO_2-In_2O_3 samples treated with pyridine and degassed at 150 ºC for 90 min. The arrows indicate position of the bands corresponding to adsorbed pyridine.

Pyridine adsorption studies are useful to determine the surface acidity of samples [45, 89]. additionally allowing the distinction between Lewis and Bronsted acid sites. The formation of coordinated species, pyL, on Lewis acid sites leads to the appearance of IR bands near 1620-1600 cm^{-1} and 1450 cm^{-1}, whereas, the formation of pyridinium ions, pyH^+, on protonic sites gives rise to characteristic bands at 1640 and 1540 cm^{-1} [90, 91]. Fig. 5.5 shows representative IR spectra of the TiO_2 and TiO_2-In_2O_3 samples after treating them with pyridine and subsequently degassing at 150 ºC for 90 min. For the TiO_2 sample, bands corresponding to adsorbed pyridine were seen when the samples were degassed at room temperature (data not shown) after pyridine treatment. These bands disappeared upon degassing at 150 ºC, indicating the absence of strong acidic sites. However, the TiO_2-In_2O_3 samples even after degassing at 150 ºC, showed the absorption bands at 1444 cm^{-1} and 1604 cm^{-1}, corresponding to the presence of adsorbed pyridine. No other bands were observed, suggesting the presence of strongly acidic Lewis and not Bronsted acid sites. Similar results were obtained for the TiO_2-Al_2O_3 and TiO_2 -Ga_2O_3 samples. When considering the samples for photocatalysis these acidic sites may prove to be useful in co-ordination of organic species to the surface, thereby increasing the concentration of the organic compound at the catalyst surface. As the acidity is of Lewis type and not Bronsted, there is no influence of the addition of Al_2O_3, In_2O_3 or Ga_2O_3 on enhancing the concentration of surface hydroxyl groups.

5.2 Photocatalytic degradation of 2-chlorophenol

The degradation of 2-chlorophenol, a common organic pollutant, was chosen to assess the photocatalytic activity of the porous materials prepared. The photocatalytic experiments were carried out with the same initial 2-chlorophenol concentration (10^{-3} M), irradiation time (1.5 h), and temperature (20 ºC). The reproducibility of this data was good, with an error limit below 6 %. The titania spheres prepared by the templating method are photocatalytically active, however, the efficiency is lower compared with the Degussa P25 titania (see curves 1 and 4 in Fig. 5.6a). The activity of the TiO_2 beads decreased while increasing pH to neutral, then, going to alkali region, TiO_2 photactivity increased again (Fig. 5.6a).

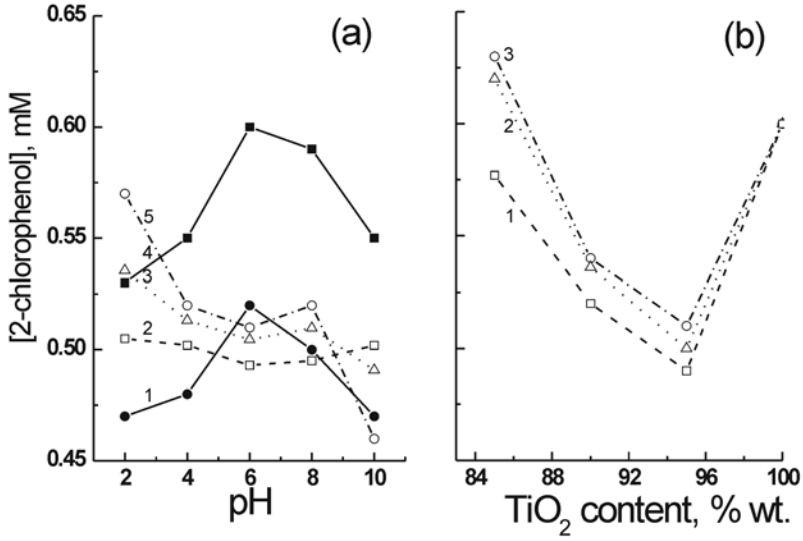

Figure 5.6 (a) Plot of 2-chlorophenol concentration remaining after UV irradiation as a function of pH for 1(●) Degussa P 25, 2(□) TiAl5, 3(Δ) TiGa5, 4(○) TiIn5, 5(■) TO. (b) 2-Chlorophenol concentration plotted against the TiO_2 wt % for 1(□) TiAl, 2(Δ) TiGa, 3(○) TiIn at a solution pH of 6.

Literature reports show contradicting data on pH dependence of pure TiO_2 photoactivity in 2-chlorophenol photodegradation reaction. Rao *et. al.*[92] and Oliveria *et. al.* [93] reported no significant pH dependence in the pH range of 3-11 and 3-9 respectively, while Doong *et. al.* [94] showed an increase in degradation rate with increase in pH (pH range 2.5-12.5). However, Ku *et. al*.[95] reported a decrease in degradation rate with increase in pH (pH range 3-11). No proper explanations for such discrepancy can be found in the literature: Various interdependent parameters, such as sample history, surface properties, experimental conditions, etc., which greatly influence materials properties and therefore effect the degradation behavior, making it difficult to find a consistent correlation. Addition of a second metal oxide component (Al_2O_3, Ga_2O_3, In_2O_3) lead to an enhancement of the photocatalytic activity (Fig. 5.6b). This was most pronounced for the TiO_2-metal oxide materials with 5 wt. % of the second oxide, which were seen to be more efficient than Degussa P25 at pH 6. However, increasing the second metal oxide content from 5 wt % to 15 wt. %, resulted in decreased photocatalytic activity within the respective series (Fig. 5.6b.). It has been shown previously that the addition of a small amount of a non-photoactive metal oxide can increase the photocatalytic efficiency of titania because of its influence on a number of materials properties (such as adsorption behavior, surface acidity, specific surface area, and crystallinity) [46, 60, 96, 97]. However, further increasing the content of the second metal oxide resulted in decreasing photocatalytic activity of the material.

Explanations for the observed increase in the photocatalytic activity of the titania after the addition of the second metal oxide are as follows: Firstly, as it was discussed above, the specific surface area of the material increased with the addition of the second metal oxide. Therefore, potentially, with more surface sites there is an increased probability of

organic moiety-catalyst surface interaction. Secondly, the second metal oxide stabilizes titanium dioxide against anatase to rutile phase transformation, hence increasing the amount of the more photoactive titania form, anatase [46, 60]. A third reason for the enhanced activity is the influence of the second metal oxide on the surface properties of TiO_2. It is well known that the activity of TiO_2 depends on the surface acidity and surface recombination rate [96, 97]. Modifying the TiO_2 with Al_2O_3, Ga_2O_3, or In_2O_3 makes the material more acidic, as shown by pyridine adsorption. As a result, improved adsorption of the decomposing substance on the surface of the mixed metal oxide materials, compared to the TiO_2, can be expected. It is also important to add that mixed TiO_2-metal oxide samples show a different pH-dependence of photoactivity than that of TiO_2 (Fig. 5.6a). The TiAl5 sample showed least variation in photocatalytic activity with change in pH. The TiIn5 sample showed greatest variation, being least active at low pH and most active at pH 10. The possible explanation for these results can be given as follows. XRD results for all the samples show absence of the second metal oxide even after extended calcination at 550ºC indicating that they remain amorphous. The reason for this might be that the second metal oxide remains dispersed, forming a layer on the anatase crystallite. This layer then dictates the surface properties and electron transfer from anatase crystal to the organic moiety. Increase in second metal oxide content increases the layer thickness, which can impede the process of electron transfer. Indeed we can see from Fig. 5.6b, that the photocatalytic activity decreases with increase in second metal oxide content. Al_2O_3 is a nonconducting material while In_2O_3 is a semiconductor. It is known for the semiconductor that the band position varies as a function of pH [98]. Assuming that the surface layer of the second metal oxide covers the anatase crystallites, we see that the Al_2O_3 containing samples show least variation in photoactivity as it is a non conductor

while In_2O_3 containing sample show maximum variation as their band gap varies most. Acidity increases as $In_2O_3 < Ga_2O_3 < Al_2O_3$. As discussed before, an increase in surface acidity enhances the adsorption behavior of the organic component and hence results in greater degradation of organics [96]. Accordingly, it is reasonable that the greatest activity was obtained for Al_2O_3 containing samples, followed by Ga_2O_3. In_2O_3 containing samples are the least active.

6 Results and Discussion

6.1 Synthesis of $Ce_xZr_{1-x}O_2$ nanoparticle sols

During the synthesis of the $Ce_xZr_{1-x}O_2$ sols the first step was the hydrolysis of the mixed precursor by addition of an aqueous NH_3 solution resulting in a pH higher than 10. It was necessary to wash off the excess of base immediately after the precipitation process. We observed that aging of the precipitate in basic medium, even for less than an hour, failed to give a transparent sol. The solubility product of $Ce(OH)_4$ is extraordinarily small ($2 \cdot 10^{-48}$) and the basic behaviour of $Ce(OH)_4$ leads to the situation that an increase of pH decreases the solubility of $Ce(OH)_4$, whereas a decrease of pH increases the solubility [99]. Accordingly, at basic pH the Ostwald ripening process enhances the growth of large particles, because precipitated $Ce(OH)_4$ clusters contribute to the crystal growth, whereas smaller grains dissolve slowly. After the washing step, nitric acid was added and the suspension was sonicated. The addition of acid leads to the opposite situation, namely a decrease of pH, so that smaller hydroxide particles dissolve fast and that the larger ones grow slowly because of the low $Ce(OH)_4$ concentration. Sonication enhanced this process and prevented the growth of particles beyond a certain extent by breaking up the larger agglomerates. The particle surface is covered with hydroxyl groups. Since the pH of the sol was below 2, the hydroxyls are protonated, leading to positively charged particles. The positive charge is counterbalanced by nitrate anions forming an electrical double layer-Stern layer [100, 101], followed by diffused layers. This imparts stability to the nanoparticles in the sol. The sols do not undergo gelation or sedimentation for at least 12

weeks. Upon dialyzing the sol to a pH of 4-5, it started to gel slowly over a period of 1-2 days. Depending on the composition the colour of sols varied from yellow for pure CeO_2 to colourless for pure ZrO_2. The solid content in the sols was about 5-8 wt%. Undialyzed sols were found to be stable on the addition of a large quantity of alcohol. The sols that were dialyzed against ethanol showed that about 90 % of water could be replaced by ethanol. However, total water replacement was not possible and resulted in precipitation of nanoparticles.

For many applications of nanoparticles, particle size distribution is a fundamental parameter, but still its determination often remains a difficult task. Although literature reports generally present particle size distribution data based on TEM results [102, 103], there is no unambiguous statistics for the particle size distribution of the whole sample. Analytical ultracentrifugation (AUC) has proven to be a versatile tool for the measurement of the particle size distribution of colloidal samples [78, 104]. In contrast to TEM, AUC detects all particles even down to smallest sizes. The resolution of the particle size distribution for small nanoparticles lies in the Angström range [105].

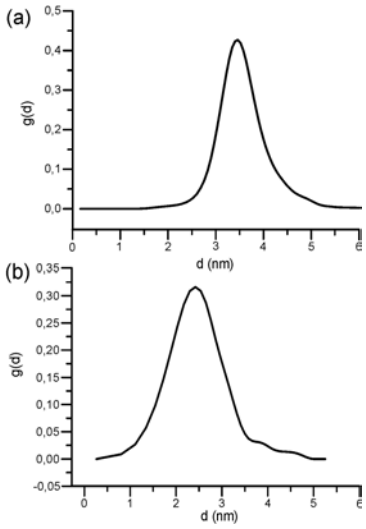

Figure 6.1 Particle size distribution curves for dialyzed CeO_2 and ZrO_2 sol obtained by AUC analysis.

The AUC experiments were performed at 40000 and 60000 rpm for dialyzed CeO_2 and ZrO_2 sols, respectively, using a laser of wavelength 675 nm and interference optics. Fig. 6.1 shows the particle size distribution for pure CeO_2 (a) and ZrO_2 sols (b). For both samples the particle size distribution is very narrow. For CeO_2 the average particle diameter was 3.45 nm and for ZrO_2 2.42 nm. No other signals were obtained at slower rotation speeds indicating that the particles were non-aggregated.

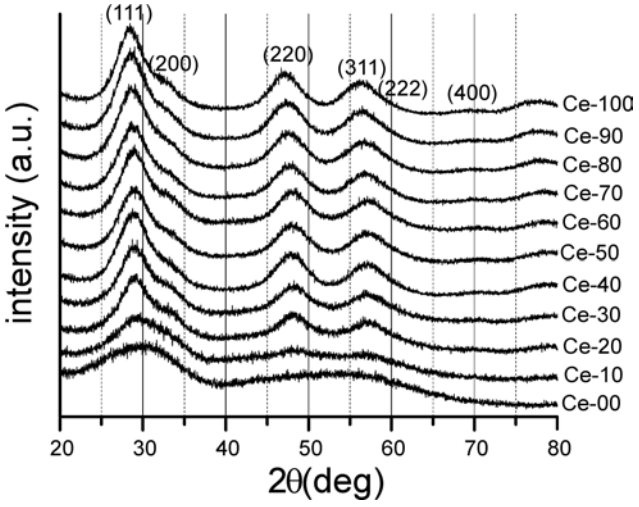

Figure 6.2 XRD patterns of gels obtained from the dialyzed sols.

X-ray powder diffraction patterns of dried gels are shown in Fig. 6.2. The patterns are named according to the CeO_2 content of the sample, i.e., Ce-100 contains 100 mol % Ce. All the samples, except the pure ZrO_2 (Ce-00) and the 10 mol% CeO_2 (Ce-10), show broad reflections corresponding to the cubic fluorite type phase. The Ce-00 sample displays only two humps indicating that the sample is X-ray amorphous. Although the Ce-10 sample shows weak reflections of the cubic fluorite structure, there is still a strong amorphous background. According to the Scherrer equation, the average particle size calculated from the (220) reflection is 2.45 nm for Ce-100, and with increasing zirconia content, the crystallite sizes become smaller. Fig. 6.3 displays the experimental XRD powder pattern of the Ce-100 sample (Fig. 6.3, full line) together with the diffraction

pattern calculated by the Debye equation of kinematic diffraction for spherical, monodisperse particles of 2.5 nm in diameter with the cubic fluorite structure (Fig. 6.3, dotted line)[106, 107]. The calculated and the experimental patterns match well. Assuming that all the particles are monocrystalline, the discrepancy in average particle diameter obtained from AUC analysis and from XRD data may be due to the difference in diameter of the dried particles and the particles in solution. As discussed before, in the stabilized sols the particles possess a layer of tightly bound ionic double layer (Stern layer) followed by solvent molecules depleted ionic layer, which makes the radius larger in the AUC analysis than the actual particle size [108].

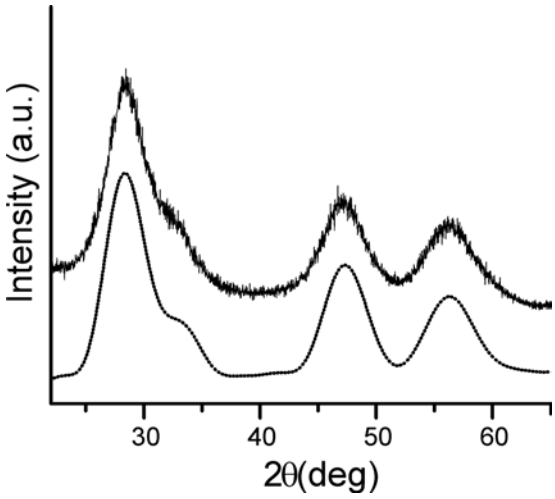

Figure 6.3 Calculated diffraction patterns for spherical, monodisperse CeO_2 cubic nanoparticles with diameter of 2.5 nm (dotted line) and experimental pattern (full line) of CeO_2 nanoparticles.

The phase diagram for the CeO_2-ZrO_2 system reported in literature depicts three major phases, i.e., cubic, tetragonal and monoclinic. The tetragonal phase is further divided into stable *t* and metastable *t*' and *t*'' structures [57, 109, 110]. In case of the formation of solid solution between CeO_2 and ZrO_2, the smaller Zr^{4+}(ionic radius = 0.84 Å) occupies the position of the larger Ce^{4+}(ionic radius = 0.97Å). According to Vegard's rule, a decrease in cell volume is expected for both the cubic and the tetragonal phases with an increase in the ZrO_2 content. Even though XRD is not sensitive enough to distinguish between the

cubic *t*' and *t*'' phases, especially for smaller crystallites, the correlation between the *d* values for the (111) reflection in dependence of the CeO_2 content gives hint about phase changes [111](Fig.6.4). The decrease in *d* values with the decrease in CeO_2 mol% confirms the formation of a solid solution in the system. In addition, there is a linear decrease of the *d* values from Ce-100 to Ce-60 representing the cubic phase structure. From Ce-50 to Ce-20 the *d* values change only slightly. This composition range corresponds to the cubic, *t*' and *t*'' mixed phase region as discussed by Vlaic *et. al.* [111] The lattice parameter calculated from the (111) reflection of the pure CeO_2 sample is a = 5.416Å, which matches well with the lattice parameter of bulk CeO_2 oxide (a = 5.41134)[112]. It was reported for CeO_2 nanoparticles, that due to the presence of oxygen deficiency and lattice defects the lattice parameter increases with decreasing particle size [113, 114]. However, in spite of the small particle size of 2.5 nm in this case there is no difference of the lattice parameters between the nanoparticulate and the bulk phase, leading to the conclusion that the particles obtained are stoichiometric and nearly free of lattice defects.

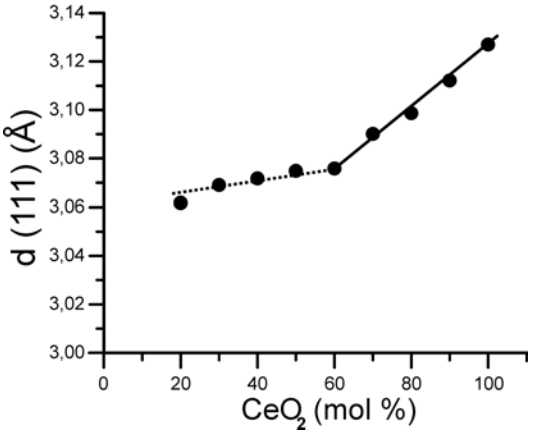

Figure 6.4 Variation of *d* value of (111) reflection with CeO_2 content.

Fig. 6.5a shows HRTEM pattern of an assembly of CeO_2 nanocrystals exhibiting an average particle size of 2-3 nm. This agrees well with the experimental and calculated XRD powder pattern (cf. Fig. 6.3). The lack of any surface protection layers results in

some agglomeration of the particles. According to the randomly oriented lattice fringes, the particles are not coalesced. In Fig. 6.5b selected area electron diffraction (SAED) is presented. The lattice distances measured from the diffraction rings are in perfect agreement with the cubic fluorite structure of CeO_2. Fig. 6.5c shows the HRTEM pattern of a 2.5 nm isolated particle oriented along the [110] direction. The Power Spectrum (PS) i.e., the square of the Fourier transform of the TEM image) of this particle is displayed in Fig. 6.5d giving evidence that the particles are well crystallized in the cubic fluorite structure without the presence of defaults.

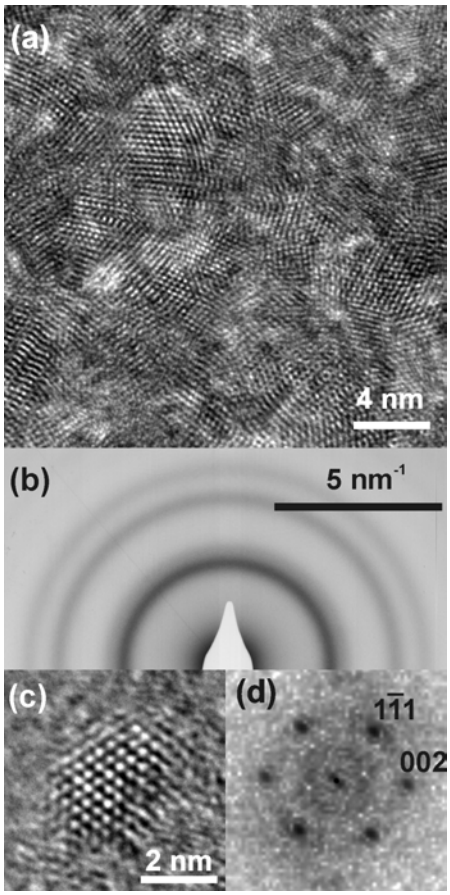

Figure 6.5 HRTEM image of an assembly of CeO_2 nanoparticles (a), SAED (b), HRTEM of an isolated particle (c) and respective PS (d).

Fig. 6.6a shows a HRTEM image of an assembly of $Ce_{0.5}Zr_{0.5}O_2$ nanoparticles with diameters of 2-3 nm. As for the pure CeO_2 nanocrystals the particles are packed together but are not coalesced. The SAED pattern of such a spherical assembly (Fig. 6.6b) shows

broad rings that match with the $Ce_{0.5}Zr_{0.5}O_2$ structure. The HRTEM pattern of an isolated 2 nm particle proves the high crystallinity (Fig. 6.6c). This is further confirmed by the PS of this particle (Fig. 6.6d), which is characteristic for the $Ce_{0.5}Zr_{0.5}O_2$ structure without structural defaults. The particle is aligned along the [110] direction.

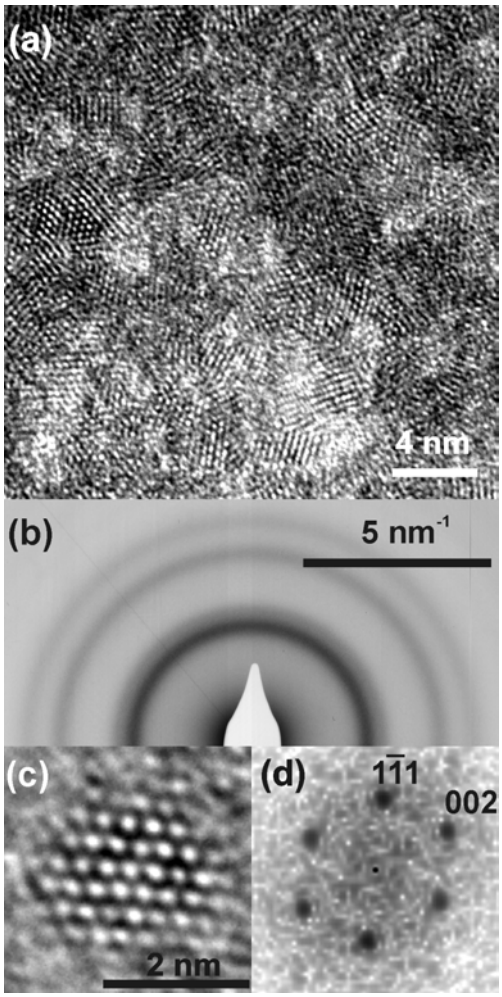

Figure 6.6 HRTEM image of an assembly of $Ce_{0.5}Zr_{0.5}O_2$ nanoparticles (a), SAED (b), HRTEM of an isolated particle (c) and respective PS (d).

XRD, TEM and HRTEM studies performed on the ZrO_2 particles show that they are smaller than 2 nm and mainly amorphous in nature. Raman spectroscopy was used to probe the local structure. Fig 6.7 depicts Raman spectra of all the samples. For Ce-00 (pure ZrO_2) two broad bands are observed at around 550 and 400 cm^{-1}. These two positions do not match with any of the standard Raman shifts reported for monoclinic, tetragonal or cubic ZrO_2 structures. However, quite similar types of Raman spectra have

previously been reported for pure zirconia gels prepared from zirconyl chloride [115]. The bands were attributed to polymeric Zr-O-Zr bonds in amorphous $ZrO_2.nH_2O$. Addition of 10 mol% CeO_2 in the Ce-10 sample induces a slight increase in particle size. Even though the Ce-10 sample shows weak reflections in the XRD, according to the Raman spectrum the local structure remains mainly disordered. A broad peak appears around 470 cm^{-1} in the Ce-20 sample. With increase in CeO_2 content, the intensity of this reflection is increasing, while the peaks around 550 and 400 cm^{-1} start to disappear. For higher CeO_2 containing samples (Ce-60 to Ce-100) a single broad peak is observed, which can be attributed to the F_2g mode of the cubic fluorite structure. The continuous shift in the peak position towards lower wavelength values with increase in CeO_2 content is in agreement with the increase in lattice parameter observed by XRD. For cubic CeO_2 bulk material a single symmetrical peak around 465 cm^{-1} is reported in the literature [109, 116]. Since the lattice parameter measured by XRD matches with that of bulk material, a corresponding symmetrical Raman peak is expected. However, in the case of the pure CeO_2 sample (Ce-100), an asymmetrical peak is found at 452 cm^{-1} instead of at 465 cm^{-1}. A possible explanation is the occurrence of a phonon confinement effect, frequently observed for nanocrystalline material [117]. The asymmetry, shift or even appearance of new bands is explained by a relaxation of the **q**=0 selection rule. This relaxation makes it possible to detect phonons from areas others than the centre of the Brillouin zone. Another possible explanation lies in the fact that XRD essentially give information on the periodicity of a material, while Raman depicts the vibrational behavior. The atoms on the surface are coordinatively unsaturated and hence show lower vibrational absorption than bulk material. In case of nanoparticles with sizes as small as 2.5 nm, the number of atoms at the surface is significantly higher than inside the particle, resulting in a shift in the peak

position. The asymmetry arises from the difference in absorption frequencies of atoms inside and on the surface of the particle.

In addition, in all the samples peaks at 1050 cm^{-1} and 700-750 cm^{-1} are observed which are attributed to surface bound nitrate groups [118]. Interestingly, for the samples Ce-100 to Ce-70 a small sharp peak around 1000cm^{-1} appears, which has not been reported previously. Generally, group V oxides exhibit such a peak corresponding to terminal metal-oxygen double bonds (M=O) [119]. These samples also show a weak shoulder around 600 cm^{-1}, which can be attributed to the presence of oxygen vacancies or lattice defects. However, the intensity of this shoulder is very low indicating that there are almost no lattice defects present in the nanoparticles.

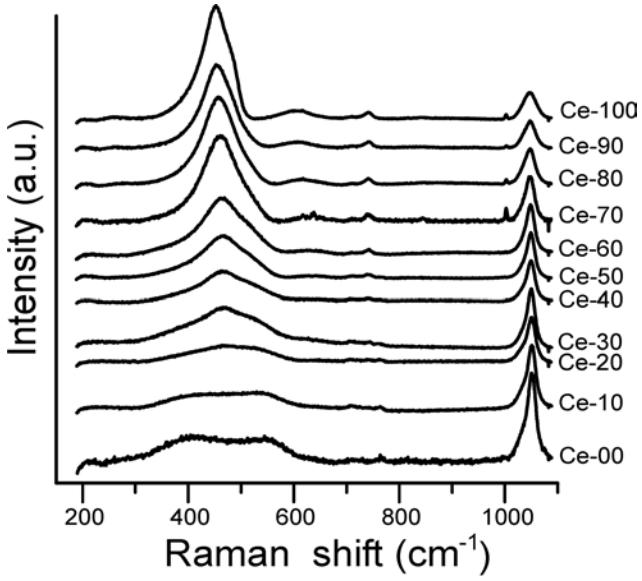

Figure 6.7 Raman spectra of the gels obtained from the dialyzed sols.

For the cubic structure a single peak corresponding to the F_2g mode is expected, while for the tetragonal structure six peaks related to 1 A_1g, 3 Eg and 2 B_1g modes are expected. The Raman spectra of the Ce-50 to Ce-00 samples give no indication for the presence of the tetragonal structure. However, the broadness of the peaks as well as the absence of

reflections due to the restrictions induced by particle size confinement prevents a complete assignment of the structure of the Ce50 to Ce-00 samples at this point.

6.2 Synthesis of $(Ce_xZr_{1-x}O_2)_a$ $(CuO)_b$ nanoparticle sols

The synthesis of $(Ce_xZr_{1-x}O_2)_a$ $(CuO)_b$ was done for the preparation of mesoporous spheres for the catalytic studies. The composition chosen for this purpose was $(Ce_{0.5}Zr_{0.5}O_2)_{0.75}$ $(CuO)_{0.25}$. The synthesis procedure was modified. Instead of $ZrOCl_2$, $ZrO(NO_3)_2.xH_2O$ was used to avoid contamination with chloride ions. The appropriate amounts of corresponding salts for Zr, Ce and Cu were dissolved together in water. Instead of aqueous NH_3, NaOH solution was used for the hydrolysis, because Cu ions form a soluble complex with ammonia. The rest of the procedure was the same as in the case of the $Ce_xZr_{1-x}O_2$ sols. During the washing, the supernatant remained colourless indicating that copper was not washed out during the process. The resultant sol had a green colour. However, upon dialysis the green colour changed to yellow indicating that the copper was washed off from the sol. The possibility of presence of separate Cu based particles, which are removed from the sol on dialysis because of the extremely small size, was ruled out from AUC studies of this sol. AUC analysis showed a single peak similar to that of pure CeO_2. XRD pattern of the dried sol matched completely with that of $Ce_{0.5}Zr_{0.5}O_2$ and showed no additional reflections. From all these results it can be concluded that the copper is not incorporated in the nanoparticles themselves. It probably exists in a soluble form, which remains amorphous upon removal of the solvent.

7 Results and Discussion

7.1 Synthesis of mesoporous $Ce_xZr_{1-x}O_2$ spheres

In the synthesis of porous $Ce_xZr_{1-x}O_2$ and $Ce_xZr_{1-x}O_2$-CuO porous spheres a variety of polymer beads with different pores sizes and surface functionality were tried as templates. Of all the products tried, XAD-16™ polystyrene beads gave the best results. These beads are mesoporous, non-functionalized polystyrene beads with high specific surface area. During the synthesis, the cleaned beads were soaked in the non-dialyzed aqueous sol and the water was allowed to evaporate gradually by heating at 60 ºC for two days. The removal of solvent leads to the deposition of sol within the pores of the beads. The dry beads were then washed to remove excess of material from the bead surface and to separate the agglomerated beads. It was observed that the washing of the beads dried only at 60 ºC resulted in washing off of the nanoparticles and consequently in poorly structured oxide spheres. An additional heating at 100 ºC was necessary prior to the washing stage to ensure compaction of the nanoparticle network within the pores. After washing, the beads were again dried at 60 ºC for two days. The optimum ratio of template beads and aqueous sol to obtain well structured beads was found to be 0.005 mole metal oxide (MO) to 1.5 g beads from systematic variation of both quantities. In the calcination process nitrogen atmosphere was maintained during the ramp period and 1.5h after reaching the calcination temperature. The calcination was carried further in flowing air. The main purpose behind such a calcination program was that the template is carbonized in nitrogen atmosphere thus retaining its form so that the connectivity of nanoparticle and

their growth is restricted to the pore space. The carbonized template can be removed afterwards by switching the gases. The calcined beads were spherical in shape and their colours varied according to the composition from white with bluish tinge for pure ZrO_2 to dark yellow for pure CeO_2 and grayish green for ($Ce_{0.5}Zr_{0.5}O_2$) 75 mol%-CuO 25mol %.

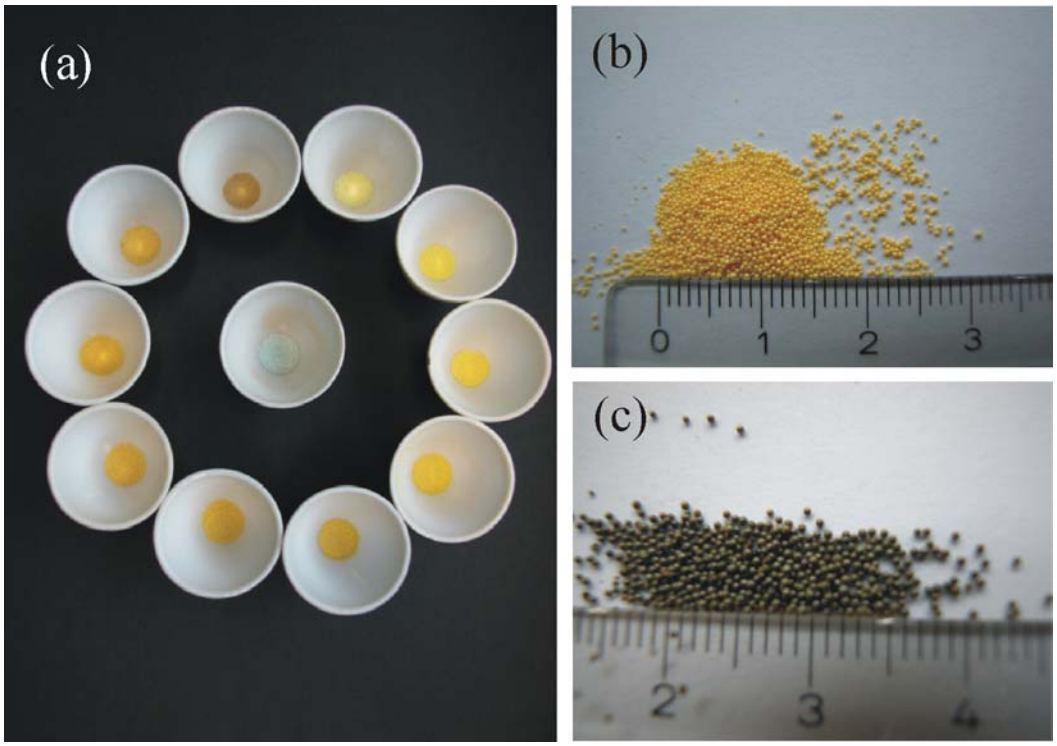

Figure 7.1 (a) The whole range of $Ce_xZ_{1-x}O_2$ sphere obtained upon calcination at 500 ºC (b) CeO_2 spheres (c) $(Ce_{0.5}Zr_{0.5}O_2)_{0.75}(CuO)_{0.25}$ spheres.

Optical photographs of the calcined beads (Fig. 7.1) show that the beads were non-agglomerated and mostly smaller than 1mm in size. A closer look at the external and internal morphology was obtained from SEM studies. Fig. 7.2 (a) and (c) show the SEM images of the XAD-16 template beads. The calcined CeO_2 spheres are displayed in Fig. 7.2 (b) and (d). The template beads are not monodisperse and their size varies greatly from about 200 µm to 1 mm. Hence the extent of shrinkage upon calcination cannot be

estimated. However, similar size ranges were seen for the calcined spheres. It can be seen that the calcined spheres were spherical in shape with a smooth external surface indicating absence of extra matter.

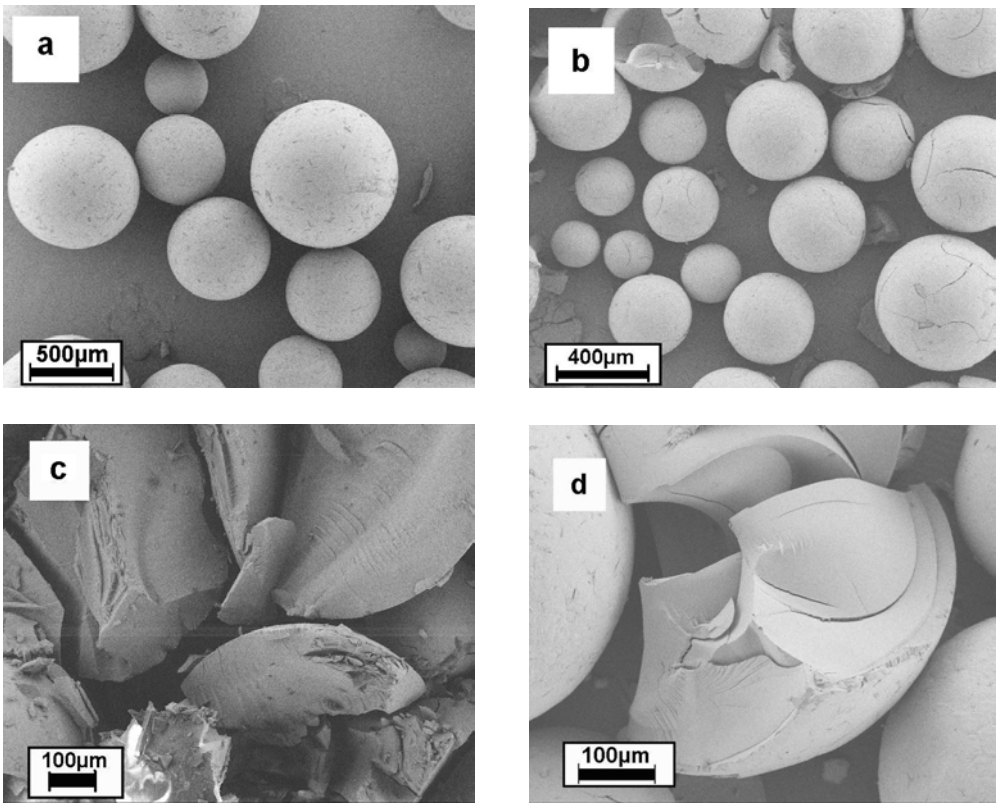

Figure 7.2 SEM images of (a) template beads XAD-16 external morphology, (c) internal morphology; and (b) calcined spheres of CeO_2 external morphology, (d) internal morphology.

Larger spheres showed occasional cracks, which might arise from the heat treatment. Apart from the cracks, the spheres had fare mechanical stability and it was necessary to break them by applying force to see the internal structure. The broken CeO_2 spheres show that the internal part of the spheres has a uniform morphology and no uneven shrinkage or deformation is observed. As the average pore sizes in the template (10-20 nm) and

consequently in resultant oxides spheres is quite small, it is not possible to see any porous structure from SEM studies. For this reason, TEM analysis of the template beads as well as the resultant oxide spheres was carried out.

Fig. 7.3 shows some TEM images of cross section through the template beads and oxide spheres The pore structure of the template beads is disordered with pores in the range of 10-20 nm with occasional appearance of larger pores of size 50- 100 nm. From the TEM images of the oxide spheres and their comparison with that of the template beads indicates that the pore structure of the oxide sphere does not exactly resemble the pore

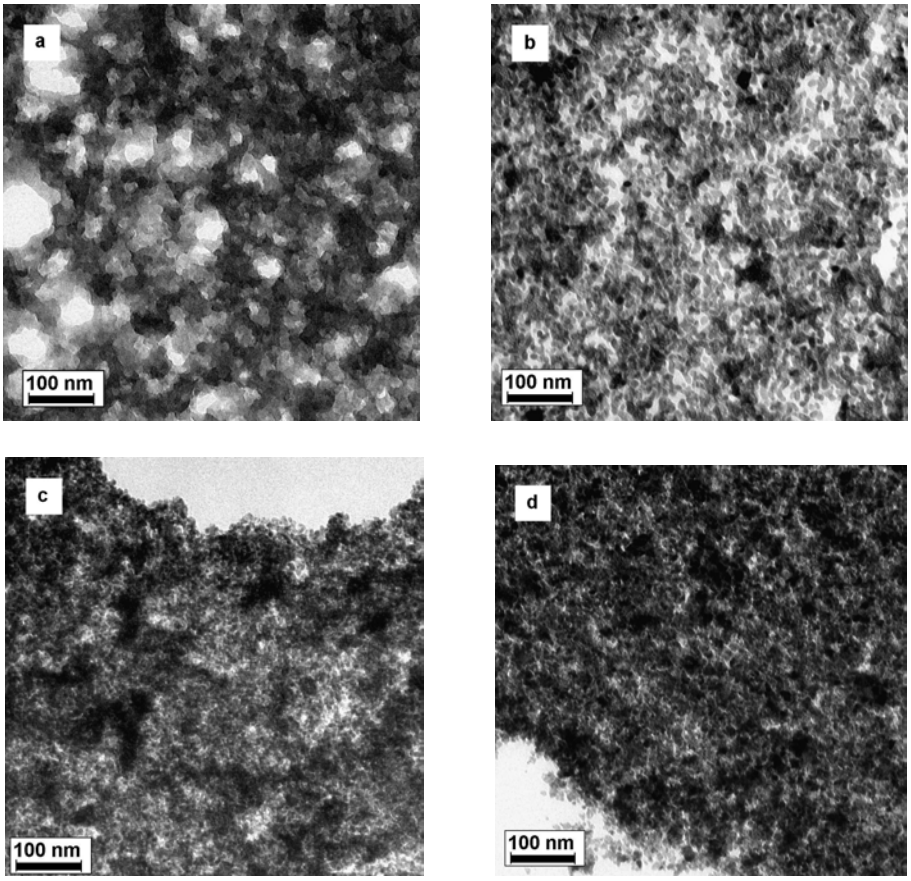

Figure 7.3 TEM images of ultramicrotomed samples: (a) template bead XAD-16, (b) ZrO_2 sphere, (c) $Ce_{0.5}Zr_{0.5}O_2$ sphere, (d) CeO_2 sphere. All the oxide samples were calcined at 500 ºC/ 8h in air.

structure of the template. This can be explained on the basis of the size of the nanoparticles and the pore size. The CeO_2 nanoparticles have an average diameter of about 2.5 nm, while the pore size of the template as well as the pore wall thickness is in the range of 10- 20 nm. So it is obvious that upon calcination at 500 ºC for 8h after template removal the particle tend to sinter, causing particle growth and shrinkage of the structure. For macroporous systems the pore sizes are very large as compared to the particle size. Hence these effects are not pronounced, but in the present system the pore size and the particle sizes are in comparable range. However it can be seen that the calcined product retains the high porosity. For the pure ZrO_2 spheres the pores are larger and the pore structure resembles more that of the template, while for CeO_2 spheres the pores are smaller. In general, the pore size is seen to reduce in the order of ZrO_2, $Ce_{0.5}Zr_{0.5}O_2$ and CeO_2.

Additional information on the surface properties of the calcined oxide spheres was obtained by nitrogen sorption studies (Fig.7.4).

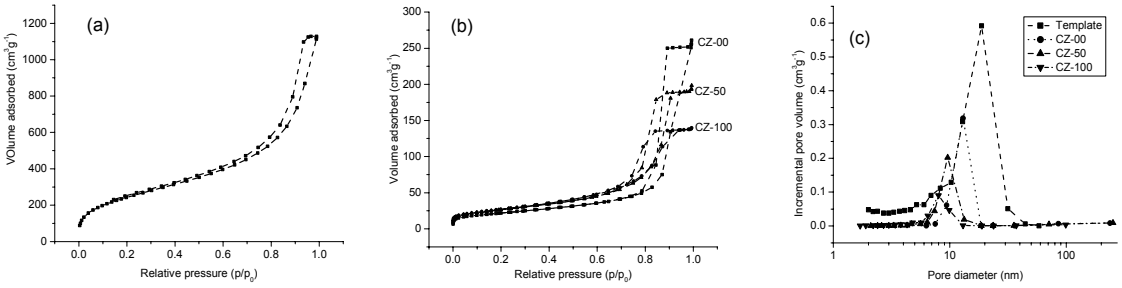

Figure 7.4 Nitrogen sorption isotherm of (a) template, (b) $Ce_xZ_{1-x}O_2$ sphere obtained upon calcination at 500 ºC/ 8h, (c) BJH pore size distribution obtained from the desorption branch of isotherms.

Here the samples calcined at 500 ºC / 8h are labeled according to the CeO_2 mole percent in the sample. For example, CZ-100 contains 100 mol% CeO_2, CZ-50 contains 50 mol% CeO_2 and CZ-00 contains 0 mol% CeO_2 (i. e., 100 mol % ZrO_2). Nitrogen sorption isotherm of the template and the calcined product show a type IV isotherm characterized by the presence of hysteresis. This indicates that the template beads as well as the samples calcined at 500 ºC are mesoporous. BJH pore size distributions indicate that the template has average pores of around 20 nm, while the final oxide spheres are in the range of 5-15 nm. The average pore diameter decreases from CZ-00 to CZ-100, which is also evident from the TEM images of these samples.

The effect of calcination on the crystal structure was studied by powder X-ray diffraction (XRD). Fig. 7.5 shows the XRD patterns of spheres calcined at 500 ºC and 900 ºC. The samples calcined at 500 ºC are named as mentioned above. The samples calcined at 900 ºC are named in a similar fashion by replacing CZ by XCZ.

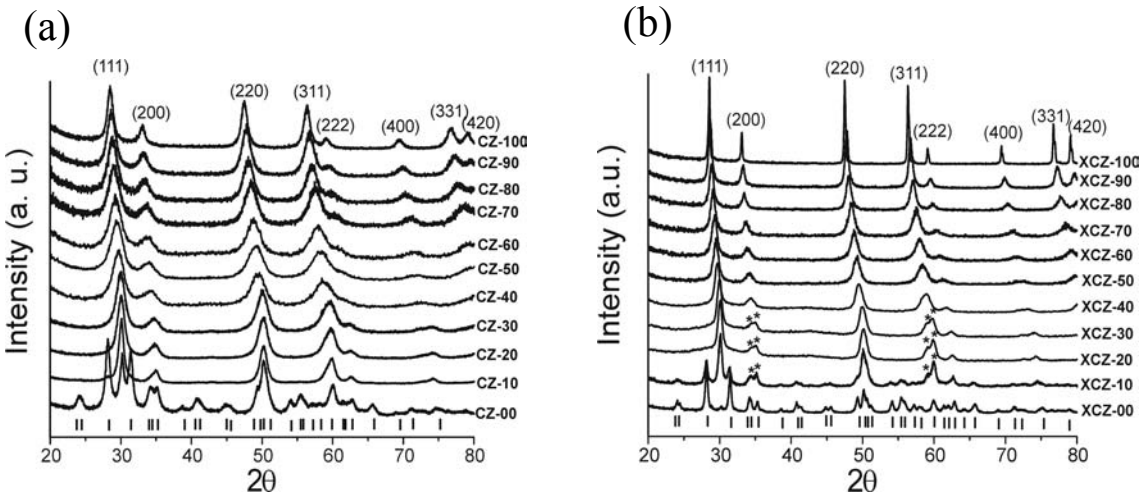

Figure 7.5 Powder X-ray diffraction patterns of $Ce_xZr_{1-x}O_2$ spheres calcined at (a) 500 ºC / 8h, (b) 900 ºC / 2h. Where **I**: reflections corresponding to monoclinic ZrO_2 and ∗: splitting reflections due to occurrence of the tetragonal phase.

As seen in the previous chapter all the nanoparticle sols except for pure ZrO_2 and 10 mol% CeO_2 samples were crystalline. Calcination at 500 ºC brings about the crystallization of these samples. Overall increase in the crystallite size is also observed, which is reflected in sharpening of the reflections. The reduction in the lattice parameter upon increase in ZrO_2 mole % is clearly evident from the shift of reflections to higher angles. The samples CZ-100 to CZ-50 have XRD patterns matching with the cubic fluorite type structure. However, from CZ-50 to CZ-10, the (200) and (311) reflections show asymmetric character due to tetragonal phase formation. The stable tetragonal polymorph is identified from the cubic structure by a splitting of the (200) reflection into (002) and (200) reflections. Similarly (311) and some other higher order reflections also show such characteristic splitting [111, 120]. However, the nature of such tetragonality, i.e., if it is the stable tetragonal phase *t* or if it is one of the metastable tetragonal phases *t' or t''* is not evident from the XRD pattern. The CZ-00 (pure ZrO_2) sample shows a mixture of monoclinic [121] and tetragonal phases. The phase evolution was more evident from the XRD patterns of the samples calcined at 900 ºC. The XCZ-00 (pure ZrO_2) sample shows a pattern corresponding to monoclinic ZrO_2, while a small reflection due to tetragonal phase can be still seen indicating that the tetragonal-monoclinic transformation is still not complete. The heat treatment results in phase separation for the XCZ-10 (10 mol% CeO_2) into the monoclinic and tetragonal phase. This indicates that the addition of 10 mol% CeO_2 is not sufficient to stabilize ZrO_2 in the tetragonal phase. The XCZ-20 and the XCZ-30 samples show splitting of the (200) and (311) reflections, signifying a stable tetragonal phase in these two samples. The XCZ-40 showed some asymmetry for the

above-mentioned reflections, while samples with higher CeO_2 content (XCZ-50 to XCZ-100) showed symmetric reflection matching with the cubic pattern. More information on the phase composition of the samples calcined at 900 ºC was obtained from Raman scattering studies. The Raman spectrum of XCZ-00 (pure ZrO_2) shows a number of bands that match well with the reported spectrum of monoclinic ZrO_2 [120]. However, the XCZ-10 sample, which is a mixture of monoclinic and tetragonal phases, showed no Raman bands corresponding to tetragonal ZrO_2 except for a shift in the position of the Raman bands. For the sample XCZ-20 five bands at 261, 315, 458, 598 and 628 cm^{-1} were observed, which correspond to the tetragonal structure [120]. With the increase in ZrO_2 content the bands shift towards higher frequency indicating a change

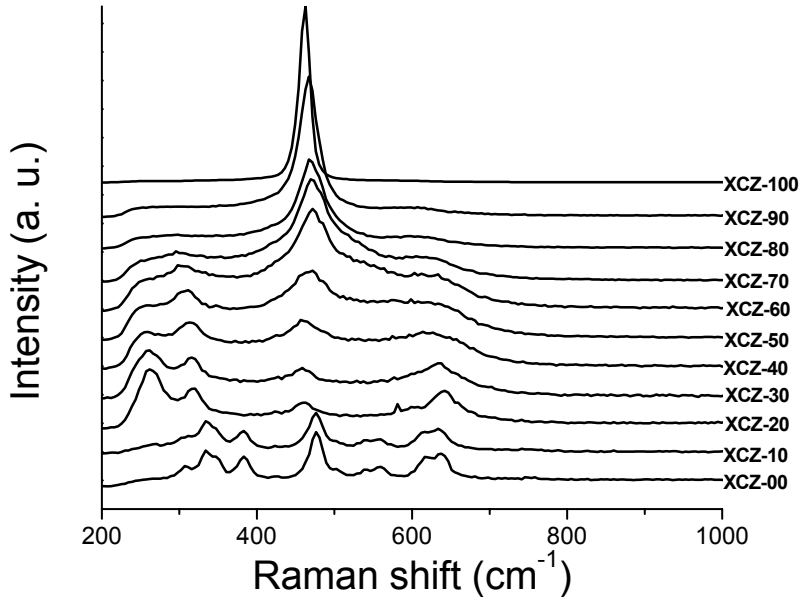

Figure7.6 Raman spectra of $Ce_xZr_{1-x}O_2$ spheres calcined at 900 ºC / 2h.

in the c/a ratio of the tetragonal form. The bands for the tetragonal phase slowly decrease in intensity from XCZ-20 toXCZ-60, where out of five only two bands at 306 and 471 cm^{-1} can be seen. From XCZ-70 to XCZ-100 a single Raman band corresponding to the F_2g mode of the cubic fluorite structure is observed. Comparison of XRD patterns and Raman spectra shows that for the XCZ-20 and XCZ-30 the presence of the tetragonal phase is shown by both methods, indicating that these samples possess the stable tetragonal phase *t*. While for the samples XCZ-40 to XCZ-60 only Raman spectroscopy was able to show the presence of the tetragonal phase, indicating the presence of the metastable tetragonal phase *t'* or *t"*.

Insight on the relation between porosity, surface area and crystallite size was gained by comparison of crystallite sizes obtained by Scherer equation and BET surface area values for the calcined samples. For the samples calcined at 500 ºC the crystallite size influences the surface area. But as the samples are porous, the pore size also influences the surface area. So no direct correlation between surface area and crystallite size can be

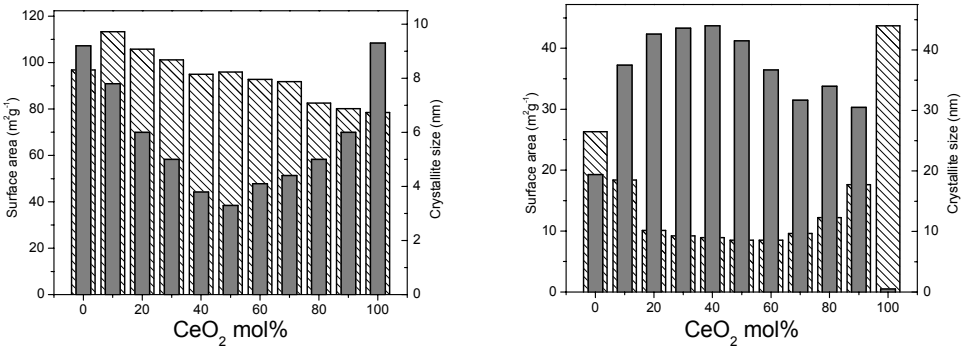

(a) (b)

Figure 7.8 Graphical representation of comparison of crystallite size (gray bars) and surface area (white bars with stripes) for samples calcined at (a) 500 ºC/ 8h and (b) 900 ºC/ 2h.

made. For the sample calcined at 500 ºC the surface area increases continuously from CZ-00 (78 m^2g^{-1}) to CZ-90 (113 m^2g^{-1}) and then drops to 97 m^2g^{-1} for CZ-100. For the pure oxide products (CZ-00 and CZ-100) the crystallite size is largest. As the composition reaches from both the ends to intermediate values, the crystallite size decreases steadily. The minimum crystallite size in the whole series is obtained for CZ-50, which contains 50 mol% each of both the oxides. This phenomenon is indeed interesting and is clear evidence that the solid solution compositions are more stable against sintering compared to individual oxide in case of CeO_2-ZrO_2 binary system.

A similar change in crystallite sizes with composition was obtained for samples calcined at 900 ºC. Even though the external form was maintained in these samples, as the crystallite growth is very large the porous structure is disrupted. Hence the surface area values are dictated by the crystallite size. In general, for non-porous materials, the surface area is inversely proportional to the crystallite size. The same observation was made for the samples calcined at 900 ºC.

7.2 $(Ce_{0.5}Zr_{0.5}O_2)_{0.75}$ $(CuO)_{0.25}$ spheres

For the synthesis of $(Ce_{0.5}Zr_{0.5}O_2)_{0.75}$ $(CuO)_{0.25}$ the process of nanoparticle synthesis was modified as mentioned in the previous section. The rest of the synthesis process was similar to the synthesis of $Ce_xZr_{1-x}O_2$ spheres. These spheres had a grayish green colour. The surface area value of the spheres obtained upon calcination at 500 ºC was 91 m^2g^{-1}. The XRD pattern of the calcined material showed (Fig. 7.9) very broad reflections corresponding to $Ce_{0.5}Zr_{0.5}O_2$. In addition there were very weak reflections corresponding

to the main peaks of monoclinic CuO. These sphere were used for methanol reforming reaction.

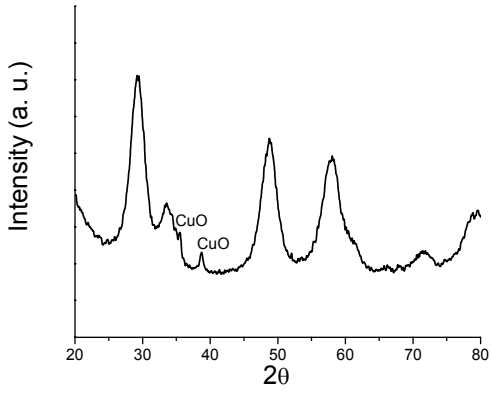

Figure 7.9 XRD pattern of $(Ce_{0.5}Zr_{0.5}O_2)_{0.75}$ $(CuO)_{0.25}$ spheres calcined at 500 ºC / 8h.

The advantages of this preparation method are that the processing period is around one week, which is comparably short. As casting approach is used in the templating process no specific interaction between the template and the nanoparticles is necessary. Samples can be produced on multigram scale.

7.3 Methanol steam reforming

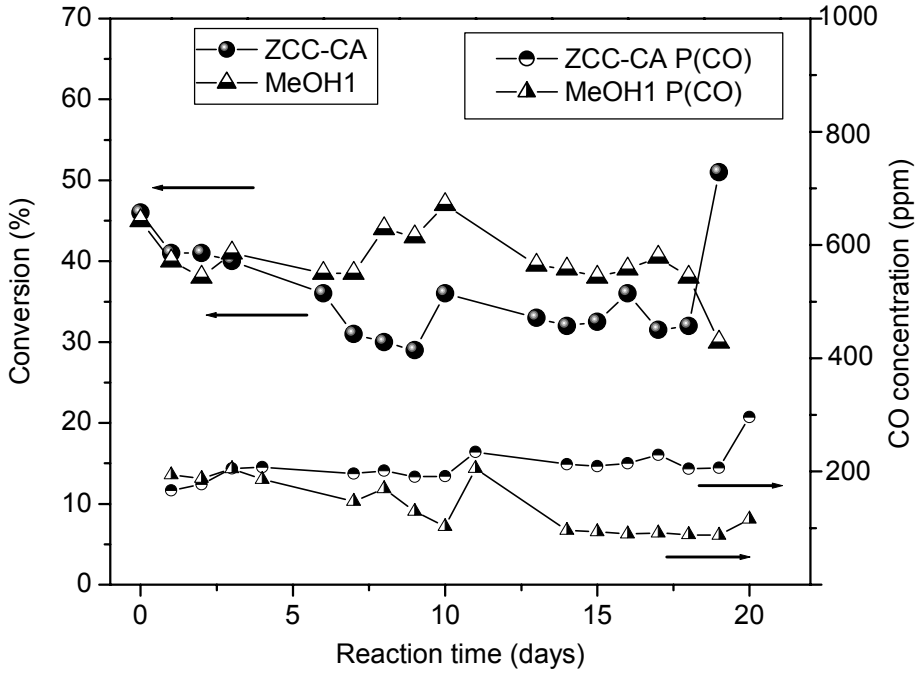

Figure 7.10 Graphical representation of the conversion of methanol in steam reforming reaction over a period of 19 days. ● and ▲ represent % conversion. While ◮ and ◓ represent amount of carbon monoxide in ppm formed during the reaction.

Among the various applications of CeO_2 based materials, there use as active supports in reforming reactions is most popular for their use in fuel cell applications. As a model system we used $(Ce_{0.5}Z_{0.5}O_2)_{0.75}$ $(CuO)_{0.25}$ spheres for catalytic steam reforming of methanol. A commercial product MeOH1 was used as a standard for comparison. The MeOH1 is a CuO-ZnO catalyst with 50 wt % CuO and surface area of 49 m^2g^{-1}. An online gas chromatographer was used to analyze the products of reforming reaction. The results of analysis are depicted in Fig. 7.10. Here the $(Ce_{0.5}Zr_{0.5}O_2)_{0.75}$ $(CuO)_{0.25}$ sample

is labeled as ZCC-CA. The results show that the ZCC-CA catalyst was quite active. In the initial stages the rate conversion was 46 %, which was slightly higher than that for the MeOH1 catalyst. With the time, however, the conversion rate decreased and was in the range between 30-40 %. The amount of carbon monoxide formed was initially less. But with time it increased and remained around 200 ppm. The main aim of this study was to get preliminary results regarding the usefulness of CuO-doped ceria-zirconia beads for reforming reactions. These results are highly promising. Further investigations about the reactions involved in the process and a more detailed characterization are ongoing and hence are out of the scope of the present study.

8. Results and Discussion

8.1 Synthesis of mesoporous $Ce_xZr_{1-x}O_2$ powders

Though the use of nanoparticles to synthesize macroporous materials was widely demonstrated in the literature [33, 41, 42, 122, 123], reports on the synthesis of ordered mesoporous material using liquid crystal templating process are scares [85, 86]. This synthetic approach is particularly challenging and needs careful consideration of various parameters that can possibly affect the process. However, from the point of view of basic research and also from an application point of view, the development and study of mesoporous materials using nanoparticle building block is very interesting/promising.

In the present work, the synthesis of mesoporous $Ce_xZr_{1-x}O_2$ with regular pore size was achieved by using a block-copolymer and $Ce_xZr_{1-x}O_2$ nanoparticle sols through evaporation induced self-assembly process. We used poly(butadiene-*b*-ethylene oxide) (PB-PEO) block-copolymers as structure directing agent. The synthesis of this type of block-copolymer has been reported before [124]. The lyotropic behavior of this class of block-copolymers has been also studied [125], which shows that these block-copolymers form very large spherical micelles and various micellar phases. This was the main reason for choosing this type of block-copolymer. The $Ce_xZr_{1-x}O_2$ nanoparticles are around 2-4 nm in size, hence to form ordered structure it is necessary that the template (micelles) are large enough to direct and stabilize the assembly of nanoparticles.

During the synthesis 0.3 g of the block-co-polymer was dissolved in ethanol, followed by the slow addition of the ethanol-water sol under stirring, containing 0.005 moles of $Ce_xZr_{1-x}O_2$. The resultant transparent solution was transferred into an open petri dish and the solvent was allowed to evaporate to get a transparent gel. The use of purely aqueous

sol did not result in the formation of structured materials. As discussed before, the water from the sol can be replaced up to 90% of the original amount. This is achieved by dialyzing the aqueous sol against ethanol. Before dialysis 10 ml ethanol was added to the aqueous sol to avoid gelation. The interesting feature of this dialysis process is that water acts as a solute, which is extracted by the dialyzing medium, resulting in the reduction of weight of the sol. Thus amount of water remaining in the sol can be calculated approximately from the solid content of the sol, initial weight of the sol, and reduction in weight upon dialysis. It was found that even though ethanol-water sols, containing water less than 5 ml, were stable, its addition to a block-copolymer solution resulted in precipitation of the oxide particles. Sols containing 5 ml or more water were stable when added to the block-copolymer solution and gave a clear solution. The dried gels were obtained by evaporation of the solvent from the clear solution over a period of 3-4 days at room temperature. Best results were obtained for the following composition: 15 ml ethanol, 5 ml H_2O, 0.3 g block copolymer, 0.005 moles oxide content.

The dry gels were heat treated to remove the organics and to obtain mesoporous oxide powders. The stability of the structure upon the heat treatment depends upon the mode of heat treatment. The calcination program used in this case is mild and carried out in a more controlled way as compared to the calcination of the beads. The dry gels were kept in an oven at 100 ºC for one day in order to remove the solvents completely and to compact the gel. These gels were then calcined in an oven under flowing air. The temperature was first raised up to 300 ºC with a rate of 1 ºC min^{-1} and then kept constant at this temperature for 1 hour. The reason for this is that the block co-polymer starts to decompose around 300 ºC and the heat released during the process can disrupt the structure easily. So the decomposition was allowed to take place at slower pace by

keeping the temperature constant at 300 ºC. After that the temperature was raised to 450 ºC and held constant for 2 hours to ensure complete decomposition of organics.

Pure CeO_2 and $Ce_{0.5}Zr_{0.5}O_2$ sols were used for this process. The dried gels of both, CeO_2 and $Ce_{0.5}Zr_{0.5}O_2$ showed a single reflection in the small angle X-ray scattering (SAXS) pattern (Fig. 8.1).

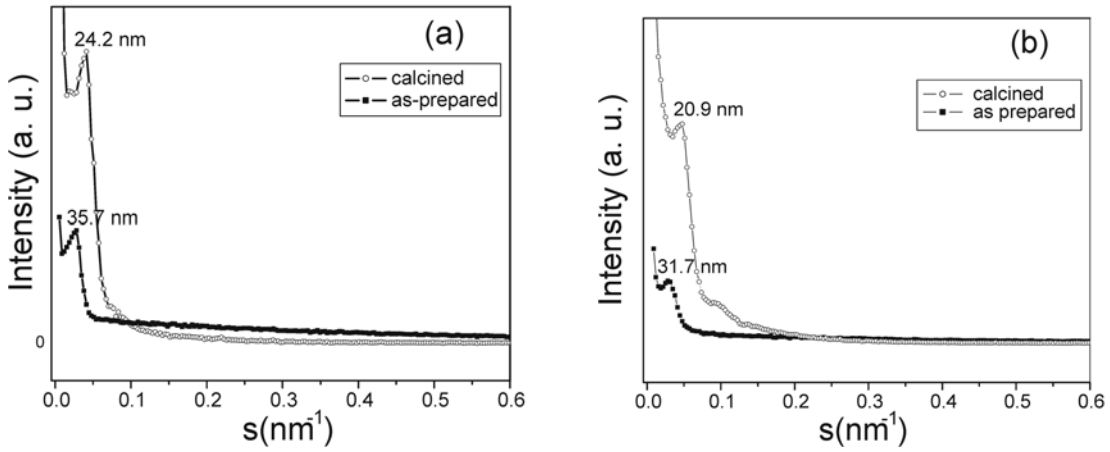

Figure 8.1 Small angle X-ray scattering (SAXS) patterns of (a) CeO_2 (b) $Ce_{0.5}Zr_{0.5}O_2$ systems

Upon calcination the peak position shifts to higher scattering angles indicating a decrease in structural parameter. The peak positions for the calcined samples correspond to structural parameters of 24.2 nm and 20.9 nm for CeO_2 and $Ce_{0.5}Zr_{0.5}O_2$, respectively. The presence of just a single peak in the SAXS patterns indicates lack of long range ordering in the structure.

For TEM analysis of the as-prepared samples (gels), they were embedded in a polymer matrix and ultra thin sections obtained by ultra-microtomy were used. Fig. 8.2 shows TEM images of gels formed from $Ce_{0.5}Zr_{0.5}O_2$ nanoparticles. The structure of the gel consists of spherical pores of diameter around 21 nm. The pores were arranged in a

disordered fashion with occasional presence of clusters arranged in a hexagonal fashion. The higher resolution images (Fig. 8.2b) show that the pore walls had a thickness of roughly 8-10 nm consisting of nanoparticles.

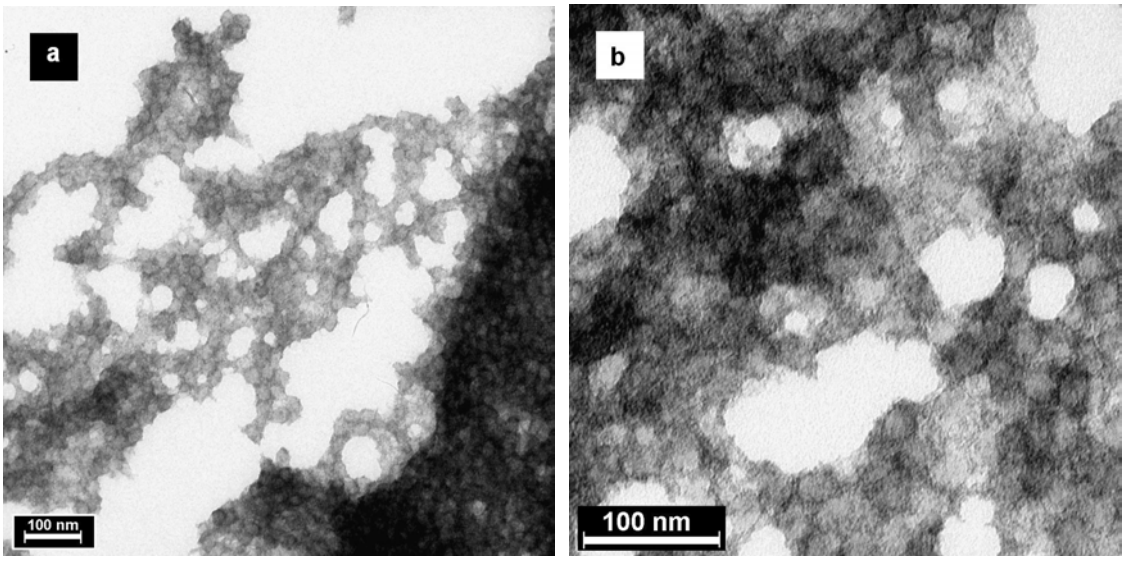

Figure 8.2 TEM images of ultramicrotomed sections of gels obtained using $Ce_{0.5}Zr_{0.5}O_2$ nanoparticles at (a) lower and (b) at higher resolution.

The calcination process gave porous materials. However, the TEM images of the calcined powders show that in addition to highly ordered structures also small fractions of non-structured agglomerates of nanoparticles were present in the samples. Fig. 8.3 shows a well-structured area, illustrating that there was shrinkage in the pore size and the pore wall thickness seemed to increase slightly. Furthermore, increase in the size of the nanoparticles was clearly seen. The nanoparticles grew more in case of pure CeO_2 sample than $Ce_{0.5}Zr_{0.5}O_2$, which is consistent with the results from the previous section.

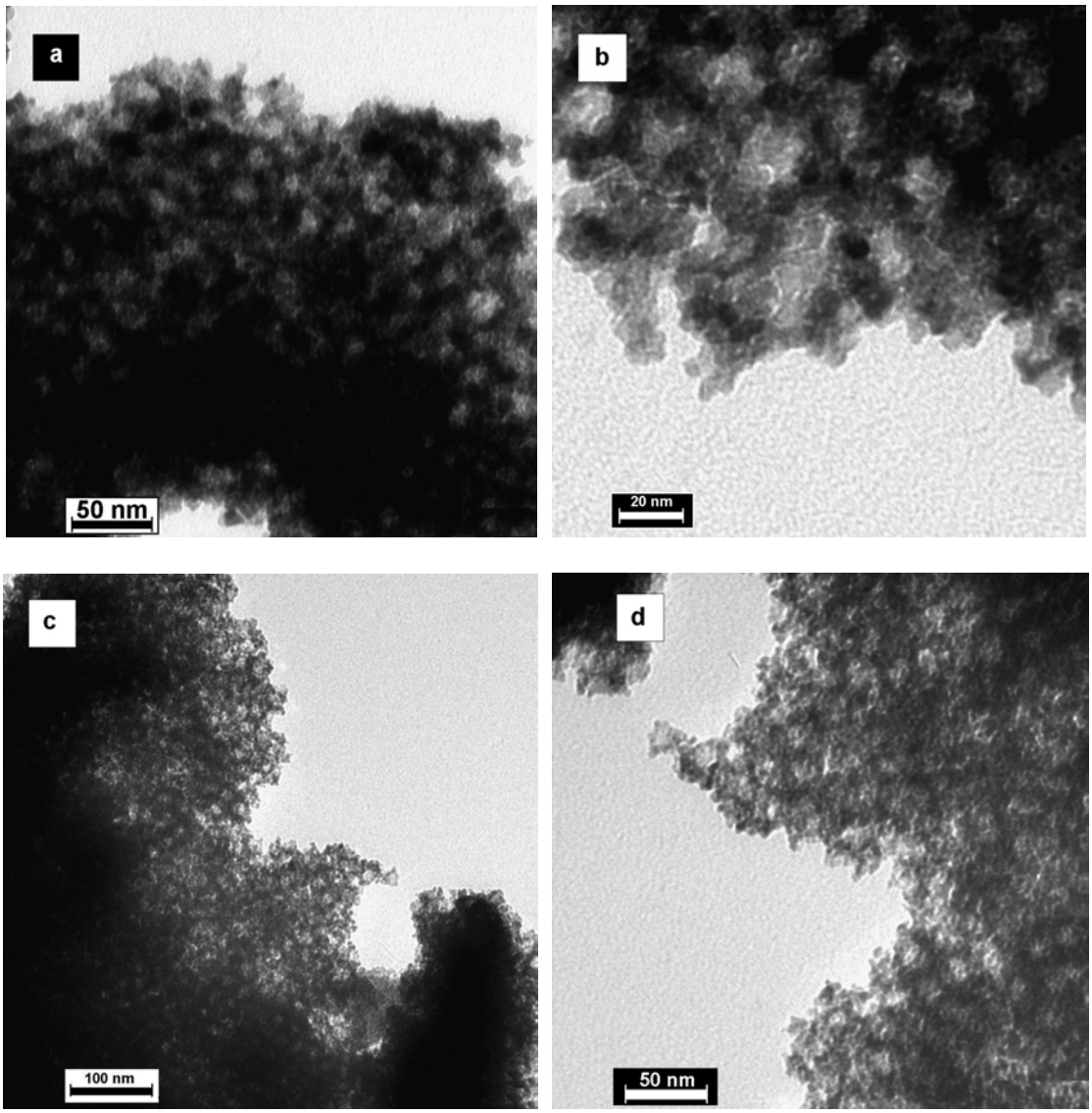

Figure 8.3 TEM images of powders obtained upon calcination at 450 ºC. (a) and (b) mesoporous CeO_2, (c) and (d) mesoporous $Ce_{0.5}Zr_{0.5}O_2$.

Nitrogen sorption studies performed on these samples showed a Type VI isotherm typical of mesoporous materials. Fig. 8.4a shows the nitrogen sorption isotherms of the calcined powders of CeO_2 and $Ce_{0.5}Zr_{0.5}O_2$. Large hysteresis was obtained for both the samples. As discussed in the methods section, the appearance of hysteresis is due to the difference in the adsorption and desorption mechanism from the cylindrical pores. If the pore

opening is smaller than the pores, the effect is more pronounced. According to TEM, it seems that in the present case the pores are spherical in shape. The desorption from such pores will occur at fairly low relative pressures. Hence large hysteresis is observed in case of both the samples. The pore size distribution (Fig 8.4b) was very narrow, giving evidence for the uniformity of the pore structure. The average pore size was seen to be 12 nm.

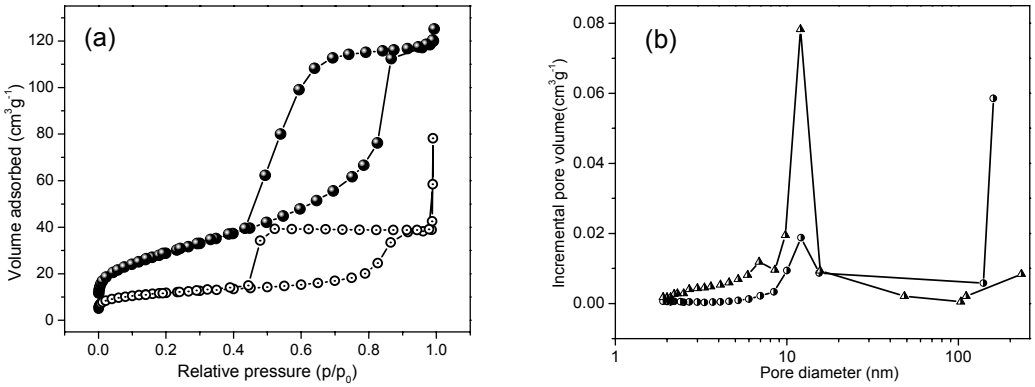

Figure 8.4 (a) Nitrogen sorption isotherms of calcined powders, CeO_2 (⊙) and $Ce_{0.5}Zr_{0.5}O_2$ (●); (b) pore size destribution from BJH analysis of the sorption data, CeO_2 (◑) and $Ce_{0.5}Zr_{0.5}O_2$ (◭).

The surface area values obtained for CeO_2 and $Ce_{0.5}Zr_{0.5}O_2$ were 41 and 105 m^2g^{-1}, respectively. The lower surface area values for the CeO_2 sample is partly due to the higher density of CeO_2 as compared to $Ce_{0.5}Zr_{0.5}O_2$ and partly due to the higher amount of unstructured fraction of the sample generated by the collapse of the pore structure.

In summary, we could demonstrate successfully the use of nanoparticles as building blocks for the synthesis of stable mesoporous materials via evaporation induced self-assembly.

9 Experimental

9.1 Synthesis of macroporous TiO_2-M_2O_3 spheres

9.1.1 Materials

The synthesis of porous TiO_2-In_2O_3, TiO_2-Ga_2O_3 and TiO_2-Al_2O_3 spheres required the use of porous polystyrene/divinyl benzene beads (SOURCE™15 RPC beads, S15RPC, Amersham Biosciences) as template and the metal alkoxide precursors titanium (IV) isopropoxide (Aldrich, 99.999%), aluminum (III) isopropoxide (Aldrich, 99.99%), gallium (III) isopropoxide (Alfa Aesar 99%), and indium (III) isopropoxide (Chemat Technology Inc. AR grade). The alkoxide precursors were used as obtained from the suppliers. The S15RPC beads are rigid, porous, and spherical with an average diameter of 15 μm and are conventionally used as reverse phase chromatography media. The beads were purchased as dispersion in 20 % ethanol. To obtain dry beads for templating the solvent was evaporated by heating the dispersion in an oven at 60 ºC for 48 h.

9.1.2 Procedure

Titanium dioxide and the mixed titania-metal oxide (metal = In, Al and Ga) spheres, with compositions as follows: TiO_2 (100%); TiO_2 (95 wt.%)-M_2O_3 (5 wt.%); TiO_2 (90 wt.%)-M_2O_3 (10 wt.%); and TiO_2 (85 wt.%)-M_2O_3 (15 wt.%) were synthesized by using mixed precursors prepared by dissolving the appropriate amount of metal isopropoxide in the liquid titanium (IV) isopropoxide. In a typical synthesis 1 g of the mixed precursor solution and 1 g of the dry beads were mixed together in a plastic bottle and the bottle was sealed to avoid contact with atmospheric moisture. The bottle was agitated overnight to ensure infiltration of the mixed precursor throughout the porous matrices of the beads. Subsequently, 100 ml of water was added to the impregnated beads to initiate hydrolysis

and condensation of the alkoxide precursor and the mixture was stirred for 24 h. The hybrid beads were filtered using a sintered glass funnel (ROBU®, Germany) No.3 and washed with water to remove small particles formed outside of the beads. The washed beads were dried in an oven at 60 ºC for 24 h, followed by calcination at 550 ºC (ramp of 1.5 h) for 10 h in flowing air, yielding porous TiO_2-metal oxide spheres. To monitor crystal phase transformations, further heating of the spheres was performed at 750 ºC (ramp 2h) for 10 h under air and 950 ºC (ramp 2.5 h) for 10 h under air.

9.1.3 Pyridine adsorption study

Pyridine adsorption studies were performed on the porous inorganic spheres (calcined at 550 ºC) by Infrared studies to determine surface acidity, using a BIO-RAD FTS 6000 spectrometer. For this purpose the samples were first evacuated in glass tubes to a pressure of 0.1 mbar at 150 ºC for 90 min and subsequently cooled to room temperature. Liquid pyridine was added to soak the samples completely and then they were evacuated again to 0.1 mbar at 150 ºC for 90 min. IR spectra of samples before and after the addition of pyridine were recorded.

9.1.4 Photocatalytic degradation of 2-chlorophenol

The photocatalytic activity of the TiO_2-based porous metal oxide spheres was measured by monitoring the photo oxidation of 2-chlorophenol. The photochemical reactor was a cylindrical flask (~ 90 ml) with a quartz window (diameter 3.6 cm) on the bottom equipped with IR-vis. and UV filters for transmitting light within 340 and 500 nm, and a magnetic stir bar. The illumination source was a high-pressure mercury lamp (Philips

HPK 125 W, total radiant flux was 10 mW cm^{-2}). For the irradiation experiments a mixture of 40 ml of the 2-chlorophenol solution (10^{-3} M) and the photocatalyst (2 g L^{-1}) was employed. The irradiation time was set to 1.5 h in all experiments. pH adjustments were made by using a pH-stat. Commercial titanium dioxide, Degussa P25, was used as a reference for comparison of the photocatalytic activity. The concentration of 2-chlorophenol was determined by HPLC using an LDC/Milton Roy system, which consisted of a Constametric 3000 isocratic pump and a Spectro Monitor D UV-detector adjusted to 254 nm. A reverse-phase column (25 cm long and 4.6 mm internal diameter) packed with Spherisorb 5 0DS2 was used. The mobile phase was a mixture of methanol (35 %), deionized, doubly distilled water (55 %), and acetonitrile. Identification of the eluting compounds was made by comparing their retention times with those of commercial compounds purchased from Aldrich.

9.3 Synthesis of $Ce_xZr_{1-x}O_2$ nanoparticles

9.3.1 Materials

Ammonium cerium nitrate, $(NH_4)_2Ce(NO_3)_6$ (Aldrich 98.5%), zirconyl nitrate, $ZrO(NO_3)_2 \cdot x\ H_2O$ (Aldrich 99.99%), zirconyl chloride, $ZrOCl_2 \cdot\ 8H_2O$(Riedel-de Haën 99.5%), copper nitrate hemipentahydrate $Cu(NO_3)_2 \cdot 2.5\ H_2O$ (Aldrich 98%); ammonia, NH_3 (Fluka 25% aqueous solution), sodium hydroxide, NaOH (Aldrich AR grade), and nitric acid, HNO_3 (Aldrich 90%) were used as received. The exact molecular weight of $ZrO(NO_3)_2 \cdot x\ H_2O$ calculated from thermal analysis was found to be 276.8 g.

9.3.2 Procedure

$Ce_xZr_{1-x}O_2$ nanoparticle sols with x = 0, 0.1, 0.2, 0.3… x = 1 were synthesized. For the synthesis of the sols with a total metal content of 0.005 mole, the appropriate amounts of $(NH_4)_2Ce(NO_3)_6$ and $ZrOCl_2{\cdot}8H_2O$ were dissolved together in 40 ml distilled water. 1.3-1.5 ml of 25% aqueous NH_3 solution was added rapidly to this solution to raise the pH above 10 leading to co-precipitation of the metal hydroxides. The precipitate was washed repeatedly with distilled water until the washing was tested neutral by litmus paper. 5 ml distilled water and a calculated amount of 90% HNO_3 was added to the washed precipitate. Ratio of HNO_3-to-metal content was varied systematically from 1:1 for pure CeO_2 sample to 1.5:1 for pure ZrO_2 sample. The resultant suspension was sonicated (Elma Transsonic Digital S, 140% ultrasound power) for 45-60 min to obtain a transparent sol. During sonication, the temperature of the water bath increased to 40-50°C. The pH of these sols was below 2. The sols were dialyzed against Millipore water using Spectra/Por membranes (MWCO: 6-8000). The pH of the dialyzed sols was in the range of 4-5. Transparent gels were obtained from these sols upon evaporation of water.

For the synthesis of $(Ce_{0.5}Zr_{0.5}O_2)_{0.75}(CuO)_{0.25}$ sols, $ZrO(NO_3)_2{\cdot}xH_2O$ was used instead of $ZrOCl_2{\cdot}\ 8H_2O$. For the synthesis of 0.005 mole metal oxide containing sol, calculated amounts of $Cu(NO_3)_2{\cdot}2.5\ H_2O$, $ZrO(NO_3)_2{\cdot}xH_2O$ and $(NH_4)_2Ce(NO_3)_6$ were dissolved together in 40 ml distilled water. Instead of aqueous ammonia, NaOH solution was used. 1 g of NaOH was dissolved in 5 ml distilled water and added rapidly to the mixed metal salt solution. The pH of the solution was raised above 10. The rest of the procedure was the same as the synthesis of $Ce_xZr_{1-x}O_2$ sols.

9.4 Synthesis of mesoporous $Ce_xZr_{1-x}O_2$ and $(Ce_xZr_{1-x}O_2)_a$ $(CuO)_b$ spheres

9.4.1 Materials

Un-dialyzed sols of $Ce_xZr_{1-x}O_2$ and $(Ce_{0.5}Zr_{0.5}O_2)_{0.75}(CuO)_{0.25}$ were used for the synthesis. Wet beads of Amberlite® XAD-16 were purchased from Aldrich.

9.4.2 Procedure

The beads received from the manufacturer contained Na_2CO_3 and NaCl to prevent bacterial growth. So it was necessary to clean the beads before use. The beads were washed repeatedly with distilled water until the conductivity of washing was below 1 μS cm^{-1}. After washing the beads were stored in distilled water. For the templating process undialyzed sols of $Ce_xZr_{1-x}O_2$ and $(Ce_{0.5}Zr_{0.5}O_2)_{0.75}(CuO)_{0.25}$ were used. 1.5 ml of the washed wet beads and sols containing 0.005 mole oxide were mixed together and kept in an oven at 60 ºC for 2 days to evaporate the solvent completely. These beads were then dried further at 90-100 ºC for 1day. The dried beads were washed thoroughly to clean the surface of beads and to remove excess deposit from the surface if present. The washed beads were again dried at 60ºC/1 day and calcined in the oven at 500 ºC for 1.5 h in N_2 and then 8 h in air with a ramp of 2.5 h in N_2. Well-crystallized porous oxide spheres with colors from dark yellow to white were obtained with increase in content of ZrO_2.

9.4.3 Methanol steam reforming

The steam reforming of methanol using $(Ce_{0.5}Zr_{0.5}O_2)_{0.75}(CuO)_{0.25}$ spheres as catalyst was carried out in a fixed bed reactor. The reactor consisted of a stainless steel tube in which 0.394 g of the catalyst beads were packed with silica beads (diameter =750 μm) laid above and below the catalyst beads. The reactor was heated at 250 ºC and 1:1 mixture of methanol and water was fed to the reactor at a flow rate of 0.07 ml/min. The effluent gases were analyzed by an online gas chromatographer (Varian CP-3800). The reaction was carried out over a period of 19 days. For comparison a commercial catalyst obtained from Süd Chemie, Germany, which contained 50 wt % CuO in addition to ZnO and Al_2O_3 was used.

9.5 Synthesis of Mesoporous $Ce_xZr_{1-x}O_2$ powders

9.5.1 Materials.

Un-dialyzed CeO_2 and $Ce_{0.5}Zr_{0.5}O_2$ sols were used as precursors in the synthesis. Poly(butadiene-*b*-ethylene oxide) (PB-PEO) block copolymer having the formula $(PB)_{320}(PEO)_{568}$ were kindly donated/provided by Dr. H. Schlaad of the Max Plank Institute of Colloids and Interfaces, Golm, Germany. Both the blocks are narrowly distributed with M_w = 17290 for polybutadiene block and M_w = 24992 for polyethylene oxide block. The synthesis of this block-copolymer was done as reported in the literature [124].

9.5.2 Procedure

Un-dialyzed aqueous sols with 0.005 mole oxide content were taken as precursor. To the aqueous sol 10 ml of absolute ethanol was added. The ethanol/water sol was dialyzed

against absolute ethanol to remove water using Spectra/Por membranes (MWCO: 6-8000). Prior to the dialysis, weights of the dialysis membrane, clips and the sol were determined separately. From the oxide content, the weight of ethanol added and the weight of the sol, the amount of water in the sol was calculated. The sol was then transferred to dialysis membrane and dialyzed against abosolute ethanol. Weight of the membrane tube containing the sol was checked every few minutes and absolute ethanol was replaced intermittently. The dialysis was carried till approximately 5 ml of water remained in the sol. 0.3 g of the PB-PEO block-copolymer was dissolved in 5 ml absolute ethanol and to it the ethanol/water sol was added drop wise with constant stirring to obtain a clear solution. This solution was transferred to a petridish and the solvent was allowed to evaporate at ambient condition for 3-4 days to obtain transparent a yellow gel. The gel was aged at 100 ºC for one day and then calcined in flowing air at 450 ºC for 2h. A special calcination program was used in which the temperature was raised to 300 ºC with a ramp of 1 ºC/min. After reaching 300 ºC the temperature was kept constant for 1 h, raised to 450 ºC and held constant at 450 ºC for 2h. Upon calcination, powdered yellow products were obtained.

9.6 Characterization

9.6.1 Powder X-ray diffraction (XRD) measurements

An Enraf-Nonius PDS-120 instrument and a D8 advance diffractometer (Bruker AXS, Germany) with Cu-Kα radiation with a wavelength of 1.540 Å obtained using Ni/C mirror were used to obtain XRD data of all the samples. The samples were analyzed in reflection mode.

9.6.2 Small angle X-ray scattering (SAXS)

SAXS data for the samples were obtained by using Kratky camera assembly manufactured by Anton-par, Germany. The samples were analyzed in transmission mode under vacuum with an X-ray source of Cu-Kα radiation.

9.6.3 Scanning electron (SEM) microscopy

A Gemini Leo-1550 instrument was used for obtaining SEM images of the samples. The samples were loaded on carbon-coated stubs and sputter coated with Au/Pd alloy prior to analysis.

9.6.3 Transmission electron (TEM) microscopy

TEM images of samples were obtained by using a Zeiss EM-912 Omega instrument operating at acceleration voltage of 100 kV. To obtain thin cross-section of samples, they were embedded in an LR-White resin. Ultra thin sections were obtained using a Leica ultracut UCT ultramicrotome. These sections were supported on carbon-coated copper grids. Alternatively for powders the samples were dispersed in a suitable solvent and a drop of this suspension was laid on the carbon-coated copper grid. The solvent was allowed to evaporate to form a thin layer of sample on the copper grid.

A CM200FEG (Philips) microscope, operated at 200kV, equipped with a field emission gun was used for high-resolution transmission electron microscopy (HRTEM) and selected area electron diffraction (SAED).

9.6.4 Nitrogen sorption studies.

Nitrogen sorption studies were carried out using a Micromeritics Tristar-3000 instrument. For the analysis the samples were transferred into sample tubes and evacuated at 150 ºC for at least 6 hour. The analysis was carried out at liquid nitrogen temperature (-196 ºC). The specific surface area was calculated by applying BET method of analysis.

9.6.5 Infrared spectroscopy

A BIO-RAD FTS 6000 spectrometer was used for FT-IR analysis of the samples. No specific sample preparation method was necessary for the analysis using this instrument. Spectra were recorded in the range from 400-4000 cm^{-1}.

9.6.6 Raman spectroscopy

All Raman spectra were recorded with DILOR LABRAM 1 spectrometer. A He-laser (632.8 nm, Melles Griot, 17 mW) was used for excitation. The laser light was focused onto the sample using a 10x objective lens (Olympus) and the spectra were recorded in backscattering geometry. The laser power at the sample location was measured and found to be less then 1 mW. The entrance slit was set to 100 μm giving a spectral width of 5 cm^{-1}. A notch filter was applied to cut off the laser line and the Rayleigh scattering up to about 150 cm^{-1}. Each spectrum is the average of 5 accumulations at an integration time of 60 seconds.

9.6.5 Analytical ultracentrifugation

The particle size distribution was studied for sols using Beckman Optima XL-I analytical ultracentrifuge (AUC) (Beckman Instruments, Palo alto, CA) equipped with Rayleigh interference and UV absorption optics.

10 Summary

1. In this work the synthesis of porous metal oxides using a wide variety of different structure directing agents (templates) and precursor materials is demonstrated. The effect of template, synthetic mode and composition on the physico-chemical properties of the final materials, together with the catalytic properties, was investigated in detail.
2. The first section describes the synthesis of macroporous TiO_2-M_2O_3 (M = Al, Ga, In) spheres using the corresponding metal alkoxides in a sol-gel process and macroporous polystyrene reverse phase chromatography beads (source™ 15RPC) as template.
3. SEM and TEM analysis shows that the morphology of the template was maintained in the final oxide spheres, which were monodispersed, highly porous with high BET surface area up to 195 m^2g^{-1}.
4. From XRD studies it is observed that the addition of a second metal oxide (M_2O_3, M = Al, Ga, In) to TiO_2 is effective in retarding the crystallite growth and the anatase to rutile phase transformation even on calcination at 750 ºC. Furthermore, results from pyridine adsorption studies indicate that the second metal oxide also enhances the surface acidity through creation of Lewis acid site.
5. TiO_2-M_2O_3 spheres show better photocatalytic activity for the degradation of 2-Chlorophenol as compared to the pure TiO_2 spheres. The enhancement in the activity is greatest for the samples containing 5 wt% of Al_2O_3, Ga_2O_3 and In_2O_3, which are even better than the standard catalyst Degussa P25. In addition, the dependence of pH

on the photocatalytic activity is different for the TiO_2-M_2O_3 spheres than for pure TiO_2, owing to the modification in surface properties of these samples.

6. In the second section, the synthesis of $Ce_xZr_{1-x}O_2$ and $(Ce_xZr_{1-x}O_2)_a(CuO)_b$ nanoparticle sols is demonstrated. The process involves hydroxide co-precipitation of mixed metal salts and peptization of the primary particles by ultrasonication using nitric acid as peptizing agent.
7. AUC analysis of these nanoparticle sols shows a narrow particle size distribution. HRTEM and XRD studies show that the particles are as small as 2.5 nm, highly crystalline and defect free. Exceptions are the pure ZrO_2 and the 10 mol% containing CeO_2 samples, which are amorphous. Moreover, XRD studies supplemented by Raman studies show the formation of solid solution over the entire composition range.
8. The third section demonstrates the use of $Ce_xZr_{1-x}O_2$ and $(Ce_xZr_{1-x}O_2)_a(CuO)_b$ as nanoparticulate precursors to synthesize mesoporous spheres of large macroscopic sizes. Mesoporous polymeric beads Amberlite® XAD-16 are used as templates.
9. SEM and TEM results show that the morphology of the template beads is reflected in the final product. Though the pore structure of the product spheres is not an exact inverse replica of the template beads, the influence of the template can be clearly seen.
10. From the nitrogen sorption analysis it follows that the oxide spheres, like the template beads, are mesoporous in nature and surface area values are up to 113 m^2g^{-1}.
11. XRD and Raman studies on samples calcined at 900 ºC show the evolution of the crystal structure and the transition from the monoclinic to the tetragonal, metastable tetragonal and cubic crystal structures from pure ZrO_2 to pure CeO_2. The crystallite

size calculated from XRD data shows the interesting result that the crystallite size is minimum for intermediate compositions, while it is maximum for the pure oxide, indicating that the solid solution formation results in retarding of crystal growth.

12. Further comparison of BET surface area and crystallite sizes of samples calcined at 500 ºC and 900 ºC shows that there is less correlation between the two factors lower calcination temperature as the template induced porosity dictates the surface area values. 900 ºC calcined sample show inverse relation between crystallite size and surface area indicating that the pore structure is lost and the porosity in the sample is interparticle porosity.
13. Methanol reforming reactions performed on $(Ce_{0.5}Zr_{0.5}O_2)_{0.75}(CuO)_{0.25}$ samples show that they are catalytically as active as commercial catalysts with a conversion efficiency up to 46 %. However, high amount of CO is also produced and this is not desirable.
14. The last section describes the use of $Ce_xZr_{1-x}O_2$ nanoparticles and poly(butadiene-*b*-ethylene oxide) (PB-PEO) block-copolymers to obtain highly crystalline mesoporous powders via evaporation induced self-assembly.
15. The SAXS data show a single peak for the as-prepared and calcined product, indicating that the process successfully gives porous materials with regular pore sizes. However, the absence of second order reflections shows a lack of long range ordering.
16. TEM images of as-prepared sample show large spherical pores with an average diameter of 21 nm and a wall thickness of 8-10 nm. The calcined samples indicate to some extent shrinkage in pore size and increase in particle size within the pore walls.

17. The nitrogen sorption data show type VI isotherm typical of mesoporous materials with large hysteresis due to the spherical pore and bottleneck effect. The pore size distribution is very narrow with an average pore size of 12 nm.
18. In general, the use of templaing techniques and a detailed study of various aspects of templating processes have been successfully demonstrated in the present work.

11 References

1. Feynman, R. P. in *Annual Meeting of the American Physical Society* (Article available on web at www.zyvex.com/nanotech/feynman.html, California institute of Technology, 1959)

2. Mackay, A. L. "Flexicrystallography - curved surfaces in chemical structures". *Curr. Sci.* **69**, 151-161 (1995)

3. Mann, S. and Ozin, G. A. "Synthesis of inorganic materials with complex form". *Nature* **382**, 313-318 (1996)

4. Antonietti, M. and Ozin, G. A. "Promises and problems of mesoscale materials chemistry or why meso?" *Chem. Eur. J.* **10**, 29-41 (2004)

5. Mann, S., Burkett, S. L., Davis, S. A., Fowler, C. E., Mendelson, N. H., Sims, S. D., Walsh, D. and Whilton, N. T. "Sol-gel synthesis of organized matter". *Chem. Mater.* **9**, 2300-2310 (1997)

6. Gregg, S. J. and Sing, K. S. W. *Adsorption, surface Area and Porosity* (Academic Press, San Diego, CA, 1982).

7. Ferey, G. "Microporous solids: From organically templated inorganic skeletons to hybrid frameworks ... ecumenism in chemistry". *Chem. Mater.* **13**, 3084-3098 (2001)

8. Kresge, C. T., Leonowicz, M. E., Roth, W. J., Vartuli, J. C. and Beck, J. S. "Ordered mesoporous molecular-sieves synthesized by a liquid-crystal template mechanism". *Nature* **359**, 710-712 (1992)

9. Huo, Q. S., Margolese, D. I., Ciesla, U., Feng, P. Y., Gier, T. E., Sieger, P., Leon, R., Petroff, P. M., Schuth, F. and Stucky, G. D. "Generalized synthesis of periodic surfactant inorganic composite-materials". *Nature* **368**, 317-321 (1994)

10. Antonelli, D. M. and Ying, J. Y. "Synthesis of hexagonally packed mesoporous TiO_2 by a modified sol-gel method". *Angew. Chem. Int. Ed. Engl.* **34**, 2014-2017 (1995)

11. Antonelli, D. M. and Ying, J. Y. "Synthesis of a stable hexagonally packed mesoporous niobium oxide molecular sieve through a novel ligand-assisted templating mechanism". *Angew. Chem.-Int. Ed. Engl.* **35**, 426-430 (1996)

12. Antonelli, D. M. and Ying, J. Y. "Synthesis and characterization of hexagonally packed mesoporous tantalum oxide molecular sieves". *Chem. Mater.* **8**, 874-881 (1996)

13. Pacheco, G., Zhao, E., Garcia, A., Sklyarov, A. and Fripiat, J. J. "Syntheses of mesoporous zirconia with anionic surfactants". *J. Mater. Chem.* **8**, 219-226 (1998)

14. Pacheco, G., Zhao, E., Garcia, A., Sklyarov, A. and Fripiat, J. J. "Mesoporous zirconia obtained with anionic templates". *Chem. Commun.*, 491-492 (1997)

15. Luca, V., MacLachlan, D. J., Hook, J. M. and Withers, R. "Synthesis and characterization of mesostructured vanadium oxide". *Chem. Mater.* **7**, 2220-2223 (1995)

16. Attard, G. S., Glyde, J. C. and Goltner, C. G. "Liquid-Crystalline Phases as Templates for the Synthesis of Mesoporous Silica". *Nature* **378**, 366-368 (1995)

17. Yang, P. D., Zhao, D. Y., Margolese, D. I., Chmelka, B. F. and Stucky, G. D. "Generalized syntheses of large-pore mesoporous metal oxides with semicrystalline frameworks". *Nature* **396**, 152-155 (1998)

18. Ying, J. Y., Mehnert, C. P. and Wong, M. S. "Synthesis and applications of supramolecular-templated mesoporous materials". *Angew. Chem. Int. Ed.* **38**, 56-77 (1999)

19. Soler-illia, G. J. D., Sanchez, C., Lebeau, B. and Patarin, J. "Chemical strategies to design textured materials: From microporous and mesoporous oxides to nanonetworks and hierarchical structures". *Chem. Rev.* **102**, 4093-4138 (2002)

20. Sayari, A. and Liu, P. "Non-silica periodic mesostructured materials: recent progress". *Microporous Mater.* **12**, 149-177 (1997)

21. Ma, Y., Tong, W., Zhou, H. and Suib, S. L. "A review of zeolite-like porous materials". *Microporous Mesoporous Mat.* **37**, 243-252 (2000)

22. Velev, O. D., Jede, T. A., Lobo, R. F. and Lenhoff, A. M. "Porous silica via colloidal crystallization". *Nature* **389**, 447-448 (1997)

23. Holland, B. T., Blanford, C. F. and Stein, A. "Synthesis of macroporous minerals with highly ordered three-dimensional arrays of spheroidal voids". *Science* **281**, 538-540 (1998)

24. Imhof, A. and Pine, D. J. "Ordered macroporous materials by emulsion templating". *Nature* **389**, 948-951 (1997)

25. Caruso, R. A., Giersig, M., Willig, F. and Antonietti, M. "Porous "coral-like" TiO_2 structures produced by templating polymer gels". *Langmuir* **14**, 6333-6336 (1998)

26. Caruso, R. A. and Schattka, J. H. "Cellulose acetate templates for porous inorganic network fabrication". *Adv. Mater.* **12**, 1921-1923 (2000)

27. Caruso, R. A., Antonietti, M., Giersig, M., Hentze, H. P. and Jia, J. G. "Modification of TiO_2 network structures using a polymer gel coating technique". *Chem. Mater.* **13**, 1114-1123 (2001)

28. Caruso, R. A. and Antonietti, M. "Sol-gel nanocoating: An approach to the preparation of structured materials". *Chem. Mater.* **13**, 3272-3282 (2001)

29. Caruso, R. A. and Antonietti, M. "Silica films with bimodal pore structure prepared by using membranes as templates and amphiphiles as porogens". *Adv. Funct. Mater.* **12**, 307-312 (2002)

30. Lakshmi, B. B., Dorhout, P. K. and Martin, C. R. "Sol-gel template synthesis of semiconductor nanostructures". *Chem. Mater.* **9**, 857-862 (1997)

31. Jung, J. H., Ono, Y., Hanabusa, K. and Shinkai, S. "Creation of both right-handed and left-handed silica structures by sol-gel transcription of organogel fibers comprised of chiral diaminocyclohexane derivatives". *J. Am. Chem. Soc.* **122**, 5008-5009 (2000)

32. Kobayashi, S., Hamasaki, N., Suzuki, M., Kimura, M., Shirai, H. and Hanabusa, K. "Preparation of helical transition-metal oxide tubes using organogelators as structure-directing agents". *J. Am. Chem. Soc.* **124**, 6550-6551 (2002)

33. Davis, S. A., Patel, H. M., Mayes, E. L., Mendelson, N. H., Franco, G. and Mann, S. "Brittle bacteria: A biomimetic approach to the formation of fibrous composite materials". *Chem. Mater.* **10**, 2516-2524 (1998)

34. Caruso, R. A., Schattka, J. H. and Greiner, A. "Titanium dioxide tubes from sol-gel coating of electrospun polymer fibers". *Adv. Mater.* **13**, 1577-1579 (2001)

35. Zhang, B. J., Davis, S. A. and Mann, S. "Starch gel templating of spongelike macroporous silicalite monoliths and mesoporous films". *Chem. Mater.* **14**, 1369-1375 (2002)

36. Yang, D., Qi, L. M. and Ma, J. M. "Eggshell membrane templating of hierarchically ordered macroporous networks composed of TiO_2 tubes". *Adv. Mater.* **14**, 1543-1546 (2002)

37. Seshadri, R. and Meldrum, F. C. "Bioskeletons as templates for ordered, macroporous structures". *Adv. Mater.* **12**, 1149- 1151(2000)

38. Fowler, C. E., Shenton, W., Stubbs, G. and Mann, S. "Tobacco mosaic virus liquid crystals as templates for the interior design of silica mesophases and nanoparticles". *Adv. Mater.* **13**, 1266-1269 (2001)

39. Niederberger, M., Muhr, H. J., Krumeich, F., Bieri, F., Gunther, D. and Nesper, R. "Low-cost synthesis of vanadium oxide nanotubes via two novel non-alkoxide routes". *Chem. Mater.* **12**, 1995-2000 (2000)

40. Davis, S. A., Breulmann, M., Rhodes, K. H., Zhang, B. and Mann, S. "Template-directed assembly using nanoparticle building blocks: A nanotectonic approach to organized materials". *Chem. Mater.* **13**, 3218-3226 (2001)

41. Breulmann, M., Davis, S. A., Mann, S., Hentze, H. P. and Antonietti, M. "Polymer-gel templating of porous inorganic macro-structures using nanoparticle building blocks". *Adv. Mater.* **12**, 502-507 (2000)

42. Shchukin, D. G., Schattka, J. H., Antonietti, M. and Caruso, R. A. "Photocatalytic properties of porous metal oxide networks formed by nanoparticle infiltration in a polymer gel template". *J. Phys. Chem. B* **107**, 952-957 (2003)

43. Subramania, G., Constant, K., Biswas, R., Sigalas, M. M. and Ho, K. M. "Optical photonic crystals fabricated from colloidal systems". *Appl. Phys. Lett.* **74**, 3933-3935 (1999)

44. Subramanian, G., Manoharan, V. N., Thorne, J. D. and Pine, D. J. "Ordered macroporous materials by colloidal assembly: A possible route to photonic bandgap materials". *Adv. Mater.* **11**, 1261-1265 (1999)

45. Diebold, U. "The surface science of titanium dioxide". *Surf. Sci. Rep.* **48**, 53-229 (2003)

46. Hoffmann, M. R., Martin, S. T., Choi, W. Y. and Bahnemann, D. W. "Environmental applications of semiconductor photocatalysis". *Chem. Rev.* **95**, 69-96 (1995)

47. Kim, J., Song, K. C., Foncillas, S. and Pratsinis, S. E. "Dopants for synthesis of stable bimodally porous titania". *J. Eur. Ceram. Soc.* **21**, 2863-2872 (2001)

48. Poznyak, S. K., Talapin, D. V. and Kulak, A. I. "Structural, optical, and photoelectrochemical properties of nanocrystalline TiO_2-In_2O_3 composite solids and films prepared by sol-gel method". *J. Phys. Chem. B* **105**, 4816-4823 (2001)

49. Schattka, J. H., Shchukin, D. G., Jia, J. G., Antonietti, M. and Caruso, R. A. "Photocatalytic activities of porous titania and titania/zirconia structures formed by using a polymer gel templating". *Chem. Mater.* **14**, 5103-5108 (2002)

50. Birkefeld, L. D., Azad, A. M. and Akbar, S. A. "Carbon-monoxide and hydrogen detection by anatase modification of titanium-dioxide". *J. Am. Ceram. Soc.* **75**, 2964-2968 (1992)

51. Tang, H., Prasad, K., Sanjines, R. and Levy, F. "TiO_2 anatase thin-films as gas sensors". *Sens. Actuator B-Chem.* **26**, 71-75 (1995)

52. Kaspar, J., Fornasiero, P. and Graziani, M. "Use of CeO_2-based oxides in the three-way catalysis". *Catal. Today* **50**, 285-298 (1999)

53. Yashima, M., Kakihana, M. and Yoshimura, M. "Metastable-stable phase diagrams in the zirconia-containing systems utilized in solid-oxide fuel cell application". *Solid State Ion.* **86-8**, 1131-1149 (1996)

54. Trovarelli, A. "Catalytic properties of ceria and CeO_2-containing materials". *Catal. Rev. Sci. Eng.* **38**, 439-520 (1996)

55. Trovarelli, A. *Catalysis by Ceria and Related Materials* (ed. Hutchings, G. H.) (Imperial College Press, 2002).

56. Kaspar, J. and Fornasiero, P. "Nanostructured materials for advanced automotive de-pollution catalysts". *J. Solid State Chem.* **171**, 19-29 (2003)

57. Kaspar, J., Fornasiero, P. and Hickey, N. "Automotive catalytic converters: current status and some perspectives". *Catal. Today* **77**, 419-449 (2003)

58. Mills, A. and LeHunte, S. "An overview of semiconductor photocatalysis". *J. Photochem. Photobiol. A-Chem.* **108**, 1-35 (1997)

59. Linsebigler, A. L., Lu, G. Q. and Yates, J. T. "Photocatalysis on TiO_2 surfaces - principles, mechanisms, and selected results". *Chem. Rev.* **95**, 735-758 (1995)

60. Legrini, O., Oliveros, E. and Braun, A. M. "Photochemical processes for water-treatment". *Chem. Rev.* **93**, 671-698 (1993)

61. Frank, S. N. and Bard, A. J. "Heterogeneous photocatalytic oxidation of cyanide and sulfite in aqueous-solutions at semiconductor powders". *J. Phys. Chem.* **81**, 1484-1488 (1977)

62. Frank, S. N. and Bard, A. J. "Heterogeneous photocatalytic oxidation of cyanide ion in aqueous-solutions at TiO_2 powder". *J. Am. Chem. Soc.* **99**, 303-304 (1977)

63. Sjogren, J. C. and Sierka, R. A. "Inactivation of phage MS2 by iron-aided titanium-dioxide photocatalysis". *Appl. Environ. Microbiol.* **60**, 344-347 (1994)

64. Lee, S., Nishida, K., Otaki, M. and Ohgaki, S. "Photocatalytic inactivation of phage Q beta by immobilized titanium dioxide mediated photocatalyst". *Water Sci. Technol.* **35**, 101-106 (1997)

65. Ireland, J. C., Klostermann, P., Rice, E. W. and Clark, R. M. "Inactivation of Escherichia-coli by titanium-dioxide photocatalytic oxidation". *Appl. Environ. Microbiol.* **59**, 1668-1670 (1993)

66. Borgarello, E., Kiwi, J., Pelizzetti, E., Visca, M. and Gratzel, M. "Photochemical cleavage of water by photocatalysis". *Nature* **289**, 158-160 (1981)

67. Amphlett, J. C., Evans, M. J., Mann, R. F. and Weir, R. D. "Hydrogen-production by the catalytic steam reforming of methanol .2. kinetics of methanol decomposition using Girdler G66b catalyst". *Can. J. Chem. Eng.* **63**, 605-611 (1985)

68. Jiang, C. J., Trimm, D. L., Wainwright, M. S. and Cant, N. W. "Kinetic-study of steam reforming of methanol over copper-based catalysts". *Appl. Catal. A-Gen.* **93**, 245-255 (1993)

69. Peppley, B. A., Amphlett, J. C., Kearns, L. M. and Mann, R. F. "Methanol-steam reforming on $Cu/ZnO/Al_2O_3$. Part 1: The reaction network". *Appl. Catal. A-Gen.* **179**, 21-29 (1999)

70. Breen, J. P. and Ross, J. R. H. "Methanol reforming for fuel-cell applications: development of zirconia-containing Cu-Zn-Al catalysts". *Catal. Today* **51**, 521-533 (1999)

71. Rouquerol, J., Avnir, D., Fairbridge, C. W., Everett, D. H., Haynes, J. H., Pernicone, N., Ramsay, J. D. F., Sing, K. S. W. and Unger, K. K. "Recommendations for the characterization of porous solids". *Pure Appl. Chem.* **66**, 1739-1758 (1994)

72. Langmuir, I. "Adsorption of gases on plane surfaces of glass, mica and platiunum". *J. Am. Chem. Soc.* **40**, 1361-1401 (1918)

73. Brunauer, S., Emmett, P. H. and Teller, E. "Adsorption of gases in multimolecular layers". *J. Am. Chem. Soc.* **60**, 309-319 (1938)

74. Chescoe, D. and Goodhew, P. J. *The Operation of transmission and scanning electron microscopes* (Oxford University Press, 1990).

75. Klug, H. P. and Alexander, L. E. *X-ray Diffraction Procedures for Polycrystalline and Amorphous Materials* (Wiley Interscience, New York, 1974).

76. Nakamoto, K. *Infrared and Raman Spectra of Inorganic and Coordination Compounds* (Wiley Interscience Publication, Toronto, 1986).

77. Schrader, B. *Infrared and Raman Spectroscopy: Methods and Applications* (VCH Publishers Inc., New York, 1995).

78. Svedberg, T. and Rinde, H. "The determination of the distribution of size of particles in disperse systems". *J. Am. Chem. Soc.* **45**, 943-954 (1923)

79. Svec, F. and Frechet, J. M. J. "New designs of macroporous polymers and supports: From separation to biocatalysis". *Science* **273**, 205-211 (1996)

80. Arshady, R. "Beaded Polymer Supports and Gels .1. Manufacturing Techniques". *Journal of Chromatography* **586**, 181-197 (1991)

81. Dowding, P. J. and Vincent, B. "Suspension polymerisation to form polymer beads". *Colloid Surf. A-Physicochem. Eng. Asp.* **161**, 259-269 (2000)

82. Smigol, V. and Svec, F. "Synthesis and Properties of Uniform Beads Based on Macroporous Copolymer Glycidyl Methacrylate Ethylene Dimethacrylate - a Way to Improve Separation Media for Hplc". *J. Appl. Polym. Sci.* **46**, 1439-1448 (1992)

83. Meyer, U., Larsson, A., Hentze, H. P. and Caruso, R. A. "Templating of porous polymeric beads to form porous silica and titania spheres". *Adv. Mater.* **14**, 1768-1772 (2002)

84. Shchukin, D. G. and Caruso, R. A. "Template synthesis of porous gold microspheres". *Chem. Commun.*, 1478-1479 (2003)

85. Hwang, Y. K., Lee, K. C. and Kwon, Y. U. "Nanoparticle routes to mesoporous titania thin films". *Chem. Commun.*, 1738-1739 (2001)

86. Wong, M. S., Jeng, E. S. and Ying, J. Y. "Supramolecular templating of thermally stable crystalline mesoporous metal oxides using nanoparticulate precursors". *Nano Lett.* **1**, 637-642 (2001)

87. Reddy, B. M., Ganesh, I., Reddy, E. P., Fernandez, A. and Smirniotis, P. G. "Surface characterization of Ga_2O_3-TiO_2 and V_2O_5/Ga_2O_3-TiO_2 catalysts". *J. Phys. Chem. B* **105**, 6227-6235 (2001)

88. Gaewdang, T., Chaminade, J. P., Gravereau, P., Garcia, A., Fouassier, C., Hagenmuller, P. and Mahiou, R. "Crystal-structure and luminescent properties of indium titanate". *Mater. Res. Bull.* **28**, 1051-1060 (1993)

89. Ryczkowski, J. "IR spectroscopy in catalysis". *Catal. Today* **68**, 263-381 (2001)

90. Haneda, M., Joubert, E., Menezo, J. C., Duprez, D., Barbier, J., Bion, N., Daturi, M., Saussey, J., Lavalley, J. C. and Hamada, H. "Surface characterization of alumina-supported catalysts prepared by sol-gel method. Part I. Acid-base properties". *Phys. Chem. Chem. Phys.* **3**, 1366-1370 (2001)

91. Busca, G. "Spectroscopic characterization of the acid properties of metal oxide catalysts". *Catal. Today* **41**, 191-206 (1998)

92. Rao, N. N., Dubey, A. K., Mohanty, S., Khare, P., Jain, R. and Kau, S. N. "Photocatalytic degradation of 2-chlorophenol: a study of kinetics, intermediates and biodegradability". *J. Hazard. Mater.* **101**, 301-314 (2003)

93. D'Oliveira, J. C., Alsayyed, G. and Pichat, P. "Photodegradation of 2-chlorophenol and 3-chlorophenol in TiO_2 aqueous suspensions". *Environ. Sci. Technol.* **24**, 990-996 (1990)

94. Doong, R. A., Chen, C. H., Maithreepala, R. A. and Chang, S. M. "The influence of pH and cadmium sulfide on the photocatalytic degradation of 2-chlorophenol in titanium dioxide suspensions". *Water Res.* **35**, 2873-2880 (2001)

95. Ku, Y., Leu, R. M. and Lee, K. C. "Decomposition of 2-chlorophenol in aqueous solution by UV irradiation with the presence of titanium dioxide". *Water Res.* **30**, 2569-2578 (1996)

96. Fu, X. Z., Clark, L. A., Yang, Q. and Anderson, M. A. "Enhanced photocatalytic performance of titania-based binary metal oxides: TiO_2/SiO_2 and TiO_2/ZrO_2". *Environ. Sci. Technol.* **30**, 647-653 (1996)

97. Ohtani, B., Bowman, R. M., Colombo, D. P., Kominami, H., Noguchi, H. and Uosaki, K. "Femtosecond diffuse reflectance spectroscopy of aqueous Titanium(IV) oxide suspension: Correlation of electron-hole recombination kinetics with photocatalytic activity". *Chem. Lett.*, 579-580 (1998)

98. Mills, A., Davies, R. H. and Worsley, D. "Water-purification by semiconductor photocatalysis". *Chem. Soc. Rev.* **22**, 417-425 (1993)

99. Wu, N. C., Shi, E. W., Zheng, Y. Q. and Li, W. J. "Effect of pH of medium on hydrothermal synthesis of nanocrystalline cerium(IV) oxide powders". *J. Am. Ceram. Soc.* **85**, 2462-2468 (2002)

100. Nabavi, M., Spalla, O. and Cabane, B. "Surface-chemistry of nanometric ceria particles in aqueous dispersions". *J. Colloid Interface Sci.* **160**, 459-471 (1993)

101. Spalla, O. and Kekicheff, P. "Adhesion between oxide nanoparticles: Influence of surface complexation". *J. Colloid Interface Sci.* **192**, 43-65 (1997)

102. Wang, H., Zhu, J. J., Zhu, J. M., Liao, X. H., Xu, S., Ding, T. and Chen, H. Y. "Preparation of nanocrystalline ceria particles by sonochemical and microwave assisted heating methods". *Phys. Chem. Chem. Phys.* **4**, 3794-3799 (2002)

103. Tsunekawa, S., Sivamohan, R., Ohsuna, T., Kasuya, A., Takahashi, H. and Tohji, K. in *Rare Earths '98* 439-445 (Transtec Publications Ltd, Zurich-Uetikon, 1999).

104. Svedberg, T. and Pedersen, K. O. *The Ultracentrifuge* (Clarendon Press, Oxford, 1940).

105. Colfen, H. and Pauck, T. "Determination of particle size distributions with angstrom resolution". *Colloid Polym. Sci.* **275**, 175-180 (1997)

106. Pinna, N., Wild, U., Urban, J. and Schlogl, R. "Divanadium pentoxide nanorods". *Adv. Mater.* **15**, 329-331 (2003)

107. Vogel, W. "X-ray diffraction from clusters". *Cryst. Res. Technol.* **33**, 1141-1154 (1998)

108. Kurth, D. G., Lehmann, P., Volkmer, D., Colfen, H., Koop, M. J., Muller, A. and Du Chesne, A. "Surfactant-encapsulated clusters (SECs): $(DODA)_{20}(NH_4)[H_3Mo_{57}V_6(NO)_6O\text{-}_{183}(H_2O)_{18}]$, a case study". *Chem. Eur. J.* **6**, 385-393 (2000)

109. Yashima, M., Arashi, H., Kakihana, M. and Yoshimura, M. "Raman-scattering study of cubic-tetragonal phase-transition in $Zr_{1-X}Ce_xO_2$ solid-solution". *J. Am. Ceram. Soc.* **77**, 1067-1071 (1994)

110. Yashima, M., Takashina, H., Kakihana, M. and Yoshimura, M. "Low-temperature phase-equilibria by the flux method and the metastable-stable phase-diagram in the ZrO_2-CeO_2 system". *J. Am. Ceram. Soc.* **77**, 1869-1874 (1994)

111. Vlaic, G., Di Monte, R., Fornasiero, P., Fonda, E., Kaspar, J. and Graziani, M. "Redox property-local structure relationships in the ph-loaded CeO_2-ZrO_2 mixed oxides". *J. Catal.* **182**, 378-389 (1999)

112. JCPDS. Card No. 43-1002

113. Tsunekawa, S., Sivamohan, R., Ito, S., Kasuya, A. and Fukuda, T. "Structural study on monosize CeO_{2-x} nano-particles". *Nanostruct. Mater.* **11**, 141-147 (1999)

114. Tsunekawa, S., Ishikawa, K., Li, Z. Q., Kawazoe, Y. and Kasuya, A. "Origin of anomalous lattice expansion in oxide nanoparticles". *Phys. Rev. Lett.* **85**, 3440-3443 (2000)

115. Tosan, J. L., Durand, B., Roubin, M., Bertin, F. and Loiseleur, H. "Potentiometric and Raman-Spectroscopic Characterization of Gelatinous Precipitates Formed by Hydrolysis of Zirconium Oxychloride Solutions". *Eur. J. Solid State Inorg. Chem.* **30**, 179-193 (1993)

116. Spanier, J. E., Robinson, R. D., Zheng, F., Chan, S. W. and Herman, I. P. "Size-dependent properties of CeO_{2-y} nanoparticles as studied by Raman scattering". *Phys. Rev. B* **64** (2001)

117. Richter, H., Wang, Z. P. and Ley, L. "The One Phonon Raman-Spectrum in Microcrystalline Silicon". *Solid State Commun.* **39**, 625-629 (1981)

118. Southon, P. D., Bartlett, J. R., Woolfrey, J. L. and Ben-Nissan, B. "Formation and characterization of an aqueous zirconium hydroxide colloid". *Chem. Mater.* **14**, 4313-4319 (2002)

119. Wachs, I. E. "Raman and IR studies of surface metal oxide species on oxide supports: Supported metal oxide catalysts". *Catal. Today* **27**, 437-455 (1996)

120. Colon, G., Pijolat, M., Valdivieso, F., Vidal, H., Kaspar, J., Finocchio, E., Daturi, M., Binet, C., Lavalley, J. C., Baker, R. T. and Bernal, S. "Surface and structural characterization of $Ce_xZr_{1-x}O_2$ CEZIRENCAT mixed oxides as potential three-way catalyst promoters". *J. Chem. Soc. Faraday Trans.* **94**, 3717-3726 (1998)

121. JCPDS. Card No. 37-1484

122. Rhodes, K. H., Davis, S. A., Caruso, F., Zhang, B. J. and Mann, S. "Hierarchical assembly of zeolite nanoparticles into ordered macroporous monoliths using core-shell building blocks". *Chem. Mater.* **12**, 2832-2834 (2000)

123. Bouchara, A., Soler-Illia, G., Chane-Ching, J. Y. and Sanchez, C. "Nanotectonic approach of the texturation of CeO_2 based nanomaterials". *Chem. Commun.*, 1234-1235 (2002)

124. Forster, S. and Kramer, E. "Synthesis of PB-PEO and PI-PEO block copolymers with alkyllithium initiators and the phosphazene base t-BuP4". *Macromolecules* **32**, 2783-2785 (1999)

125. Forster, S., Berton, B., Hentze, H. P., Kramer, E., Antonietti, M. and Lindner, P. "Lyotropic phase morphologies of amphiphilic block copolymers". *Macromolecules* **34**, 4610-4623 (2001)

Popular abstract

Nanostructured materials are the materials having structural features on the scale of nanometers i.e. 10^{-9} m. the structural features can enhance the natural properties of the materials or induce additional properties, which are useful for day to technology as well as the future technologies

One way to synthesize nanostructured materials is using templating techniques. The templating process involves use of a certain "mould" or "scaffold" to generate the structure. The mould is called as the template, can be a single molecule or assembly of molecule or a larger object, which has its own structure. The product material can be obtained by filling the space around the template with a "precursor", transformation of precursor into the desired material and then removal of template to get product. The precursor can be any chemical moiety that can be easily transformed in to the desired material. Alternatively the desired material is processed into very tiny bricks or "nano building blocks (NBB)" and the product is obtained by arrangement of the NBB by using a scaffold.

We synthesized porous metal oxide spheres of namely TiO_2-M_2O_3: titanium dioxide- M-oxide (M = aluminum, gallium and indium) TiO_2-M_2O_3 and cerium oxide-zirconium oxide solid solution. We used porous polymeric beads as templates. These beads used for chromatographic purposes. For the synthesis of TiO_2-M_2O_3 we used metal- alkoxides as precursor. The pore of beads were filled with precursor and then reacted with water to give transformation of the precursor to amorphous oxide network. The network is crystallized and template is removed by heat treatment at high temperatures. In a similar

way we obtained porous spheres of $Ce_xZr_{1-x}O_2$. For this we synthesized nanoparticle of $Ce_xZr_{1-x}O_2$ and used then for the templating process to obtain porous $Ce_xZr_{1-x}O_2$ spheres. Additionally, using the same nanoparticles we synthesized nano-porous powder using self-assembly process between a block-copolymers scaffold and nanoparticles.

Morphological and physico-chemical properties of these materials were studies systematically by using various analytical techniques

TiO_2-M_2O_3 material were tested for photocatalytic degradation of 2-Chlorophenol a poisonous pollutant. While $Ce_xZr_{1-x}O_2$ spheres were tested for methanol steam reforming reaction to generate hydrogen, which is a fuel for future generation power sources like fuel cells. All the materials showed good catalytic performance.

Resume

Atul Suresh Deshpande

Birth date: 2nd of March 1977 in Nanded, India.

1982-1994	Primary and secondary education at S. J. Vidyalaya, Daund. India.
1994-1997	Bachelor of Science (Chemistry) From S. P. College, Pune University of Pune, India.
1997-1999	Master of Science (Inorganic Chemistry) From The Department of Chemistry, University of Pune, India.
Since 2001	Ph.D. student at Max Planck Institute of Colloids and Interfaces, Golm, under the guidance of Prof. Dr. Markus Antonietti in the group of Dr. Rachel Caruso (formerly) and Dr. Markus Niederberger working on the project "Fabrication of porous metal oxide for catalytic applications using templating techniques"

Acknowledgement

I would like to express my gratitude towards all the persons who have helped me or stayed along my side during this work.

First, I would like to thank Prof. Dr. Markus Antonietti for giving me this great opportunity to work in this internationally acclaimed research institute.

I am grateful to my supervisors Dr. Rachel Caruso and Dr. Markus Niederberger who guided me through my work. Especially to Markus for being very kind and nice to me and helping me and working extra long times for correcting my thesis!

I am thankful to the Dr. Angelo Valleriani, the coordinator of IMPRS on biomimetic systems and other member, for an all-new learning experience.

This work was of course not possible without the kind help from my fellow co-workers and collaborators. I appreciate the help from Dr. Dmitry Shchukin for the photocatalytic activity measurement, Dr. Nicola Pinna for the HRTEM measurements, Pablo Beato for the Raman studies, Hary Soerijanto and Benjamin Frank for the testing of catalyst methanol steam reforming reactions, Dr.Helmut Schlaad and Ines below for providing the magic block-copolymer for the self-assembly reactions and Dr. Bernd Smarsly and Dr. Helmut Cölfen for the fruitful discussions.

I express my gratitude to Ingrid Zenke, Rona Pitchke, Dr. Hartman, Roy knocke, Regina Rothe and AntjeVölkel for performing all the analytical work for me.

I thank my former colleagues, Jan and Heike for helping me with the work, my present colleagues Georg, Julien and Jianhua gave me the true “global family” feeling. I enjoyed the French lessons from Julien, and learnt a few differences between the Austrian and German “German” from Georg!

Special thanks to Cilâine, Sandra and Kerstin for giving me moral support, helping me with my presentations and talks, German language lessons and giving me company for lunch!

I am in debt of the all my Indian friends in Potsdam and Berlin with whom I celebrated the festivities, who never let me feel alone, lifted my spirits up in the bad times and gave me a feeling of home away from home.

No acknowledgement from MPI can be complete without the mention of Eric C.! It was nice experience for me. I enjoyed the music, the parties in Chez Briel and the kicker!

I admire the support given to me from all my teachers, friends at the University of Pune and colleagues at NCL who contributed one way or the other in fulfilling this task.

I owe a great deal to my family. My father Suresh, mother Vijaya and my brother Uday, his wife Vasudha and their son Anish, who supported me in every situation in life, provided me with the best things they have and took a good care of me. I hope I live up to their expectation and make them proud.

Thank you!

3Fi trd"